

(NASA-CR-149800) RCTATING GRAVITY
GRADIOMETER STUDY Final Report, Aug. 1975 -
Jun. 1976 (Hughes Research Labs.) 174 p HC
A06/ME A01 CSCL 14E

7
N77-19366

Unclas
G3/35 20547

RCTATING GRAVITY GRADIOMETER STUDY

Robert L. Forward
Principal Investigator

Robert M. Lemmen
Program Manager

Roger W. Lowe
Robert W. Peterson
Ichiro Tonai
W. E. Williams

HUGHES RESEARCH LABORATORIES
3011 Malibu Canyon Road
Malibu, California 90265

30 June 1976

FINAL REPORT
JPL Contract 954309

for the period from
August 1975 through June 1976

David H. Swenson
JPL Technical Manager



This work was performed for the Jet Propulsion Laboratory,
California Institute of Technology sponsored by the
National Aeronautics and Space Administration under
Contract NAS7-100

ABSTRACT AND SUMMARY

This report contains a number of preliminary studies on the application of a Rotating Gravity Gradiometer (RGG) system on board a Lunar Polar Orbiter (LPO) for the measurement of the Lunar gravity field. An RGG system would be desirable for the LPO mission since it would significantly reduce the total mission weight and cost budgeted for the gravity portion of the science by eliminating the need for a Relay Satellite and by decreasing the tracking time needed for full Lunar coverage from months of continuous tracking to daily data dumps. However, there were a number of questions on the compatibility of the present airborne RGG design with the LPO mission. The various studies in this report address those questions. A data collection simulation study shows that a gradiometer will give significantly better gravity data than a doppler tracking system for the altitudes under consideration for the LPO, that the present demonstrated sensitivity of the RGG is adequate for measurement of the Lunar gravity gradient field, and that a single RGG instrument will provide almost as much data for geophysical interpretation as an orthogonal three axis RGG system. An engineering study of the RGG sensor/LPO spacecraft interface characteristics shows that the RGG systems under consideration are compatible with the present models of the LPO spacecraft, can be placed anywhere on the spacecraft, do not require any special alignment or thermal environment, do not generate RF, magnetic or other disturbing fields and put no new constraints on spacecraft attitude, rate and control system accuracies. The interface study also contains a physical and functional description of a typical RGG system as designed for a spacecraft. An error simulation study shows that the errors in spacecraft orbital position and spacecraft attitude will not significantly degrade the gravity gradient data during the data reduction process.



ORIGINAL PAGE IS
OF POOR QUALITY

TABLE OF CONTENTS

SECTION	PAGE
CONCLUSIONS	5
RECOMMENDATIONS	6
STUDY TASK RESULTS	7
TASK 1 - Measurement Sensitivity and Repeatability	7
TASK 2 - Identification and Tabulation of Error Sources	11
TASK 3 - Science Return Trade-Off Study	13
TASK 4 - Spacecraft/Gradiometer Interface Characteristics	16
TASK 5 - Increased Science Return Vs. Number of Sensors, Spacecraft Maneuvers and Data Reduction Complexity	17
TASK 6 - Potential Sensor Simplifications for Zero-G	20
REFERENCES	22
APPENDICES	23
A Gravity Gradient Mapping From the LPO - Science Return Simulation Study	A-1
B Functional and Physical Description Gravity Environment Measurement System (GEMS)	B-1
C LPOSIM Fortran Program - Simulates the Lunar Polar Orbiter Gravity Gradient Experiment	C-1
D Lunar Polar Orbiter Gravity Gradient Experiment Simulation Plots	D-1

CONCLUSIONS

The general conclusion of this multi-study effort is that a Rotating Gravity Gradiometer is not only compatible with a Lunar Polar Orbiter mission, but will provide science data of higher resolution and higher sensitivity than the planned Doppler tracking system. It will also significantly reduce the total mission weight required for the gravity experiment by eliminating the need for a Relay Satellite and will decrease the DSN tracking time required for full Lunar coverage from nearly continuous tracking for months to daily data dumps. In Appendix A, a data collection simulation study shows that a gradiometer will give significantly better gravity data than a doppler tracking system for the altitudes under consideration for the LPO. The study also simulated the effects of sensor noise on the mapping of gravity gradient data and the integration of gradient data into gravity data and found that the present demonstrated sensitivity of the RGG is adequate for measurement of the Lunar gravity gradient field. Other portions of the data simulation study found that a single RGG instrument oriented along the orbital axis to measure the gravity gradients in the orbital plane will provide almost as much data for geophysical interpretation as an orthogonal three axis RGG system. The cross gradient output of the RGG should be integrated with the spacecraft velocity to obtain a contour map of the vertical gravity field, and then the higher resolution (but slightly distorted) principal gradient difference output of the RGG should be used to enhance the resolution of the data set for geophysical interpretation purposes. In Appendix B, an engineering study of the RGG sensor/LPO spacecraft interface characteristics shows that the RGG systems under consideration are compatible with the present models of the LPO spacecraft, can be placed anywhere on the spacecraft, do not require any special alignment or thermal environment, do not generate RF, magnetic or other disturbing fields, put no new constraints on spacecraft attitude and rates, and should not affect the spacecraft attitude control system if the RGG angular momentum is included in the spacecraft control equations. Appendix B of the report also contains a physical and functional description of a typical RGG system as designed for a spacecraft. Another simulation study (See Appendix C and D and Task 5) that includes the orbital motion and attitude variations of the spacecraft shows that the variation in spacecraft orbital altitude and position, and spacecraft attitude errors will not significantly degrade the gravity gradient data.

RECOMMENDATIONS

Because of the compatability of the RGG system with the LPO spacecraft and mission, and because of the significant advantages to be gained by replacing the Relay Satellite and Doppler velocity tracking system with an on board gravity gradiometer, it is recommended that serious consideration be given to the funding of an instrument development effort to produce a breadboard version of an RGG sensor and spacecraft compatible electronics, combined with sufficient testing and demonstration of the sensor to reduce the technical risk associated with a new instrument concept and to increase the confidence level in the LPO Science Board on the use gradiometer instruments as a means of measuring Lunar gravity.

STUDY TASK RESULTS

TASK 1 - MEASUREMENT SENSITIVITY AND REPEATABILITY

The first task on the study was to evaluate the measurement sensitivity and repeatability of gravity gradient measurement using the existing Hughes Rotating Gravity Gradiometer under controlled laboratory conditions.

Since the Hughes RGG was undergoing continuous testing, rework and improvement during the study period, this was a continuing effort throughout the contract.

Measurement Sensitivity

A single Rotating Gravity Gradiometer measures the gravity gradient components in the plane of its rotation. In operation, the phase of the signal demodulation process is adjusted so that the zero phase of demodulation occurs when the rotor index is aligned with one of the sensor external mounting reference directions. The demodulated RGG signal then contains two independent outputs, the sine (Sxy) or inphase output which contains a measure of the difference in the two principal gravity gradient components in the sensor plane of rotation (Gxx-Gyy), and the cosine (Cxy) or quadrature phase output which contains a measure of 2 Gxy or twice the cross gradient component in the plane of rotation.

If three orthogonal RGG sensors are used, then the five independent components of the gravity gradient tensor can be obtained from the six sensor outputs by combining the sensor outputs as follows:

$$G_{xx} = (S_{xy} - S_{zx})/3$$

$$G_{yy} = (S_{yz} - S_{xy})/3$$

$$G_{zz} = -G_{xx} - G_{yy} \quad (\text{not independent})$$

$$G_{xy} = C_{xy}/2$$

$$G_{yz} = C_{yz}/2$$

$$G_{zx} = C_{zx}/2$$

ORIGINAL PAGE IS
OF POOR QUALITY

Since the Laplacian of the gravitational gradient tensor is zero,

$$G_{xx} + G_{yy} + G_{zz} = 0$$

and this is just the trace of the gravity gradient tensor, we find that the principal components of the tensor are not independent.

When an analysis of the propagation of the sensor random noise error through this computational process is carried out, we find that the error in calculating the gravitational gradient tensor from the sensor outputs is slightly different for the two types of gradient components since we have six sensor outputs and only five independent gradient components. For the cross gradient components, the measurement sensitivity is just half of the sensor random noise in the cosine output. For the principal components, the measurement sensitivity is $1.414/3$ of the sensor random noise (since there are two independent sensor measurements combined to obtain each principal gradient component). This ratio is $1/2.12$ or a little less than half of the sensor random noise in the sine output.

Periodically during the contract, at times when the sensor was not being tested or reworked on our ongoing AFGL/ARPA Rotating Gravity Gradiometer Development contract, we would carry out sensitivity and repeatability measurements with the sensor oriented so that its spin axis was in the vertical orientation. In this orientation, the effects of earth gravity on the sensor were a minimum. They are still not negligible however. At its present stage of development, the RGG still contains a large sensitivity to earth gravity due to its anisoelastic response. To correct this error sensitivity requires cutting metal in the sensor arm plates and this final trim is not planned for a number of months until after the final, high precision bearings are delivered and installed and the sensor error coefficients remeasured on the new bearings. Despite the fact that there is still a large earth gravity sensitivity in the present configuration, we were able to obtain error sensitivity data that was almost at the final sensitivity goal of ± 1 Eotvos for a 10 sec integration time. (1 Eotvos is defined as ± 1 nanogal/cm where a gal (Galileo) is 1 cm/sec/sec. An equivalent unit for lunar mascon work would be 0.1 mgal/km or 0.1 milligal accuracy of measurement of lunar gravity due to a kilometer change in distance.)

The plots shown in Figure {1} are the two outputs of the RGG in the laboratory with the spin axis vertical showing the random noise characteristics over a fifteen minute period. The sensitivity levels quoted are the sensitivity in calculating the gravity gradient component from the sensor output, which is roughly half of the unprocessed sensor output.

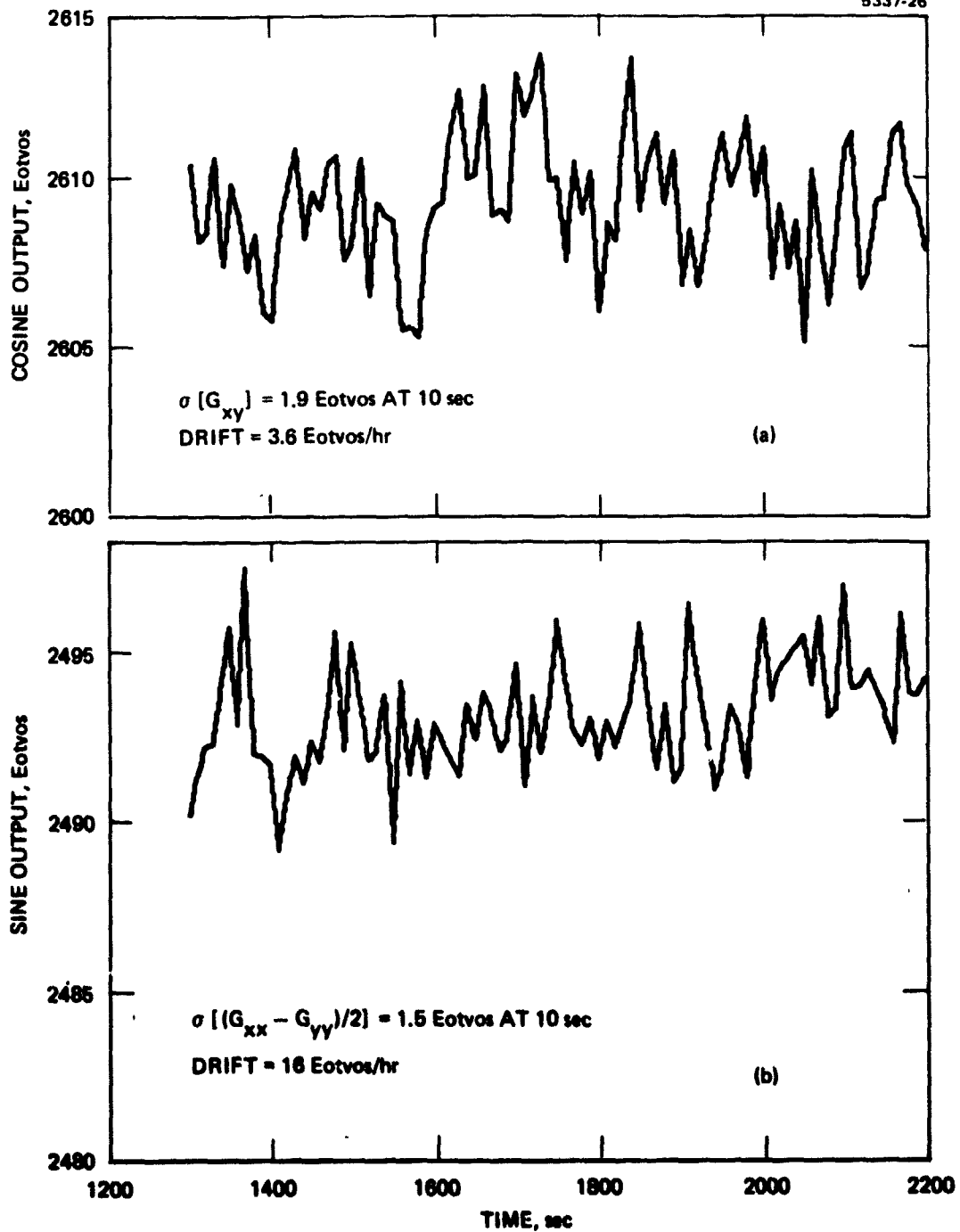


Figure (1) - Measurement Sensitivity of RGG in Laboratory

Repeatability

Repeatability of the RGG sensor is best demonstrated in the laboratory by moving a test mass close to the sensor, thus inserting a gravity gradient signal into the sensor to increase the sensor output, then later removing the mass, measuring the decrease and comparing its magnitude with the previously caused increase. It is not possible with the present laboratory setup to replace the mass accurately enough to repeat the test again with exactly the same gravity input, since a change in placement of as little as 100 microns at the 20 cm distances that separate the test mass from the sensor can cause a significant error in the gravity input.

An example of the repeatability of the RGG in the laboratory is given in Figure {2}. The magnitude of the sensor output was first determined by taking a 100 sec average, then the test mass was placed in proximity to the sensor. After the signal rise had settled, the magnitude of the sensor output was measured again with another 100 sec average. The test mass was then removed, and after the fall time had settled, a third 100 sec average was taken. The signal rise was $+417.3$ Eotvos, while the signal fall 2.5 minutes later was -416.7 Eotvos, or a repeatability to within 0.6 Eotvos (within the random noise).

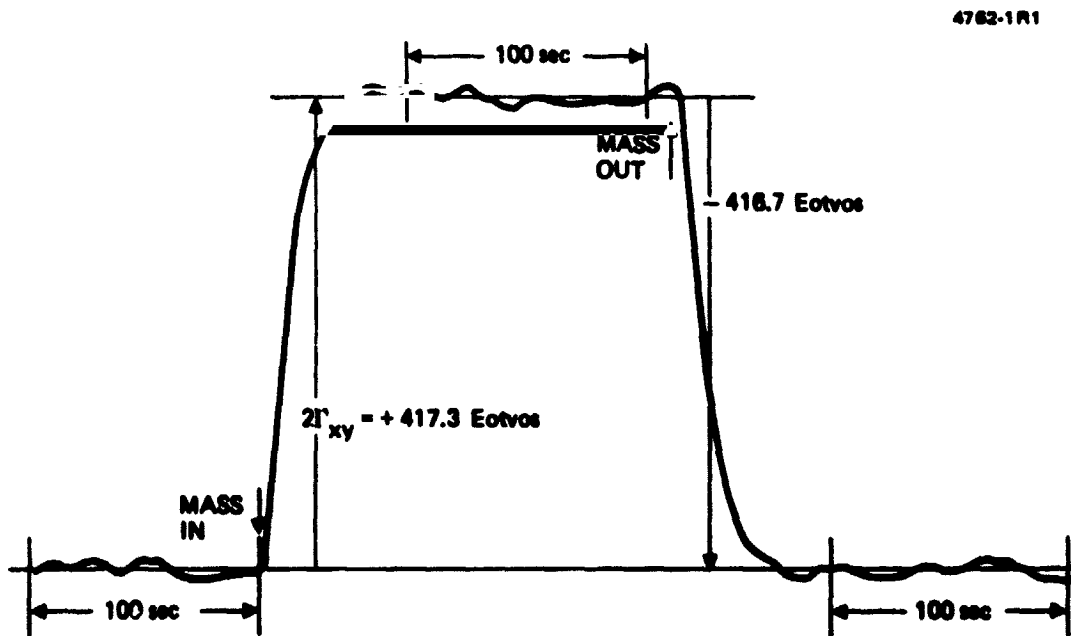


Figure {2} - Repeatability of RGG in Laboratory

TASK 2 - IDENTIFICATION AND TABULATION OF ERROR SOURCES

Our work on Task 2 involved the identification and tabulation of the error sources associated with the gravity gradient measurements of Task (1). Those errors associated with the operation of the gradiometer in the Earth's gravitational field were then separately identified. By separating out the errors caused by operation in the Earth's gravity field, we can then make a better estimate of the expected performance of the RGG sensor in the nearly free-fall LPO spacecraft environment.

The details of the various sensor error sources are documented in the ongoing contract reports [1,2] on the development of the Rotating Gravity Gradiometer. Most, if not all, of the error sources of concern are due to the effects, either direct or indirect, of the one g environment of the earth acting on the sensor. Of the 23 separately identified error sources, 14 are directly or indirectly dependent upon the earth's gravity field. The only error sources that are independent of the earth's gravity field are: thermal noise (which is the largest error source at 1/3 the error budget), speed control servo noise, data digitalization noise, scale factor or gain shift errors, sensor resonant frequency shift, and magnetic field sensitivity.

After some consideration and identification of the effect on the error coefficients of the earth's gravity field, Table [1] was prepared to show the expected contributions to the sensor errors of the various sensor error coefficients assuming the more benign environment of the LPO spacecraft.

TABLE 1 - SUMMARY OF RGG ERROR SOURCES

	Worst Case Airborne Prototype (Eotvos @ 10 s)	Estimated Lunar Orbiter (Eotvos @ 10 s)
Thermal noise ($T = 326^{\circ}\text{K}$)	0.30	0.30
Resonant frequency phase shift	0.26	0.26
Skew misalignment	0.23	0.05
Scale factor or gain shift	0.21	0.21
Axial vibration-to-torsion error	0.20	0.05
Dynamic mass unbalance g sensitivity	0.20	0.00
Speed control servo noise	0.10	0.10
Digitalization error noise	0.15	0.15
Prime anisoelasticity g^2 sensitivity	0.14	0.00
Differential mass unbalance g sensitivity	0.12	0.00
Sum mode mismatch	0.10	0.05
	—	—
RSS Total	0.64	0.49

T1732

TASK 3 - SCIENCE RETURN TRADE-OFF STUDY

One of the first studies carried out in this program was a trade-off study to determine the science return (both sensitivity and gravity harmonics [resolution]) as a function of orbital altitude. This was done by carrying out a computer simulation of what we could expect from a typical RGG system operating in an LPO spacecraft at various altitudes compatible with the LPO mission. The most important concern was the type (format, directionality and units) and quality (sensitivity and resolution) of the science return that we could expect from the total system. Was it adequate for scientific purposes? Was the data in a form that was readily utilized by other scientists not in the specialization of gravity gradiometry? We also broadened the trade-off study to include the question: How did the data obtained from a gravity gradiometer system compare in type and quality to that obtained from other methods of obtaining the same information (specifically that obtained from a Doppler velocity tracking system that was the original choice of the LPO mission analysts because of its previous utilization in mapping Lunar mascons)?

The results of the study are presented in Appendix A - Gravity Gradient Mapping from the LPO - Science Return Simulation Study by Dr. Robert L. Forward, the Principal Investigator (with substantial assistance from Richard W. Lowe). The paper has been accepted (without change) for publication in The Moon. The results of the simulation were very positive and surprising to everyone (including the highly biased PI).

The simulations showed that gravity gradient data obtained using existing designs of airborne gravity gradient sensors would be of high resolution and high sensitivity and thus of the high quality needed for science interpretation. The simulations showed that certain components of the gravity gradient data could be plotted directly into gradient contour maps and used by geophysicists for interpretation of subsurface structures, or alternatively, other components of the gravity gradient could be easily converted into more familiar gravity contour maps. Also, gravity contour maps obtained from gravity gradient data were found to have better resolution and signal-to-noise than gravity contour maps obtained from Doppler tracking data.

In the simulation studies, a frontside map of the Lunar mascons taken from a paper by Sjogren, Wimberly and Wollenhaupt [3] were used to generate a point mass model. The point mass model was taken as the starting basis for the simulation since it could reproduce a gravity field that had a very close resemblance to the actual Lunar gravity field and yet had a number of high frequency features that could test the resolution and sensitivity requirements of any gravity measurement system. The results of the work are summarized by the abstract of the paper:

ABSTRACT

Simulations of the gravity data to be expected from a Lunar Polar Orbiter spacecraft utilizing either a Doppler velocity tracking system or a gravity gradiometer instrument system are generated using a point mass model that gives an excellent representation of the types of gravity anomalies to be found on the moon. If the state of the art in instrumentation of both systems remain at the level of ± 1 mm/sec at 10 sec integration time for the Doppler velocity system accuracy and at ± 1 Eotvos ($1 \text{ Eotvos} = 10 \text{ nrad/sec/sec} = 1 \text{ ngal/cm} = 0.1 \text{ mgal/Km}$) at 10 sec integration time for the gravity gradiometer system accuracy, inspection of the simulation plots show that a gravity gradiometer system will give science data with resolution that is nearly twice that of the Doppler system along with signal-to-noise ratio that is twice that of the Doppler velocity system at altitudes below 100 Km. The error model used in the study is one where the system errors are assumed to be dominated by point measurement noise and data quantization noise. The effects of other, more controllable, systematic error sources are not considered in this analysis.

The superiority of the gravity gradient measuring system over the Doppler tracking system found in the studies has been corroborated by concurrent studies done elsewhere, such as the recent work by Ananda, Lorell and Flury [4] who also compared the two systems using a different simulation procedure and got essentially the same results.

Other recent studies also raise some warning about possible problems with satellite-to-satellite Doppler tracking systems. A recent NASA/Goddard Contract report by Estes and Lancaster [5] on a low-low Earth Gravsat mission found that:

"Recovery of local sets of density blocks from long data arcs was found not to be feasible due to strong aliasing effects."

Similar studies are underway by Estes on high-low Earth orbit satellite-to-satellite Doppler tracking systems which are closer to the planned LPO mission configurations. Preliminary results indicate that the aliasing problem is less severe for the high-low case (factors of 4 to 10 better) but it is still there. It would be important for the high-low aliasing studies to be repeated for typical LPO mission profiles to determine the real

accuracy obtainable from an LPO-Relay Doppler tracking system. For it may turn out that the data reduction accuracy, when limited by aliasing problems, will not permit a determination of the mascon densities to the accuracies that would be implied by a naive extrapolation of the ± 1 mm/sec measurement accuracy of the Doppler velocity tracking system.

TASK 4 - SPACECRAFT/GRADIOMETER INTERFACE CHARACTERISTICS AND CONSTRAINTS

Our work on Task 4 involved the identification of the spacecraft/gradiometer interface characteristics and constraints. These included the following:

- (A) Weight
- (B) Power
- (C) Mechanical Envelope
- (D) Thermal Control
- (E) Science Data Rates/Format
- (F) Engineering Data Rates/Format
- (G) Command (Rate and Format)
- (H) Mechanical Alignment
- (I) Attitude Control (Rate and Acceleration)

The details of the interface characteristics and constraints as well as a physical and functional description of an RGG system designed for the LPO spacecraft are contained in Appendix B - Functional and Physical Description of the Gravity Environment Measurement System (GEMS). The general conclusions of the study are that the RGG sensor is compatible with the LPO spacecraft designs presently under consideration. The detailed conclusions can be found in the Appendix.

TASK 5 - INCREASED SCIENCE RETURN VS. NUMBER OF SENSORS,
SPACECRAFT MANEUVERS AND DATA REDUCTION COMPLEXITY

Task 5 involved an evaluation of the increase in science return as a function of the number of sensors (number of axes of gravity data), possible spacecraft maneuvers, and complexity of science data reduction. This was done with a computer simulation of the output of typical RGG sensors operating in an LPO spacecraft undergoing orbital and attitude motions that might be expected in a typical mission profile. (The computer Fortran program is printed in Appendix C.)

To keep the study within the bounds consistent with the extent of this effort, a number of simplifications to the simulation were made:

First, the Moon and the LPO orbit were both assumed to be inertially fixed in space. The motion of the Moon about the Earth and the Earth about the Sun, as well as the effects of the other masses in the Solar system were neglected.

Second, the simulation assumed that the LPO orbit was affected only by the primary mass of the moon, and was not affected by the rest of the Solar system masses or by the test mascons. Since we were not going to calculate the Doppler velocity changes for comparison with the gravity gradient signals we did not include the effect of the small test mascons on the orbit since the altitude changes (1-5 m) are negligible for the test mascon masses that we used in the simulation.

Third, we assumed that the LPO orbit inclination was exactly polar. Although it is known that the LPO inclination will probably never be greater than 85 degrees because of orbit instabilities, we felt that the errors and data reduction problems introduced by the non-polar orbit are not of major concern and that a simulation carried out assuming a polar orbit would show the effects of the various errors that were of concern.

Fourth, only a few small test mascons were placed in the simulation to check the detection sensitivity and resolution of the RGG system. We could have attempted to emplace the complex multimass system developed in the Task 3 study into this simulation, but we felt that those results and conclusions could be reasonably applied to this simulation if we could show comparable sensitivity and resolution results for a few point masses.

Fifth, the error sources introduced into the simulation were assumed to be independent. Orbital eccentricity could be changed without affecting attitude offsets, and the attitude angular rates and pointing errors were both assumed small enough so that they could also be considered independent.

However, to keep the simulation realistic and to exercise the capabilities of the Gravity Gradient measurement system, a number of things were not simplified.

First, the altitude and eccentricity of the LPO orbit was made variable. Since a major concern is the change in the background bias of the Lunar field as the LPO spacecraft varies in altitude, it was important to examine the effects of this background bias shift on the data reduction process as it attempted to resolve the test mascons.

Second, although the Moon was assumed to be inertially fixed in space, the simulation has the Moon rotating at its sidereal angular rate. This rotational motion moves the mascons under and past the LPO orbital ground track and allows a determination of the cross track resolution that is obtainable from comparison of successive orbital passes.

Third, rather than calculating the gravity gradient tensor in a lunar surface fixed frame, the gradient was calculated at the position of the spacecraft in an inertially fixed frame. This inertially fixed frame rotates with respect to the vertically oriented spacecraft reference frame once each orbit, which rotates the tensor measured by the gravity gradient sensor twice each Lunar orbit. Once calculated in the inertial reference frame, the gravity gradient tensor is then rotated by the angular rotation of the spacecraft to put it into a Lunar vertical reference frame. This insures that any subtle mixing effects of the local vertical reference system with the ellipticity of the orbit will be made evident.

Fourth, the simulation had provision for inserting both angular rate and pointing errors into all three axes of the spacecraft measurement frame. These could either be constant values or time varying errors.

Fifth, the simulation provides a multiplicity of outputs. These include calculations of the six outputs of the three orthogonal gravity gradiometer instruments, the six components of the gravity gradient tensor field as calculated from the instrument outputs, the trace of the gravity gradient tensor (which should be twice the square of the total spacecraft angular rate), as well as the spacecraft altitude and elapsed time.

The results of the simulation are presented in Appendix D - Lunar Polar Orbiter Gravity Gradient Experiment Simulation Plots, by Dr. Robert L. Forward.

The conclusions that can be drawn from the simulation are:

Spacecraft altitude variations due to an elliptical orbit may cause some loss of sensitivity and resolution, but the bias shifts introduced should not prevent the extraction of the higher frequency gravity data.

Spacecraft attitude tilts cause a bias shift, and should be rapidly recognizable and measured to milliradian accuracy by their appearance in the cross gradient terms.

Periodic attitude errors caused by malfunction of the attitude control system will cause significant data reduction errors if the attitude error amplitudes are large (greater than 1 degree) and of rapid period (less than 5 minutes). (Since they are time varying, they will show up as angular tilts in the cross gradient outputs and as angular rate gradients of the same periodicity but quadrature phase in the trace.)

A single RGG sensor oriented along the orbital axis to measure the gravity gradients in the plane of the orbit can use the lunar orbit track to track spacing of about 30 km to obtain good resolution of mascons in both the along track and cross track directions. The cross gradient output of the RGG should be integrated with the spacecraft velocity to obtain a contour map of the vertical gravity field, and then the higher resolution (but slightly distorted) principal gradient difference output of the RGG should be used to enhance the resolution of the data set for geophysical interpretation purposes.

TASK 6 - POTENTIAL SENSOR SIMPLIFICATIONS FOR ZERO-G

Task 6 involved evaluating the existing gravity gradiometer design to identify those aspects of the instrument which can be modified or simplified to reduce instrument costs due to operation of the instrument in a zero (0) g environment.

The RGG sensor design was first examined for potential modifications and simplifications with the realization that the following RGG error sources would contribute significantly less noise (or none at all) in the zero-g environment of the Lunar Polar Orbiter, relative to their noise contributions in the earth's g field environment:

- (a) Differential mass unbalance g sensitivity
- (b) Dynamic mass unbalance g sensitivity
- (c) Anisoelastic g-squared sensitivity
- (d) Skew misalignment transverse vibration sensitivity
- (e) Axial vibration-to-torsion sensitivity
- (f) Sum mode mismatch spin variation sensitivity

If all of these sensitivities were significantly reduced by operation in the LPO, then the special designs, devices and tolerance call-outs that were required to keep these sensitivities under control in the earth environment could possibly be relaxed for the Lunar orbital environment. Some possible cost-saving factors that would result would be:

- (a) Elimination of the fine mass balance tubes and their control electronics.
- (b) Omission of the isoelastic cut-outs in the sensor arm plates.
- (c) Combination of the inner and outer rotor shells into a single shell which supports the arm/end mass/pivot structure as well as the spin bearings, drag cups and rotary transformers.
- (d) Relaxation of the high tolerances on the fabrication of the spin bearings (eliminating the costly final hand lapping operation).
- (e) Reduction in time required for instrument assembly, test and balancing.

With these possibilities in mind, the analyst who carried out the error analyses for the earth bound RGG was asked to reexamine his equations and assumptions for an orbital case. The relaxation from one g to zero g was found to eliminate the need for the fine mass balance tubes and the special isoelastic cut-outs in the arm plates, producing some cost savings. However, the largest remaining error source was the skew axis misalignment driven by transverse vibrations coupling in through the misalignment between the spin axis and the sensor torsional axis. The transverse vibrations can come from an external source or can be generated internally in the spin bearings. Although bearing vibrations are usually driven by the g loading on the bearing, they can also come from bearing fabrication errors. Thus, until further work produces a different conclusion, we do not feel it is prudent to recommend any further cost reductions that could be obtained from relaxing the fabrication tolerances on the spin bearings or the cruciform sensing structure, or the removal of the provision for aligning the spin axis with the torsional axis (which involves differential adjustment of the inner rotor holding the sensor/end mass/pivot structure and the outer rotor holding the spin bearings).

REFERENCES

1. C. B. Ames, et al., "Rotating Gravity Gradiometer"
R&D Design Evaluation Report on Contract
F19628-76-C-0107 with Air Force Geophysics Lab,
L. G. Hanscom Field, Bedford, MA 01731 (March 1976)
2. C. B. Ames, et al., "Test Evaluation and Modification
of Prototype Rotating Gravity Gradiometer", Final
Report on Contract F19628-75-C-0201 with
Air Force Cambridge Research Lab, Hanscom AFB, MA
(July 1975)
3. W. L. Sjogren, R. N. Wimberly and W. R. Wollenhaupt
"Lunar Gravity via the Apollo 15 and 16 Subsattelites"
The Moon, 9, 115-128 (1974)
4. M. Ananda, J. Lorell and W. Flury, "Lunar Farside
Gravity: An Assessment of Satellite-to-Satellite
Tracking Techniques and Gravity Gradiometry"
Proceedings of Seventh Lunar Sciences Conference
(15-19 March 1976)
5. R. H. Estes and E. R. Lancaster, "A Simulation for
Gravity Fine Structure Recovery From Low-Low Gravsat
SST Data", Final Report on Contract NAS 5-20901 with
NASA Goddard SFC, Greenbelt, MD 20711
(January 1976)

APPENDICES

- Appendix A - Gravity Gradient Mapping from the LPO - Science Return Simulation Study
- Appendix B - Functional and Physical Description - Gravity Environment Measurement System (GEMS)
- Appendix C - LPOSIM Fortran Program - Simulates the Lunar Polar Orbiter Gravity Gradient Experiment
- Appendix D - Lunar Polar Orbiter Gravity Gradient Experiment Simulation Plots

LPO GRAVITY GRADIENT EXPERIMENT FORTRAN PROGRAM

C
C GRADZZ.FOR
C
C CALCULATES THE VERTICAL GRADIENT OF THE VERTICAL GRAVITY
C OF A SET OF MASS POINTS WHOSE CALCULATED VERTICAL
C GRAVITY FIELD CLOSELY SIMULATES THE LUNAR GRAVITY FIELD
C MEASURED BY APOLLO 16 SUBSATELLITE TRACKING DATA FOR
C THE FRONTSIDE REGION FROM -50 TO +30 DEGREES
C LONGITUDE AND +4 TO +9 DEGREES LATITUDE.
C REFERENCE:
C W. L. SJOGREN, R. N. WIMBERLY AND W. R. WOLLENHAUPT
C "LUNAR GRAVITY VIA THE APOLLO 15 AND 16 SUBSATELLITES"
C THE MOON, 9, 115-128 (1974).
C
C 30 JUNE 1976 VERSION
C
C ORIGINAL PROGRAM WRITTEN BY MR. ROGER W. LOWE
C HUGHES AIRCRAFT COMPANY
C
C REFER QUESTIONS OR COMMENTS TO:
C DR. ROBERT L. FORWARD
C HUGHES RESEARCH LABORATORIES
C 3011 MALIBU CANYON ROAD
C MALIBU, CA 90265
C (213)456-6411 X280
C
C ONE SET OF INPUT DATA ARE THE MASCONS STORED IN
C MASCON.DAT THAT ARE IN A 15X181 ARRAY WITH 15 KM SPACING
C ON THE LUNAR SURFACE.
C THE PROGRAM USES A 9X9 SUBARRAY OF MASCONS TO CALCULATE
C THE GRADIENT AT EACH POINT.
C
C THE OTHER SET OF INPUT DATA ARE THE LARGE DOMINANT MASCONS
C WHOSE MASS AND POSITION ARE STORED IN MASXYZ.DAT.
C
C THE UNITS USED ARE:
C DISTANCES IN KILOMETERS
C MASSES IN MASCONS (10**14 KG)
C GRAVITY GRADIENT IN EOTVOS (10**-9 SEC**-2)
C
C IN THESE UNITS THE NEWTONIAN GRAVITATIONAL CONSTANT IS
C G=6670 EOTVOS KM**3/MASCON

A-3

PRECEDING PAGE BLANK NOT FILMED

```

C
C DIMENSION THE DATA AND OPEN THE FILES
C
      DIMENSION RM(201,35),GRDZZ(15)
      DIMENSION IX(30),IY(30),A(30),W(30)
      OPEN(UNIT=20,FILE='MASCON.DAT')
      OPEN(UNIT=21,FILE='MASXYZ.DAT')
      OPEN(UNIT=22,FILE='GRADZZ.DAT')
C
C READ IN THE SMALL MASCON GRID POINTS
C
      DO 10 I=11,191
      READ(20,1) (RM(I,J),J=11,25)
1    FORMAT(15F5.1)
10   CONTINUE
C
C FOLD OUT A COPY OF THE OUTER 10 POINTS OF THE MASCON
C GRID TO GENERATE A LARGER GRID FOR THE CALCULATION WITH
C A SMOOTH TRANSITION AT THE MEASUREMENT BOUNDARY
C
      DO 20 I=11,191
      DO 15 J=1,10
      RM(I,J)=RM(I,21-J)
15   CONTINUE
      DO 20 J=26,35
      RM(I,J)=RM(I,51-J)
20   CONTINUE
      DO 40 J=11,25
      DO 30 I=1,10
      RM(I,J)=RM(21-I,J)
30   CONTINUE
      DO 40 I=192,201
      RM(I,J)=RM(383-I,J)
40   CONTINUE
      DO 50 I=1,10
      DO 50 J=1,10
      RM(I,J)=RM(I,21-J)
      RM(I,J+25)=RM(I,26-J)
50   CONTINUE
      DO 60 I=192,201
      DO 60 J=1,10
      RM(I,J)=RM(I,21-J)
      RM(I,J+25)=RM(I,26-J)
60   CONTINUE

```

```

C
C READ IN THE LARGE MASCON DATA SET
C IX(I) = X POSITION OF MASCON IN UNITS OF 15 KM
C IY(I) = Y POSITION OF MASCON IN UNITS OF 15 KM
C A(I) = DEPTH OF MASCON BELOW SURFACE IN KM
C W(I) = WEIGHT OF MASCON IN UNITS OF 10**14 KG
C
C DO 70 I=1,30
C READ(21,3,END=80) IX(I),IY(I),A(I),W(I)
C 3 FORMAT(1X,I3,1X,I3,1X,F4.0,F7.0)
C 70 CONTINUE
C 80 NUM=I-1
C
C SET THE ALTITUDE ABOVE THE LUNAR SURFACE
C H= ALTITUDE IN KILOMETERS
C
C H=30.
C
C CALCULATE THE GRAVITY GRADIENT FROM THE 81 SMALLER
C MASCONS IN A 9X9 SUBARRAY ABOUT THE MEASUREMENT POINT.
C X,Y,Z= X,Y,Z DISTANCE FROM MEASUREMENT POINT IN KM
C
C Z=0.-H
C DO 120 I=11,191
C DO 110 J=11,25
C G=0
C DO 100 M=-4,4
C X=M*15.
C DO 90 N=-4,4
C Y=N*15.
C P2=X*X+Y*Y
C R=SQRT(P2+Z*Z)
C G=G+6670.*RM(I+M,J+N)*(2-3*P2/(R**2))/(R**3)
C 90 CONTINUE
C 100 CONTINUE
C
C CALCULATE THE GRAVITY GRADIENT FROM THE
C LARGER MASCON SET.
C
C DO 105 K=1,NUM
C X=(IX(K)-(I-10))*15.
C Y=(IY(K)-(J-10))*15.
C Z=-(A(K)+H)
C P2=X*X+Y*Y
C R=SQRT(P2+Z*Z)
C G=G+6670.*W(K)*(2-3*P2/(R**2))/(R**3)
C 105 CONTINUE

```

```
C
C STORE THE TOTAL INTEGRATED GRAVITY GRADIENT
C FOR THAT MEASUREMENT POINT AND MOVE ON TO THE NEXT
C MEASUREMENT POINT.
C
      GRDZZ(J-10)=G
110 CONTINUE
      WRITE (22,4) GRDZZ
      4 FORMAT(15F5.1)
120 CONTINUE
C
C STOP WHEN FINISHED
C
      STOP
      END
```

LARGE MASCON DATA SET (MASXYZ.DAT)

This is a set of 20 large mass points at various positions and depths below the lunar surface. The first two numbers are the x and y positions of the masses in integer units of 15 Km, the third number is the depth in Km, and the fourth is the mass in units of 10^{14} Kg.

003	013	050.	440.
007	-02	065.	-620.
016	014	045.	-160.
018	-01	085.	970.
027	014	45.	-230.
033	009	45.	-100.
043	011	75.	440.
050	014	40.	-200.
053	006	35.	170.
060	003	60.	-260.
062	016	30.	-250.
067	011	50.	800.
078	010	25.	160.
084	015	55.	900.
090	006	60.	460.
096	013	45.	-470.
101	008	40.	-420.
104	-01	60.	540.
110	007	50.	470.
117	010	75.	540.
119	002	50.	-340.
126	002	75.	-890.
128	012	75.	-1010.
148	007	60.	1100.
160	007	75.	-680.
166	-01	85.	-820.

SMALL MASCON DATA SET (MASCON.DAT)

This is a compacted version of a 15x181 set of mass points that are spaced at 15 Km intervals on the Lunar surface. The units of the mascon masses are in 10^{14} Kg.

-0.4-0.5-0.6-0.7-0.7-0.7-0.7-0.7-0.4+0.0+1.1+1.1+0.7+0.4+1.6
 -0.2-0.5-0.6-0.8-0.8-0.8-0.9-1.1-1.0-0.2-0.0-0.0+0.6-0.5+0.5
 -0.2-0.6-1.2-1.0-0.8-0.8-0.9-1.0-0.4-0.2-0.1-1.4+0.6-0.3+0.1
 +0.1-0.6-1.2-1.0-0.8-0.8-0.9+0.1+0.6-0.8-0.9-0.2+0.4+0.1
 +0.5-0.5-0.7-1.0-0.9-0.8-0.7-0.5+0.1+0.6-0.1-0.1-0.6-0.3+0.0
 +0.4-0.5-1.0-1.0-0.6-0.7-0.4+0.1+0.3+0.5+0.1+0.3+0.0+0.0+0.2
 +0.3-1.0-1.5-0.6-0.5-0.3-0.2+0.3+0.4+0.6+0.6+0.4+0.2-0.1-0.4
 +0.3-1.0-1.1-0.5-0.4-0.3-0.1-0.1-0.0+0.4+0.6+0.7+0.9-0.4-0.5
 -0.4-0.9-0.4-0.3-0.2-0.2-0.1-0.1-0.1+0.0+0.3-0.1-0.5-0.7-0.8
 -0.7-0.5-0.3-0.1+0.0-0.0-0.2+0.0-0.1-0.2-0.5-1.1-1.3-1.6-1.6
 -0.5-0.4-0.1+0.1+0.3+0.1-0.4-0.2+0.0-0.3-1.0-1.6-1.3-1.5-1.9
 -0.5-0.2-0.0+0.6+0.8+0.8+0.5+0.4+0.1-0.4-0.9-1.2-1.3-1.3-1.6
 -0.3-0.2+0.5+1.3+1.6+1.5+1.5+2.5+0.4-0.5-0.8-1.1-1.1-1.0-1.0
 -0.7+0.4+1.1+1.7+1.7+1.9+2.0+1.6+0.5-1.1-0.7-0.8-1.0-0.7-0.7
 -0.2+0.8+1.6+1.9+1.8+1.7+1.6+1.9+0.6-0.7-0.6-0.6-0.9-0.5+0.0
 -0.0+1.1+2.0+1.7+1.5+1.7+1.2-0.6+0.2-0.4-0.7-0.5-0.5-0.2+0.1
 -0.0+0.7+1.5+1.3+1.6+1.8+0.9-0.3+0.2-0.4-0.6-0.5-0.4-0.1+0.1
 +0.2+0.6+1.6+1.0+1.2+1.4-1.0+0.1+0.5+0.0-0.8-0.5-0.4-0.5-0.4
 +0.1+0.4+0.3+0.1-0.8-1.3-0.4+0.0+1.4-1.0-0.8-0.5-0.6-0.6
 +0.3+0.4+0.1+0.3-0.7-2.1-1.2-0.3-0.1+0.5-0.3-0.3-0.6-0.8-1.0
 +0.1-0.1-0.3-0.6-2.5-1.2-0.9-0.4+0.0+0.3+0.4-0.2-0.4-0.8-1.2
 +0.2-0.3-0.6-1.0-1.8-1.1-0.9-0.4-0.1+0.4+1.2+0.3-0.3-0.7-1.1
 +0.0-0.5-0.6-1.6-1.0-0.9-0.8-0.4+0.0+0.5+1.0+0.5-0.2-0.7-0.8
 +0.0-0.5-0.7-1.1-1.0-0.8-0.8-0.4-0.2-0.2+0.1+0.1-0.1-0.2-0.3
 -0.3-0.5-0.8-0.7-0.7-0.6-0.5-0.4-0.5+0.0+0.1+0.1+0.1+0.0+0.2
 +0.0-0.3-0.7-0.8-0.6-0.5-0.4-0.3-0.1+0.1+0.2+0.6+0.1-1.3+0.6
 +0.2-0.3-0.4-0.8-0.6-0.4-0.3-0.1-0.0+0.4+0.5+1.2+0.2-0.6+1.4
 +0.3-0.1-0.3-0.6-0.4-0.3-0.2-0.1+0.1+0.4+0.8+1.1-0.0-1.5+1.2
 +0.7+0.1-0.4-0.4-0.3-0.2-0.1-0.0+0.1+0.4+1.0+0.4-0.1-0.1+0.2
 +0.6+0.1-0.4-0.4-0.2-0.1+0.0+0.1+0.4+0.4+0.6+0.3-0.3-0.3-0.1
 +0.6+0.3-0.5-0.3-0.3-0.1+0.1+0.3+0.7+0.7+0.5-0.2-0.2-0.3-0.3
 +1.0+0.5-0.1-0.3-0.2-0.2+0.0+0.6+1.1+0.8+0.2-0.1-0.3-0.4-0.4
 +1.6+0.7+0.2-0.3-0.2-0.2-0.3-0.2-0.9-0.3-0.9-0.4-0.5-0.8-0.7
 +1.6+1.0+0.2+0.1-0.1-0.3-0.7-0.6-1.2-0.6-0.2-0.6-1.1-0.9-0.8
 +2.0+1.3+1.2+0.7+0.8-0.0-0.2-0.6-1.2-0.5-0.2-0.8-0.9-1.4+0.6
 +2.1+1.6+1.4+1.0+0.7+0.4-0.0-0.4-0.6-0.2-0.3-0.6-1.2-0.5+0.4
 +1.9+1.8+1.5+1.3+1.0+0.6+0.1+0.1+0.1+0.6-0.2-0.6-0.8-0.9+1.7
 +2.1+1.9+1.8+1.6+1.4+0.6+0.6+0.3+0.2+0.1-0.1-0.1-0.3-0.0+0.7
 +2.3+2.0+1.7+1.6+1.6+1.9+1.6+0.8+0.3-0.1+0.0-0.1-0.0+0.5+0.7
 +2.3+2.2+1.9+2.2+2.2+1.9+1.7+1.2+0.3+0.1-0.2-0.2-0.5+0.6+0.5

+2.7+2.1+1.7+1.1+1.3+1.3+1.0+0.5-0.7+0.1+0.1+0.1+0.5+1.0+0.4
+2.8+2.2+1.5+1.2+1.1+1.4+0.9+0.4-0.8-0.3-0.1+0.1+0.5+0.6+0.5
+3.0+1.8+1.3+0.3+0.6+0.7+0.7+0.3-0.7-0.3+0.1+0.2+0.5+0.2+0.2
+2.7+1.5+0.5+0.1+0.1+0.3+0.3-0.3-0.3+0.1+0.1+0.1+0.1+0.3-0.1
+1.9+1.1+0.5+0.1-0.0+0.2+0.3+0.2+0.3+0.6+0.1-0.0+0.9-0.2-1.0
+1.7+0.6+0.6+0.2+0.1+0.2+0.3+0.3+0.5+0.9+0.3-0.1-0.5-0.7-2.1
+1.0+0.8+0.5+0.2+0.1+0.2+0.3+0.4+0.8+1.3+0.1-0.4-0.7-2.3-2.0
+0.8+0.8+0.8+0.8+0.4+0.2+0.3+0.4+1.1+0.4-1.2-0.8-1.2-0.8-1.3
+1.0+1.0+1.0+0.7+0.4-0.1-0.1+0.3+0.5+0.6-0.1-0.9+0.6+0.3-0.2
+1.1+1.3+1.4+0.9+0.4-0.1+0.2+0.4+1.0+0.5-0.1-0.6+0.4-0.0+0.5
+1.1+1.2+1.2+1.1+0.2-0.7+2.2+1.2+1.3+0.5+0.7-1.0-0.2-0.3+0.6
+1.2+1.3+1.0+0.6-0.0-0.2+0.3+0.5+1.1+1.8+0.2-0.8-0.5-0.7-0.3
+1.2+1.2+1.1+0.5-0.3-0.8-0.6+0.2+1.0+1.4+0.3-0.7-1.9-1.1-1.0
+1.0+0.6+0.7+1.4+0.7-0.7-0.4-1.4+0.3+1.2+0.7+1.1-1.0-2.0-0.7
+1.0-0.3-1.6+0.7+0.9+0.0-0.3-0.4-0.6+0.3+0.7+0.6+0.0-1.0+0.3
-0.3-0.9-1.4-1.0-1.0+1.1-0.2-0.3-0.1+0.3+0.8+1.3+0.3-0.0+1.1
-0.3-0.4-1.7-0.7-0.6-1.3-0.4-0.3+0.1+0.4+0.9+0.8+0.5+0.2+1.0
-0.3-0.2-0.6-1.0-0.6-0.4-0.3-0.1+0.1+0.3+1.1+0.8+0.7+0.7+0.8
+0.0+0.9-0.4-0.4-0.5-0.3-0.2-0.1+0.1+0.2+0.7+0.8+0.8+0.6+0.7
-1.4-0.5+0.0-0.4-0.5-0.5-0.3-0.1+0.2+0.4+1.0+0.9+1.0+1.0+0.5
-0.3+0.2+0.9-0.4-0.8-0.8-0.7-0.1-0.4+0.2+2.6-0.4+1.4+1.4+0.8
-0.1+0.1+0.0-0.5-1.5-1.4-0.9-1.2-2.6+4.6+2.6-0.0+1.8+2.2-0.8
+0.3-0.2-0.4-0.8-1.0-1.4-1.8-0.7+1.8+3.0+4.3+0.8+3.9-0.6-3.9
+0.9+0.2-0.7-1.2-1.0-1.2+1.9-0.4-1.0+2.0+2.4+2.4+4.2-6.6-1.8
+0.3+0.4-1.1-1.5-1.4-2.0+1.7-2.9+2.1+1.0+0.3+1.9+3.9-0.2-1.6
+0.2+0.0-0.5-1.4-1.8-0.8+0.2+0.7+3.4+0.4-0.6-1.2+3.7+2.0-2.0
+0.1-0.1-0.6-1.7-2.3-1.4+0.2+1.3+1.6-0.2-1.5-0.0+1.3+3.7+0.9
+0.0-0.2-0.7-1.6-2.6-1.9+0.7+2.0+1.4+0.3+0.1+0.5+1.7+3.6+1.7
+0.0-0.2-0.7-1.5-2.5-2.3+0.2+1.9+1.0+1.1+1.0+2.0+1.9+2.4-0.4
+0.2-0.1-0.7-1.4-2.3-1.4-0.6+0.7+0.6+1.1+0.9+2.3-0.9+1.2-0.8
+0.0-0.2-0.6-1.5-3.0-0.1-2.5+1.5+0.6+1.8+4.9+0.9+0.7-0.4-0.8
+0.0-0.1-0.2-0.5-0.7-1.1-1.4-0.6-0.5-1.9+1.0-0.4-0.5-0.3-0.5
+0.0-0.3+0.1+0.3+0.8-1.3-1.3-0.6-0.6-1.1+2.4-0.2+0.0-0.3+0.0
-0.2-0.5+0.5+1.4+1.7+2.8-1.6-0.6-0.0+2.8+1.6+0.3-0.2-0.4+0.1
-0.0+0.4+1.0+1.7+2.4+4.9-0.0-1.3-0.1+4.3+2.7-0.7-0.2-0.2+0.6
-0.0+0.8+1.7+2.2+2.0+2.9+1.8+3.7+2.9+2.6+2.7-0.1-0.9+0.1+1.1
-0.3+2.3+1.8+1.6+1.4+2.5+2.2+2.5+0.8-1.0+1.1-0.2-0.3-0.0+1.8
-1.5-0.7+0.7+1.4+1.3+1.2+1.5+0.7-1.6-1.0-0.5+0.3-0.1+0.7+2.1
-1.0-1.0+0.1+0.5+0.8+0.8+0.3-1.3+0.7-1.3+0.4+0.9+0.4+0.4+2.7
-1.1-1.2-0.1+0.1+0.3+0.3+0.1-0.8-1.4+1.4+0.9+1.8+1.4+2.0+3.6
-1.0-1.5-0.2+0.0-0.1+0.1+0.6-1.1-0.8+0.2+1.2+0.9+1.0+1.6+2.8
-1.1-1.6+0.2-0.1+0.3+0.7+0.3-1.0-1.3-0.1+0.9+0.4-0.2-0.8+1.2
-1.2-1.9-0.3-0.2+1.2+0.9+0.1-0.8-1.8-0.2-0.1-0.0-0.0+0.2+1.2
-1.7-0.5-0.1+0.8+1.0+0.5+0.2-0.5-1.4-1.5-0.6-0.2+0.1-0.7-0.0
-0.7-0.2+0.6+0.9+0.5+0.2+0.1-0.5-1.6-1.6-0.9-0.4+0.5+0.7+0.3
-0.4+0.3+1.1+0.2-0.0-0.1-0.3-0.5-1.1-1.7-1.5-0.9+0.5+0.4-0.2
+0.1+0.1+0.3-0.1-0.2-0.4-0.5-0.7-1.0-1.7-2.6+0.2-0.8+1.3+1.0
+0.1+0.2+0.0-0.5-0.9-0.5-0.7-0.9-0.3-0.1-3.5-1.7+1.5+1.7+2.9
+0.1+0.2-0.1-1.2-1.3-0.6-0.8-0.9-0.8-2.8-3.8-2.4-1.7+0.6+2.0
+0.3+0.1-0.4-2.5+3.7-0.7-0.8-1.1-1.1-1.3-3.3-1.7-1.1-1.8+1.3

+0.6+0.4+0.0-1.4+0.4-0.7-0.9-1.1-0.8-2.4-3.6-3.1-2.0-2.0+0.6
+0.9+0.8+0.3+0.0+0.1-0.7-0.8-1.1-0.2-2.9-3.4-2.4-2.7-1.1+0.6
+0.9+1.0+0.8+0.7-0.1-0.5-0.9-1.1-1.5-2.1-2.5-1.4-1.7-2.1+0.4
+0.8+0.9+1.3+1.0-1.1-0.5-0.8-0.7-0.5-3.7-1.4+0.3+0.6-0.4+0.5
+0.6+0.8+1.1-0.2-1.2-1.4-1.2-1.0-1.0-2.2-1.2+0.8+2.3+1.7-0.0
+0.3+0.6+0.2-0.5-1.1-1.9-1.3-1.3-1.7-2.5-0.5+1.4+1.7+2.0+0.9
+0.2+0.5+0.2-0.4-2.9-1.9-1.5-1.1-1.0-1.3+0.5-1.7+1.8+0.9+0.6
-0.0+0.5-0.1+1.0-3.5-1.4-0.8+0.7-1.4+0.3+0.3-1.4-0.5-0.8-0.1
+0.1+0.2+0.3-0.9-3.5-0.8+0.1-2.0-3.6+3.5+3.5+0.3-0.5-0.7-0.9
-0.0+0.6-0.3-1.3-2.9-0.3+0.3+2.2-0.7+5.3+0.3+0.3-0.3-1.4-1.6
-0.0-0.0+0.6-0.6-2.2-0.2+0.6-1.3+1.3+5.1-0.4+0.0-0.6-1.1-1.3
-0.1+0.3-0.0+0.9-1.3-0.9-1.0-3.0+4.9+2.4-0.7-0.8-0.8-1.0-1.8
-0.6+0.1+0.4+0.5-1.2-0.9-1.6-1.4+1.4+0.8-0.7-1.3-1.0-0.8-1.4
-0.2+0.3+0.7+1.0+4.3-0.4-3.3-1.9-1.7-1.9-2.2-2.0-1.4-0.8-1.3
-0.4+0.1+0.9+1.6+0.2+0.1-1.8-0.5+0.3-4.9-3.9-3.0-1.3-0.8-1.2
-0.1+0.4+1.3+2.3+1.4+0.8+0.2-0.1+1.2-4.9-4.7-2.6+0.2-0.5-1.3
+0.1+0.7+1.2+2.0+2.3+1.6+0.2-0.8-1.3-2.8-3.6-2.3-0.1-0.8-1.8
-0.4+0.1+1.0+1.1+1.8+2.0+0.7-0.3-0.6-1.8-2.8+1.2-0.6-1.2-1.4
-1.6-0.2-1.0+0.0+0.7+1.0+0.1-0.9-0.1-0.7-1.3-0.2-1.3-1.3-1.5
-2.9-2.2-1.3-2.0-0.9+0.2-0.0-0.3+0.1+0.5-0.3-0.6-2.2-1.4-1.9
-4.5-1.5-1.3-2.1-1.3+0.5-0.1-0.1+0.2+1.0-0.0+0.2-2.4-1.3-1.9
-5.3-2.9-0.5-1.6-2.6-0.7+0.8+0.5+1.3+2.8+0.2-0.5-3.2-1.0-2.1
-3.9-3.4-2.2-0.4-1.6-1.2-0.6+1.3+1.8+2.5+0.8+0.2-2.7-2.0-2.5
-3.1-3.3-3.1-0.5-0.9-1.8-0.4+0.4+1.9+2.0+0.6+1.1-2.4-1.7-2.2
-2.4-2.6-2.7-2.1-0.8-1.7-3.3-0.1+1.7+1.6+0.6+0.8-1.8-1.7-1.8
-1.7-2.0-2.3-2.3-2.2-2.4-3.3-1.9+1.1+0.8+0.4+0.4-0.6-1.2-1.6
-0.6-1.4-2.4-3.2-2.6-2.6-1.8-5.5+0.7+0.6+0.5+0.7-0.4-1.0-1.6
+0.6-0.4-0.9-2.1-2.4-2.8-3.2-3.4-0.4+1.3+0.6+0.8-0.1-1.1-2.0
+1.0+0.8+0.4-1.0-2.8-2.5-2.9-3.1-1.2+1.3+0.2+0.5+0.0-1.3-1.5
+1.0+1.0+0.5-0.9-2.0-2.5-2.1-2.5-0.7+1.0+0.9+1.1+0.5-0.4-1.6
+0.5+0.5+0.1-0.8-2.5-2.6-1.3-0.8+0.5+2.4+1.6+2.5-1.2-1.8-1.7
+0.5+0.3+0.2-0.6-2.5-2.5-0.9-0.1+0.6+1.0+0.1-0.8-1.1-1.5-5.2
+0.5+0.3+0.5-0.1-2.2-2.4+1.4+1.2-0.0-1.6-0.8-0.1-0.4-1.0-1.0
+0.3+0.3+1.5+0.5-1.6-2.2+3.1+1.1-0.1-1.0-1.7-3.1-3.7-3.3-1.6
+0.6+0.5+0.1-0.1-1.4+2.1+3.1+0.2-0.0-0.9-1.0-1.6-2.3-2.0-1.3
+0.9+0.3-0.9+0.5+2.5+2.3+1.4+0.5+0.1-0.3-0.5-0.9-1.1-0.5-0.9
+0.6+0.2+0.3+0.1+2.8+2.9-0.2+0.3+0.3+0.0+0.1+0.1+0.1+0.4-0.4
+0.2+0.1-0.0+1.1+3.2+0.9-0.5+0.2+0.2+0.1-0.4+0.7+3.1+1.9+0.7
-0.2-0.3-0.6+0.5+0.6-1.5-1.2-0.7-0.7-0.4-0.2-0.2+2.6+2.4+1.5
-0.3-0.6-1.0-0.3-0.8-2.0-1.6-1.5-1.3-1.0-0.5+0.7+2.4+2.3+1.2
-0.6-1.0-1.4-1.4-1.9-2.7-1.9-1.7-2.2-1.5-1.0-0.5+1.8+1.4+0.4
-1.0-1.4-1.7-1.9-2.4-2.3-1.9-1.6-2.4-2.0-1.8-1.2+0.2+0.8+0.2
-1.7-1.9-2.0-2.3-2.3-1.4-1.5-2.0-2.0-3.0-2.6-1.9-0.5+0.1+0.0
-1.9-2.1-2.2-2.6-2.6-2.0-1.9-1.8-1.8-2.2-2.8-1.1-0.9+0.0-0.6
-1.8-2.1-2.5-2.8-2.7-2.4-2.1-1.8-1.8-2.1-1.9-1.7-1.8+0.4-1.7
-1.9-2.1-2.2-2.3-2.9-2.5-2.2-1.7-1.4-1.7-2.0-1.8-1.6-0.8-1.2
-1.7-2.0-1.9-2.2-2.1-2.1-2.0-1.8-1.5-1.5-1.7-1.8-1.7-1.4-1.6
-1.0-1.3-1.8-1.8-2.1-2.1-1.8-1.3-1.2-1.1-1.4-1.9-2.0-2.1-1.6
-0.1-0.1+0.3+0.7+1.0+0.6-0.5-0.4-0.9-1.1-1.2-1.3-1.6-1.7-1.4
+1.0+0.8+0.9+0.4-0.1-0.1-0.1-0.1+0.1-1.5-1.0-0.9-1.0-1.3-1.3

+0.8+1.5+1.7+1.6+0.7+0.3-0.1-0.2-0.3-0.5-0.5-0.6-0.6-0.7-0.4
+2.1+2.5+2.2+1.9+1.1+0.7+0.1-0.9-0.3-0.3-0.1+0.0+0.2-0.8-0.9
+2.5+2.8+2.3+2.2+1.8+1.4+0.1-0.1-0.2-1.0-0.1+0.1+0.4+1.1+0.3
+2.6+2.6+2.6+2.3+1.9+0.8-1.0-1.0+0.2+0.9+0.1+0.6+0.9+0.9+1.0
+2.5+2.3+2.3+2.0+1.5+0.5-1.6-1.8-1.6-0.4+0.3+1.5+1.3+1.2+1.3
+1.8+2.1+2.3+3.1+1.1+0.3+2.0-1.1-1.1-0.8+0.3+1.1+1.4+1.7+1.6
+0.5+1.7+1.6+1.3+0.7-1.8-0.4-0.3-0.6-0.8+0.4+1.1+1.7+2.2+2.3
-0.0+2.1+1.0-0.8+1.8-2.1+1.3-0.4-0.4-0.9+0.5+1.5+1.6+2.1+2.3
-0.6+1.4+0.5-0.7+1.5-0.3-1.6-1.7+0.6-0.4+0.6+1.1+1.7+1.9+2.4
-0.0-0.2+0.1+0.1-0.0-0.6-0.7-0.4+0.1+0.2+0.5+1.0+1.6+1.8+1.9
-0.1-0.1-0.7-0.0+0.5+0.8+0.4+0.5+0.5+0.3+0.4+0.7+0.7+1.3+1.8
-0.1-0.2-0.2-0.1+1.3+1.0+0.4-0.2+0.1+0.6+0.7+0.4+0.7+1.0+1.4
-0.2-0.3-0.3-0.6-0.1-0.1-0.5+1.0+0.7+0.0-0.1+0.1+0.3+0.7+1.2
-0.3-0.8-1.5-0.3+0.7+0.5+0.3+0.1-0.5-0.6-1.0-0.8-0.7-0.4+0.7
+0.2-0.8-0.7-0.3-0.1+0.2+0.1-0.6-0.8-1.7-1.9-0.9-0.4-0.2-0.0
+0.3-1.4-1.0+0.5+0.0+0.0+0.6-0.3-0.3-1.1-1.1-0.8+0.1-0.1+0.0
-0.8-1.8-1.6+0.1+0.2-1.3+0.3+0.4-0.5-1.5-2.0-0.8-0.4-0.1+0.0
-1.1-2.5-1.3-0.7-1.1-0.2+0.2+0.3-0.7-2.0-2.3-0.3-0.8-0.1+0.1
-1.6-2.0-1.8-0.4-0.1+0.1+1.1+0.1-0.6-1.9-2.1+0.1-0.5+0.6+0.2
-0.4-2.4-1.3-0.5+0.1-0.3+0.4+0.3-0.3-1.0-0.8-0.2-0.2+0.6+0.5
-1.9-1.3-0.8-0.5+0.1-0.2+0.0+0.3-0.2-0.2-0.3-0.5+1.7+0.8+0.5
-1.2-0.8-0.6-0.1-0.3-0.3-0.2-0.1+0.1+0.5-0.1+0.5+1.4+1.1+0.3
-0.7-0.5-0.4-0.3-0.3-1.4-0.6-0.3-0.2-0.1-0.7+0.3+1.1+1.4+0.4
-0.4-0.2-0.3-0.3-0.2+0.4-0.3-0.3-0.3-0.4-1.1-0.0+1.0+1.0+0.4
-0.2+0.0-0.2-0.2+0.0+0.0-0.3-0.3-0.5-0.7-0.9-0.2+1.1+0.7-0.0
+0.0+0.0+0.0+0.0+0.2-0.2-0.4-0.5-0.7-1.0-1.1-0.3+0.5-0.2-0.5
-0.0+0.0-0.2-0.4-0.3-0.1-0.4-0.7-0.8-1.0-1.4-0.2+0.4-0.9-1.9
+0.5+0.1-0.3-0.5-0.3+0.5-0.3-0.8-1.0-1.2-1.2-0.9-1.3-2.0-1.8
-0.2-0.5-0.6-0.8-0.3+0.0-0.2-0.5-0.9-1.3-1.4-1.5-1.7-1.7-1.9
-0.6-0.8-0.9-1.6-0.6-0.2-0.5-0.7-1.1-1.5-1.5-1.6-1.9-1.8-1.9
-1.1-1.2-1.2-2.1-0.3-0.3-0.6-0.7-0.9-1.2-1.6-1.9-2.1-2.3-2.1
-1.3-1.5-1.6-1.1-0.8-0.7-0.7-0.8-0.8-0.9-2.1-2.9-3.5-0.1-0.9
-1.8-1.8-1.4-0.8-0.8-0.7-0.7-1.0-0.7-0.6-1.1-0.7+1.0+0.3-0.2
-2.0-1.9-1.3-0.9+0.2-0.7-0.7-0.6-0.5-0.6-0.4-0.0+0.9+0.8+0.2
-2.1-2.2-1.6-0.5-0.1-0.4-0.5-0.4-0.3-0.5+0.3+0.9+0.9+0.6+0.2
-2.1-2.4-2.2-0.6-0.3-0.5-0.5-0.3-0.1+0.4+0.7+0.6+0.6+0.6+0.3
-2.4-2.7-2.5+0.0-0.7-0.6-0.6-0.3+0.1+0.8+0.4+0.5+0.6+0.5+0.4
-2.5-2.8-1.8-0.2-0.7-0.6-0.8-0.2+0.4+0.5+0.5+0.5+0.5+0.5
-2.3-2.3-1.6-0.4-0.7-0.6-0.5-0.2+0.2+0.7+0.5+0.5+0.6+0.6+0.5
-2.3-1.9-1.3-0.5-0.7-0.7-0.9-0.1+0.7+0.4+0.5+0.5+0.6+0.5+0.5
-2.0-1.7-0.8-0.7-0.8-0.6-0.6+0.1+0.5+0.4+0.6+0.6+0.6+0.6+0.5



RESEARCH REPORT 495

GRAVITY GRADIENT MAPPING FROM THE LPO
— SCIENCE RETURN SIMULATION STUDY

Dr. Robert L. Forward
Senior Scientist

February 1976

* Work supported in part by JPL Contract 954309

A-13

PRECEDING PAGE BLANK NOT FILMED

TABLE OF CONTENTS

SECTION		PAGE
I	INTRODUCTION	A-18
II	THE LUNAR MODEL	A-21
III	LUNAR POINT MASS MODEL	A-22
IV	GRAVITY FIELD OF THE LUNAR POINT MASS MODEL	A-24
V	DOPPLER VELOCITY DIFFERENCE FROM THE POINT MASS MODEL	A-27
VI	GRAVITY GRADIENT OF THE POINT MASS MODEL	A-36
VII	GRAVITY PLOTS FROM GRADIENT PLOTS	A-48
VIII	EFFECTS OF SYSTEM NOISE ON CONTOURS	A-55
IX	GRAVITY MEASUREMENT AT HIGHER ALTITUDES	A-59
X	SUMMARY	A-63
	REFERENCES	A-65
	APPENDIX A — Rotating Components of the Tensor Gravity Gradient Field of a Point Mass from the Point Mass Coordinate System to a Measurement Point Coordinate System	A-66

PRECEDING PAGE BLANK NOT FILMED

LIST OF ILLUSTRATIONS

FIGURE		PAGE
1	Vertical gravity contour plots	A-25
2	Doppler velocity and velocity change contour plots	A-29
3	Doppler velocity change in 15 km sampling interval	A-33
4	Strength of vertical component of field as a function of horizontal separation	A-38
5	Vertical gradient of vertical gravity contour plots	A-39
6	Gravity gradiometer instrument output contour plots	A-45
7	Vertical gravity integrated from horizontal gradients	A-53
8	Effect of noise on contour plots	A-57
9	Comparison of Doppler and gradients at 100 km	A-61

ABSTRACT

Simulations of the gravity data to be expected from a Lunar Polar Orbiter spacecraft utilizing either a Doppler velocity tracking system or a gravity gradiometer instrument system are generated using a point mass model that gives an excellent representation of the types of gravity anomalies to be found on the moon. If the state of the art in instrumentation of both systems remain at the level of ± 1 mm/sec at 10 sec integration time for the Doppler velocity system accuracy and at ± 1 Eotvos[†] at 10 sec integration time for the gravity gradiometer system accuracy, inspection of the simulations indicates that a gravity gradiometer system will give science data with better resolution and higher amplitude-to-measurement noise ratio than the Doppler velocity system at altitudes below 100 km. The error model used in the study is one where the system errors are assumed to be dominated by the point measurement noise and data quantization noise. The effects of other, more controllable, systematic error sources are not considered in this simplified analysis. For example, both systems will be affected by errors in LPO orbital altitude and position knowledge, spacecraft maneuvers, and data reduction errors. In addition, a Doppler tracking system will be sensitive to errors produced by spacecraft acceleration (from outgassing or solar pressure) and poor relative position of the LPO, Relay Satellite and ground tracking station, while a gravity gradiometer system will be sensitive to errors from spacecraft attitude and angular rates. These preliminary study results now need to be verified by a more complete error analysis in which all the uncertainties of the data gathering process are formally mapped into uncertainties in the resulting gravity maps.

$$^{\dagger} 1 \text{ Eotvos} \equiv 10^{-9} \text{ sec}^{-2} = 10^{-9} \text{ gal/cm} = 0.1 \text{ mgal/km} = 10^{-10} \text{ g's/m.}$$

I. INTRODUCTION

To date, the information that we have on the gravity field variations of the moon (and the rest of the bodies in the solar system) has come from measurements of the changes in velocity of a spacecraft passing by the body, usually by measurement of the Doppler frequency shifts in the spacecraft transmitter carrier frequency. This technique requires the constant use of a ground tracking station during data collection and results in a measurement of one component of the gravitational force field (that component along the line of sight to the tracking station). However, since nearly constant tracking was usually needed for other purposes and the modifications to the spacecraft transmitter to stabilize it for use in a Doppler tracking system were minor, the gravity data was essentially "free," except for the costs of processing the data.

In the coming years, it is proposed to use a Lunar Polar Orbiter spacecraft to carry out a complete, high resolution survey of the moon from a low polar orbit. One of the more important physical parameters to be obtained from the LPO mission is a high resolution gravity map, for gravity is one of the few means for obtaining subsurface geophysical information.

The presently used gravity measurement technique using earth tracking stations will only give gravity information on the front side of the moon, thus, in order to obtain a complete gravity survey of both frontside and backside using the Doppler velocity tracking technique, it will be necessary to add an 86 kg Relay Satellite to the mission. In the present preliminary mission design, [1] the Relay Satellite will be in a high equatorial orbit and the LPO in a near polar orbit. The orbit configurations are such that only 60% of the LPO backside passes can be tracked with the Relay. Thus, to obtain a complete, high resolution (15 to 30 km), gravity survey of both frontside and backside will require months of ground station tracking time carefully chosen ahead of time to cover the backside gaps caused by the occasional poor position of the Relay Satellite. The resultant gravity data will consist of only vertical

and east-west gravity components near the equator, and only horizontal components near the pole.

An alternate technique exists for the measurement of the lunar gravity field. This involves measuring the gradients of the gravity with instrumentation onboard the spacecraft. There are four instrumental approaches to the instrumentation and the state of development of three of them^[2, 3] is such that they can be considered as candidate instruments for the LPO. Despite some current misconceptions,^[1] all the gradiometer instruments can be placed anywhere on the spacecraft, will operate satisfactorily at the spacecraft attitude rates presently planned, and will have minor spacecraft interface problems. If the gradiometer system used is a complete one and measures all the components of the gravity gradient tensor, then accurate knowledge of the spacecraft attitude or altitude is not needed since it can be extracted from the gradient data.

The purpose of this paper is not to debate the relative engineering merits of the various instrumentation techniques for measurement of the gravity field of the moon, but to address the question:

Suppose both a Doppler velocity tracking system with an accuracy of ± 1 mm/sec at 10 sec and a gravity gradiometer system with an accuracy of ± 1 Eotvos at 10 sec were equally available, what would be the scientific return we could expect from the two systems and how do they compare?

We will address this question by carrying out a simulation of a Doppler velocity system response and a gravity gradiometer system response to a point mass model that produces a gravity field that closely resembles an actual lunar gravity field. In order to keep this paper within bounds, we will use a simplified error model where the total errors are assumed to be dominated by the point measurement (instrumentation) noise and the data quantization noise. A real system noise level will also have contributions from other sources. Both systems will be affected by errors in LPO orbital altitude and position knowledge, spacecraft maneuvers, and data reduction errors. In addition, a Doppler tracking

system will be sensitive to errors produced by spacecraft acceleration (from outgassing or solar pressure) and poor relative position of the LPO, Relay Satellite and ground tracking station, while a gravity gradiometer system will be sensitive to errors from spacecraft attitude and angular rates. These error sources will typically produce errors with very long (1 to 3 per orbit) or very short (< 10 sec) period characteristics and should be separable from the desired lunar data (5 to 500/orbit).

However, in the sense that these error sources have not been modeled, this is a preliminary study that needs to be verified by a more complete error analysis in which all the uncertainties of the data gathering process are formally mapped into uncertainties in the reduced gravity data.

II. THE LUNAR MODEL

Since one purpose of the study is to investigate the high resolution capability of the gravity measurement systems, it was desirable to generate a lunar gravity model that had high resolution features in it and at the same time was a reasonable model for the kind of gravity variations we expect to see above the lunar surface.

Fortunately, lunar gravity data of high resolution and dense coverage (and therefore relatively high accuracy) were obtained over a small section of the lunar frontside during the Apollo 16 mission. In the paper "Lunar Gravity via the Apollo 15 and 16 Subsattellites," by Sjogren, Wimberly and Wollenhaupt^[4] there is a section of Apollo 16 subsattellite data from -50 to +30 degrees longitude and +4 to +9 degrees latitude where the Apollo 16 Subsattellite was well below 20 km from the lunar surface. Since the Apollo 16 subsattellite had an inclination of only 10 degrees, the track spacing was very close, and even with tracking limited to every third orbit, the data was obtained at 15 km intervals. In all, about 58 orbits and 10,000 20 sec observations were available. The system accuracy quoted was 1 mm/sec for each 20 sec observation point. The Doppler data was smoothed with a 1 min long spline fit and then the spline fit analytically differentiated to obtain an estimate of the gravity at approximately 15 km intervals. The resultant contour plot is the line-of-sight acceleration of the spacecraft at the spacecraft altitude. For the central portion of the data this turns out to be very close to the vertical component of the gravity vector at about 15 km altitude.

Because this available data set had a number of interesting high resolution features it was decided to utilize this data as a starting point for the generation of a lunar gravity model. Unfortunately, the data set itself, consisting of only the vertical gravity component at only one altitude is a little difficult to utilize if we wish to predict the total gravity vector, the Doppler velocity, and gravity gradients in different directions than vertical and at other altitudes than 15 km.

III. LUNAR POINT MASS MODEL

To provide the basic gravity anomaly model for our simulations, we generated a lunar point mass model consisting of 28 large point masses buried at various points under the lunar surface and a grid of smaller point masses spaced every 15 km along the lunar surface. These masses were adjusted by an iterative process until the vertical gravity field at 15 km altitude calculated from the point mass model had a reasonable resemblance to the Apollo 16 data in the region from -22° to $+27^{\circ}$ longitude and $+2^{\circ}$ to $+9^{\circ}$ latitude. Although an excellent fit was obtained (no point more than 2 milligals off and the rms variation less than 0.6 mgal), the fit was not important to the simulation effort since all we really needed to start with was a lunar gravity anomaly model that was reasonable in amplitude and harmonic variation for the moon, and was not so unlike the real lunar variations as to cause questions about the validity of the simulation results. In the same vein, although we have found a mass point distribution that does a reasonable job of reproducing the vertical gravity field variations, it is by no means the only mass point distribution, and its nonphysical nature makes it of little value for interpretation of the lunar features, which should most likely be modeled with rings and discs.

As a check on the validity of the point mass model as well as the cutoff points for the computer algorithm, we calculated the horizontal gravity gradients (Γ_{zx} and Γ_{zy}) at 15 km altitude using the point mass model and compared it with the same gradients calculated by differentiating the original gravity data set, and again obtained excellent agreement. Other checks for internal consistency were also made, such as calculating the horizontal gradients of vertical gravity at 30 and 60 km altitude and checking against the horizontal differences of the vertical gravity calculated at that altitude. (This check showed that a 9×9 array of surface mass points contributing to each gravity point were sufficient for internal consistency.) Once the mass point model had been generated and checked for consistency, we could then use it to calculate any

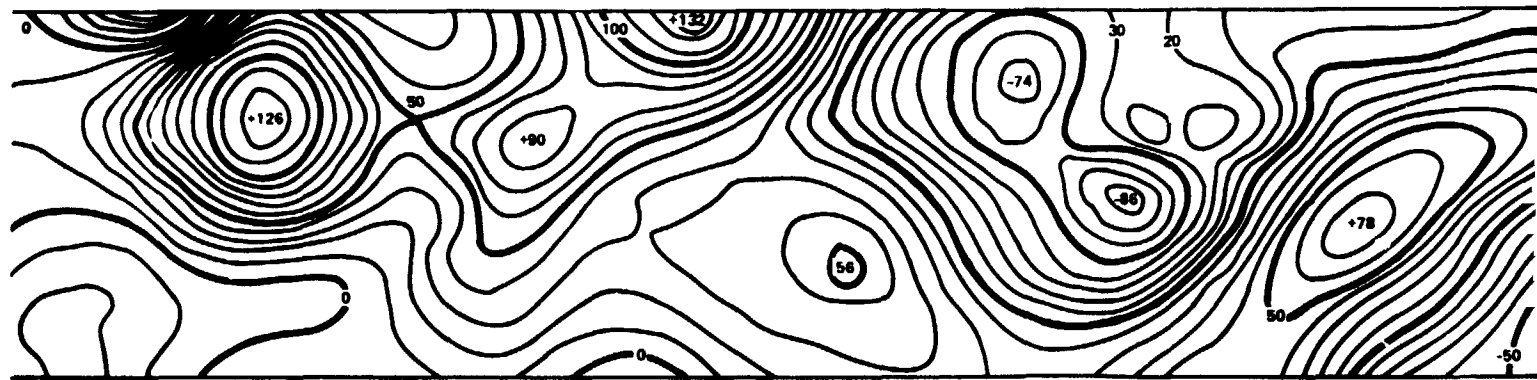
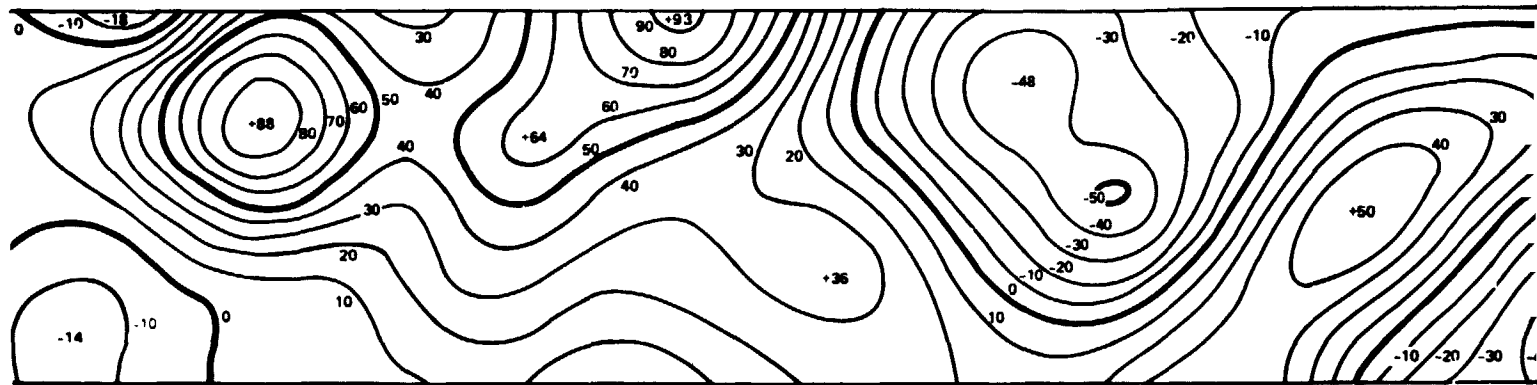
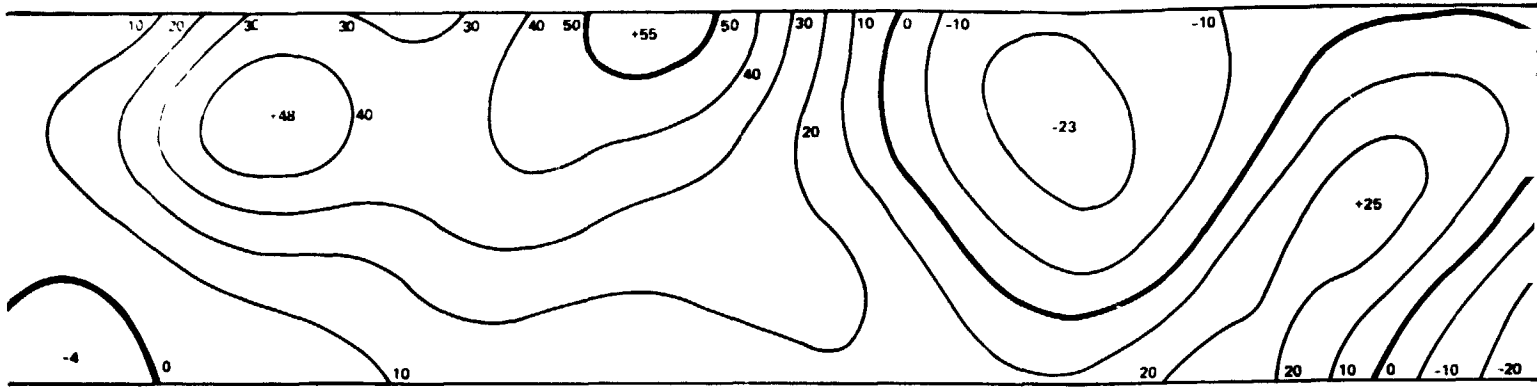
component of any quantity (three components of the gravity and doppler velocity vectors, and nine components of the gravity gradient tensor) at any altitude higher than the original data set (~ 15 km) with a high degree of confidence that it would give a reasonable approximation to the kinds of gravity anomaly variations and measurement system outputs we would expect to find over the moon.

IV. GRAVITY FIELD OF THE LUNAR POINT MASS MODEL

As a starting point, we first calculated the vertical component of gravity from the mass point model at three different altitudes, 15, 30, and 60 km. These are shown in Fig. 1. The original lunar data set is at the bottom for comparison. These were all contoured at 10 mgal intervals. With increasing altitude, we see the expected decrease in resolution. This is most evident in the two lobed depression with two adjacent subsidiary small depressions in the region around -2° longitude. The small depressions are seen at 15 km altitude and disappear at 30 km altitude, then at 60 km altitude the two strong depressions have merged into a single, slightly oval region.

Since there is no instrument that can measure gravity directly in the free fall environment of an orbiting spacecraft, these curves do not represent the output of any particular instrument, but only give us a feeling for what we can expect from the reduction of the data obtained from systems that measure the integral or derivative of the gravity field.

92. VERTICAL GRAVITY CALCULATED FROM POINT MASS MODEL, mgal



92. VERTICAL GRAVITY FROM APOLLO 16 SUBSATELLITE, mgal (SJOGREN, ET AL)



-22°

-10°

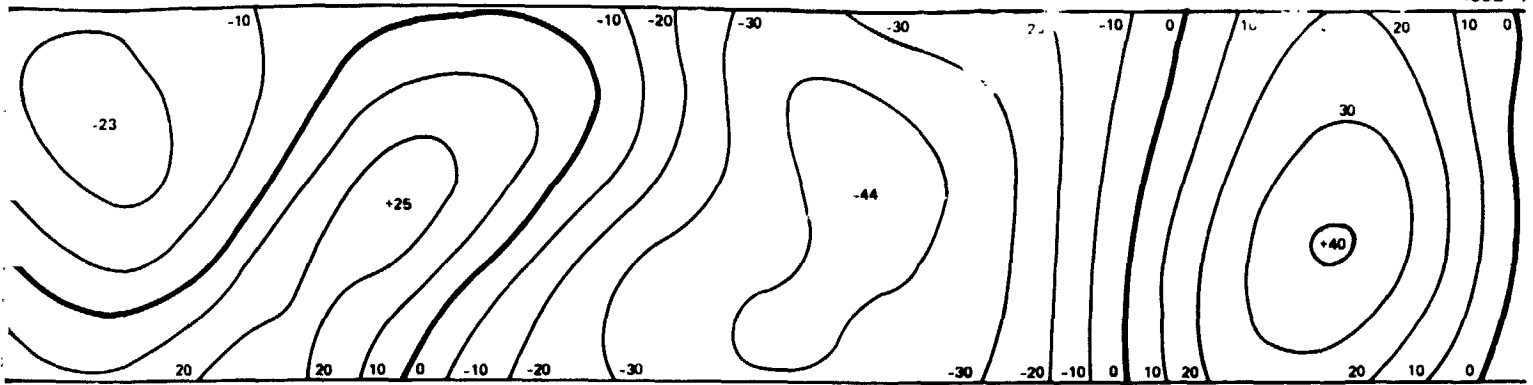
0°

LONGITUDE

FOLDOUT FRAME /

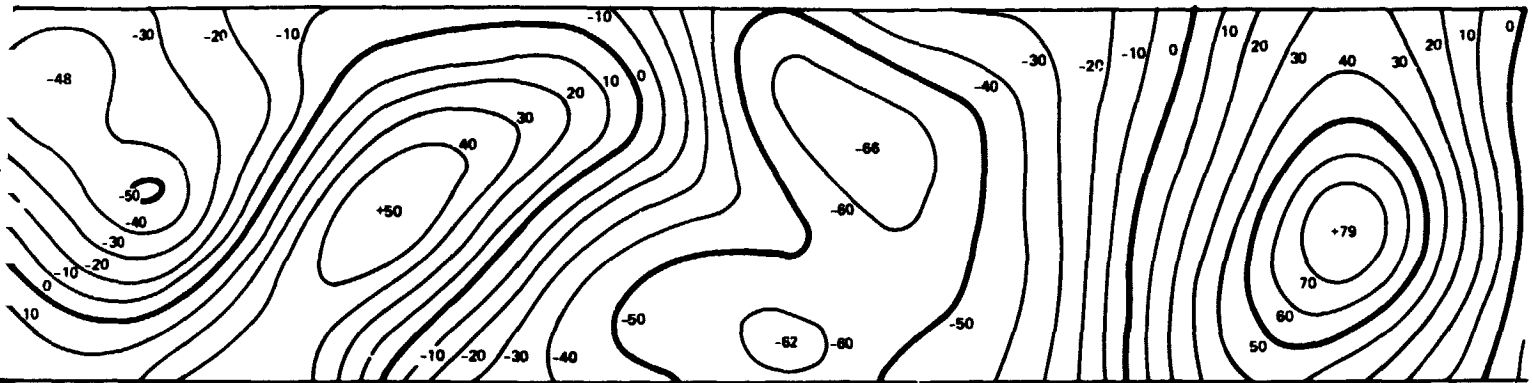
60 km ALTITUDE

4652-7



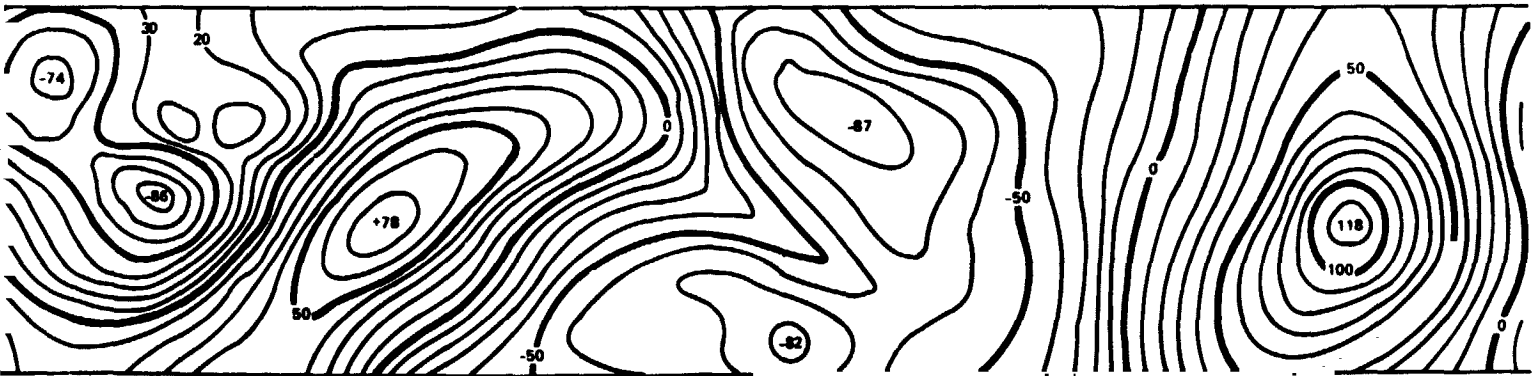
30 km ALTITUDE

4652-8



15 km ALTITUDE

4652-9



EN, ET AL)

13 - 20 km ALTITUDE

4652-10



0° +10° +20° +270°

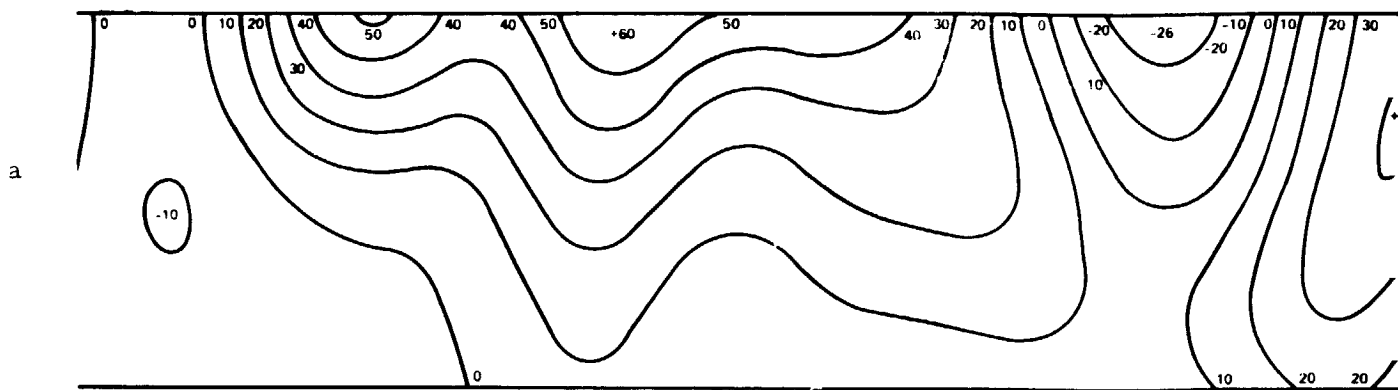
LONGITUDE

V. DOPPLER VELOCITY DIFFERENCE FROM THE POINT MASS MODEL

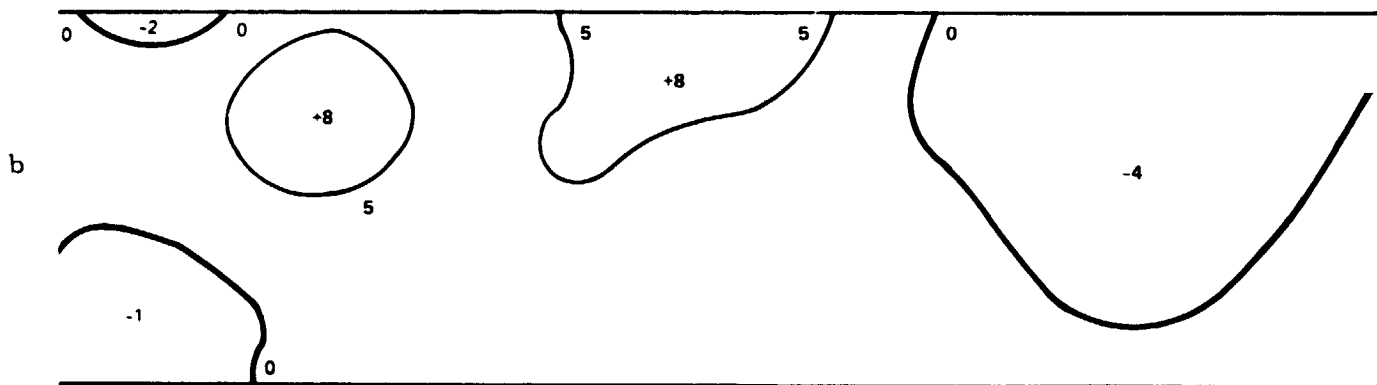
We next calculated the effect of the point mass model on the velocity of an orbiting spacecraft. A spacecraft in low polar orbit around the moon has a velocity in the near north (south) or x (-x) direction of approximately 1.7 km/sec. If we wish to obtain high resolution data ($1/2^\circ$, 30 km wavelength or 15 km resolution), then the spacecraft will pass over the 15 km resolution cell in approximately 8.8 sec. The present state of the art in Doppler velocity tracking is an accuracy of ± 1 mm/sec for a 10 sec averaging time. Thus, data taken every resolution cell will have a comparable accuracy. Until more definitive information on the exact performance of an LPO tracking system is available, we will use this noise value of ± 1 mm/sec per 15 km resolution cell in our calculations.

Now, the exact velocity of the spacecraft at any point will consist primarily of the dominant orbital motion plus small perturbations that are the integral of all the gravity anomaly forces that have acted on the spacecraft. If we were to calculate the effect of the point mass model on the velocity of the spacecraft and plot the resultant velocity directly, we would obtain a plot with smoothly varying, gradually sloping contours (see Fig. 2(a)). To obtain a measure of the gravity field from this Doppler velocity plot, it would be necessary to differentiate the velocity to find the velocity change as a function of time (see Fig. 2(b)). With real data, this is normally done not by subtracting adjacent velocity measurements and dividing by time as we did to get Fig. 2(b) from Fig. 2(a), but by fitting a cubic spline fit curve to a set of points (typically 6) about the point of interest, and then analytically differentiating the spline fit curve to obtain the derivative of the Doppler velocity, which is the acceleration. This procedure has the advantage that it allows for a smooth derivative to be taken and averages out the effects of the noise at a single measurement point, but the disadvantage that it also smooths out real gravity variations of high frequency, thus lowering

v_z , DOPPLER VELOCITY, mm/sec



Δv_z , VERTICAL DOPPLER VELOCITY CHANGE, mm/sec CHANGE IN 15 km



g_z , VERTICAL GRAVITY, mgals

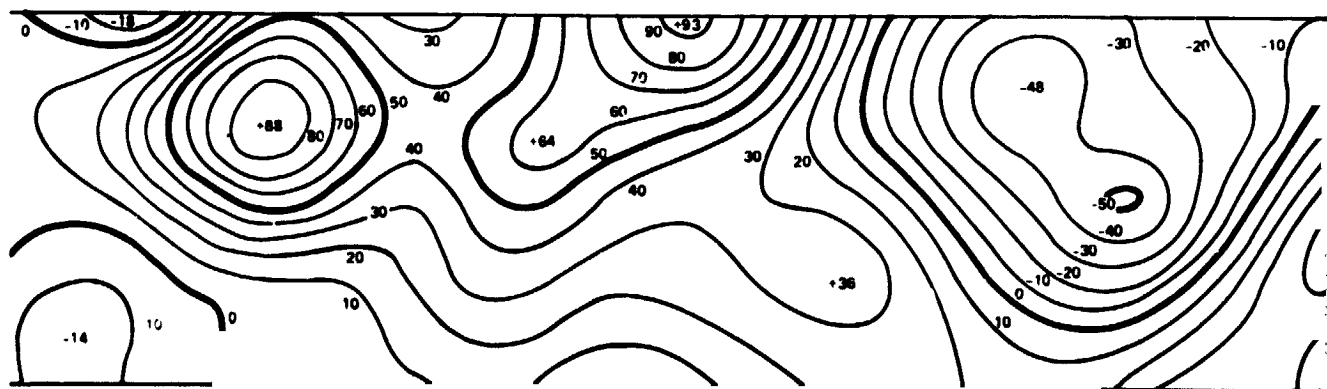


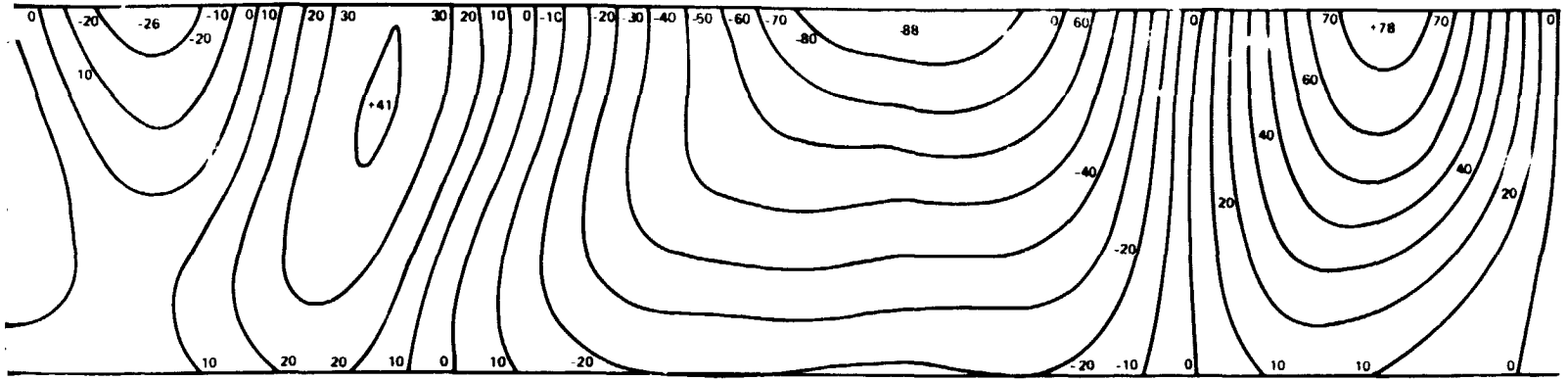
Fig. 2. Doppler velocity and velo

PRECEDING PAGE BLANK NOT FILMED

FOLDOUT FRAME /

30 km ALTITUDE

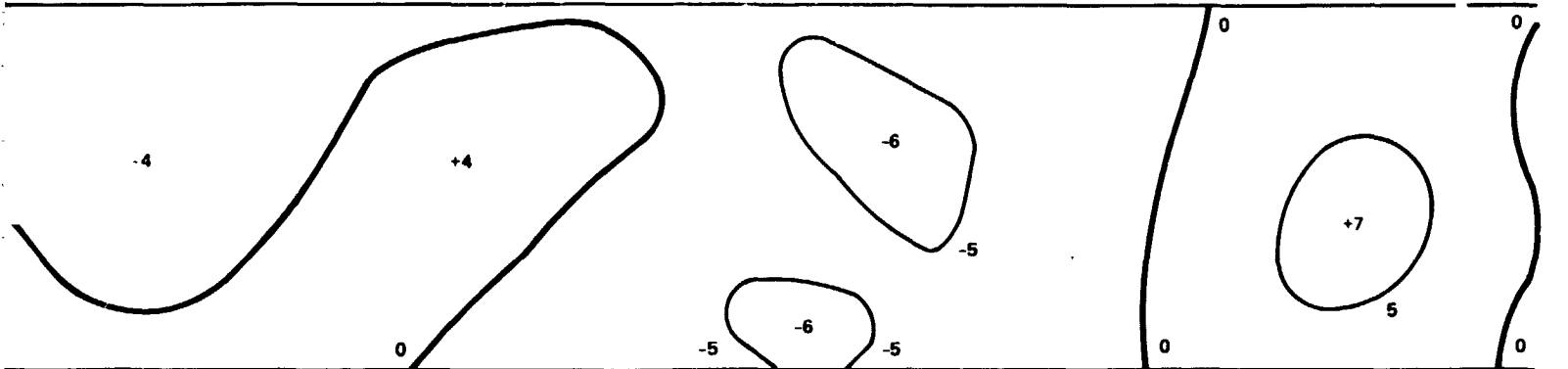
4652-11



km

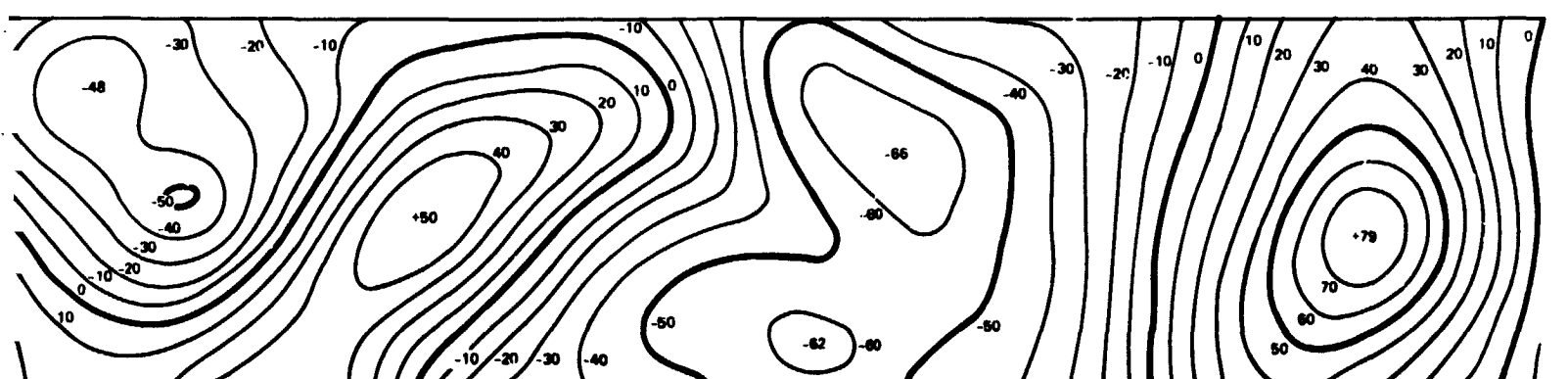
30 km ALTITUDE

4652-5



30 km ALTITUDE

4652-8



Doppler velocity and velocity change contour plots.

the resolution of the processed data. (See example in Fig. 5 of Sjogren, et al., [5] where a cubic spline fit was found inadequate to represent high resolution data.) We do not use this technique in generating our plots, as we wish to explore the high resolution aspects of both the gravity signal and the system noise.

In the plots in Fig. 2(b) and Fig. 3(a), (b), and (c), what is plotted is not the Doppler velocity, but the change in the Doppler velocity that would be induced in one resolution cell (15 km) by the gravity in that resolution cell. Since the time spent by the spacecraft in passing through that resolution cell is just

$$dt = \frac{15 \text{ km}}{1.7 \text{ km/sec}} = 8.8 \text{ sec} \quad (1)$$

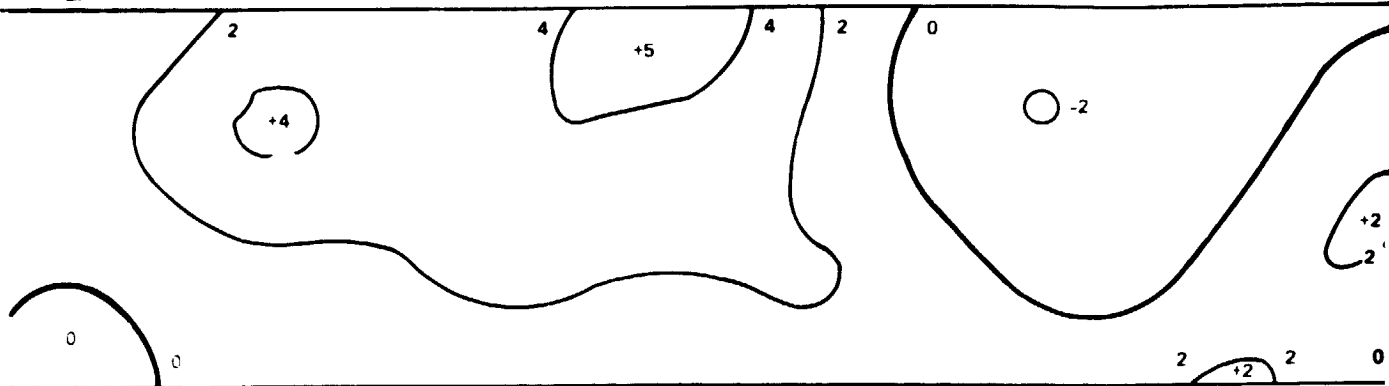
then the change in Doppler velocity is just

$$dv_z = g_z dt \quad (2)$$

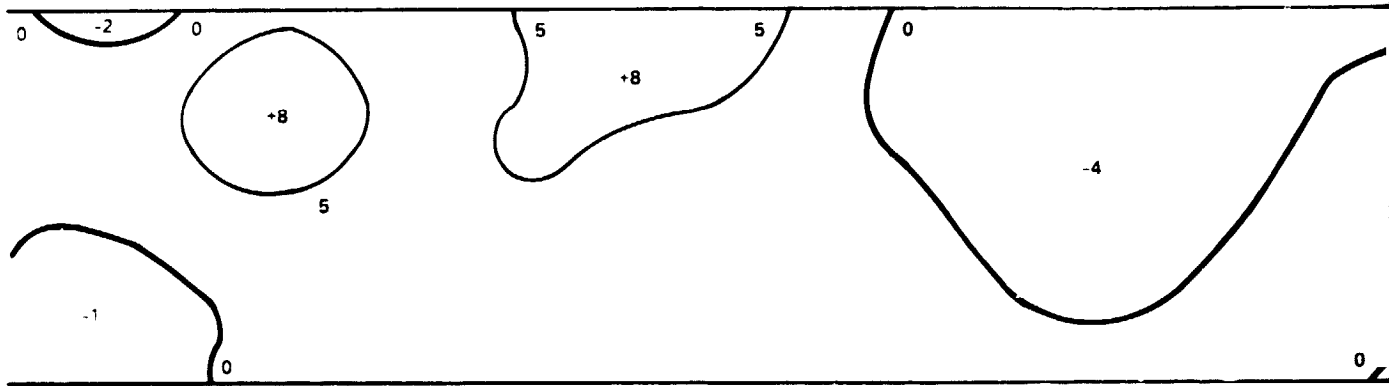
which comes out to be 0.88 mm/sec velocity change for 10 mgal of gravity acting for 8.8 sec. Thus these plots of vertical Doppler velocity difference for a constant resolution time of 8.8 sec are directly relatable to the vertical gravity field. The plots of the vertical Doppler velocity change are plotted in Fig. 3 for 15, 30, and 60 km altitude. At the bottom is the vertical gravity at 15 km for comparison. The 15 and 30 km plots are contoured at 5 mm/sec change per resolution time or 5 times the single point noise value and the 60 km plot is contoured at 2 mm/sec change per resolution time or twice the single point noise value. The 15 km plot could have been contoured at 0.88 mm/sec change per resolution time and would have looked identical to the vertical gravity plot. It was contoured at 5 mm/sec change per resolution time so that we may later compare it with the gravity gradiometer plots and other plots with contour values of comparable amplitude-to-measurement-noise ratios. One feature to notice on the Doppler velocity change plots is that the amplitude of the larger, low

Δv_z , VERTICAL DOPPLER VELOCITY CHANGE, mm/sec CHANGE IN 15 km

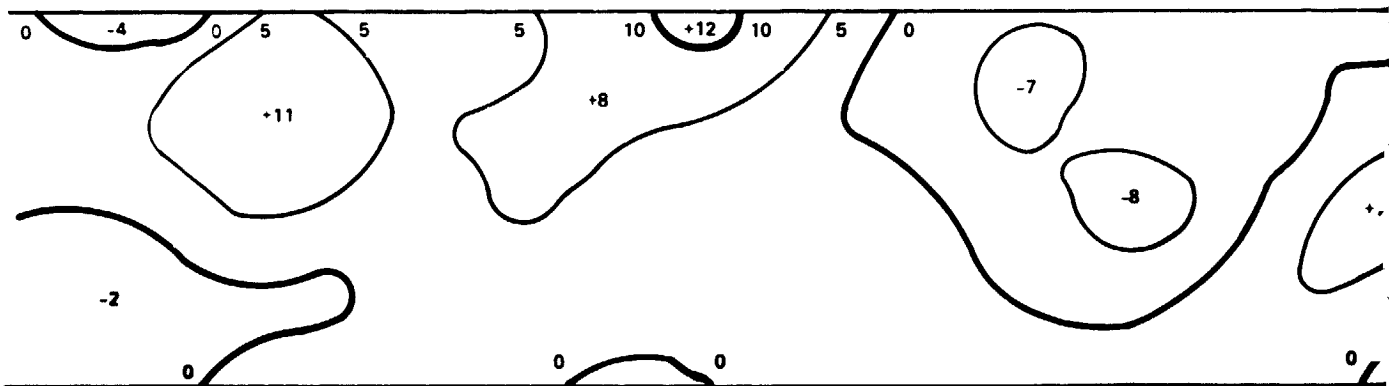
a
2 mm/sec CHANGE
CONTOURS



b
5 mm/sec CHANGE
CONTOURS

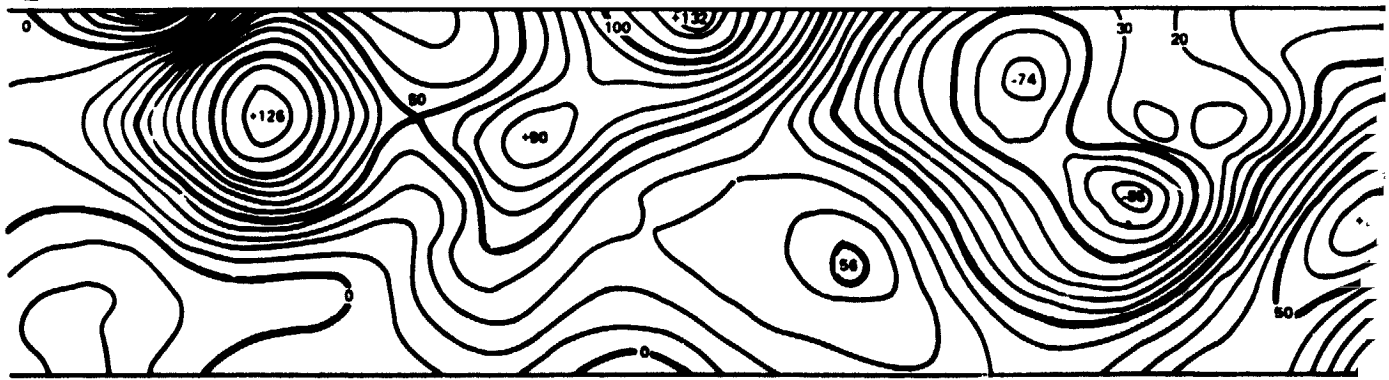


c
5 mm/sec CHANGE
CONTOURS



g_z , VERTICAL GRAVITY, mgals

10 mgal
CONTOURS



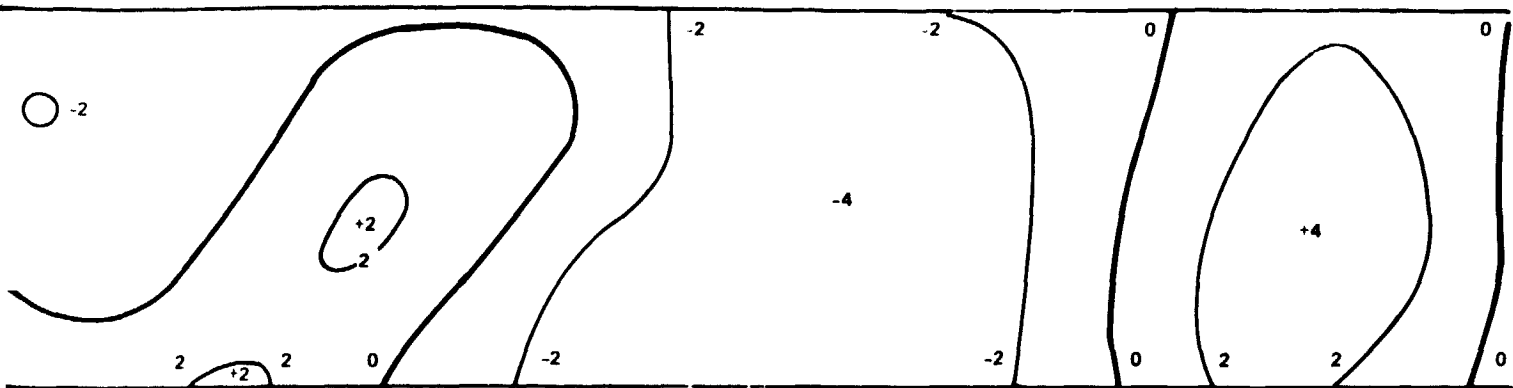
PRECEDING PAGE BLANK NOT FILMED

Fig. 3. Doppler velocity change in 15 km

FOLDOUT FRAME /

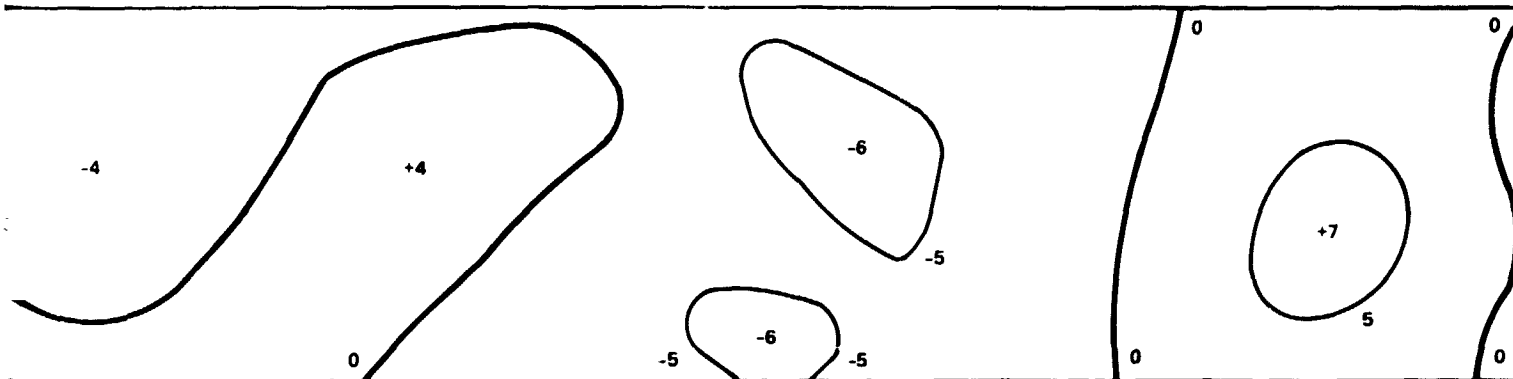
60 km ALTITUDE

4652-4



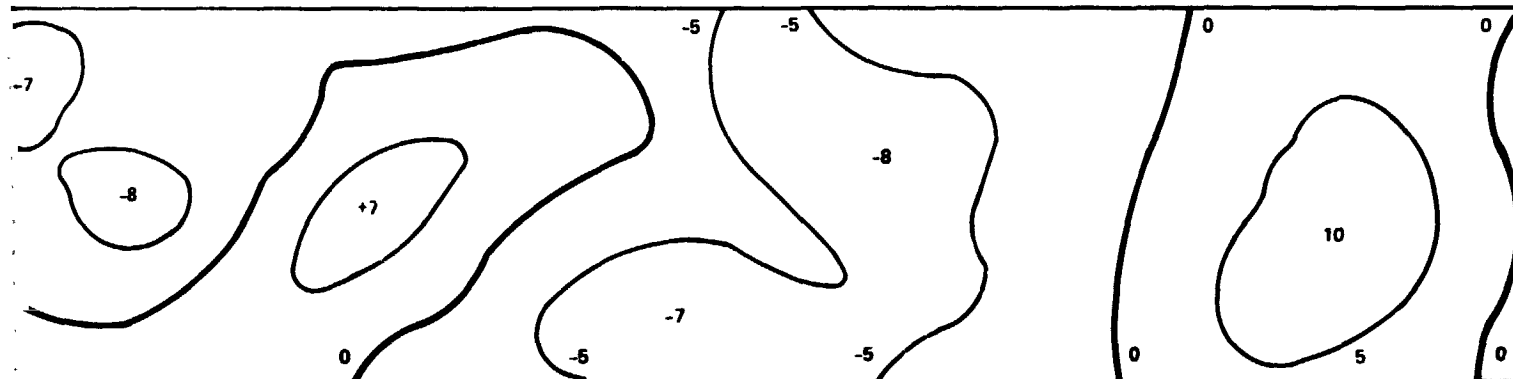
30 km ALTITUDE

4652-5



15 km ALTITUDE

4652-6



15 km ALTITUDE

4652-9



velocity change in 15 km sampling interval.

frequency, low resolution peaks such as the Lamont peak at +23 longitude and the peak at -18° longitude fall off relatively slowly with altitude. A factor of four in altitude between 15 km and 60 km only lowers the peak by a factor of 2.5.

VI. GRAVITY GRADIENT OF THE POINT MASS MODEL

To examine the performance of a gravity gradient measurement system on an LPO, we next calculated various components and combinations of components of the gradient of the gravity field. This was done by calculating at each measurement point the contribution to the total gravity gradient field from each of the 28 large mass points and the array of 81 smaller mass points in a 9 x 9 square array around the mass point below the measurement point. (This cutoff at ± 4 points on either side of the measurement point was found to give negligible error at both 15 and 60 km altitude.) Since the gravity gradient field is a tensor field, the equations for rotating the tensor field from the point mass coordinate frame to the calculation point measurement frame involves the double application of the rotation matrix. Once each contribution from each mass point has been rotated to the same calculation point reference frame, the amplitudes can be added. (For those interested, the derivation is in the appendix.)

The first set of gravity gradient calculations was the calculation of the vertical gradient of the vertical gravity

$$\Gamma_{zz} = \frac{dg_z}{dz} \quad (3)$$

which for a point mass M at distance R is

$$\Gamma_{zz} = \frac{2GM}{R^3} \quad (4)$$

Because this is a component of a tensor instead of a vector, the change of the amplitude of this component of the gravity gradient tensor with horizontal separation from the mass point

$$\Gamma_{zz}(x) = \frac{2GM}{(z^2+x^2)^{3/2}} \left(1 - \frac{3}{2} \frac{x^2}{(z^2+x^2)} \right) \quad (5)$$

is different than the variation in the amplitude of the vertical component of the gravity vector with change in horizontal separation

$$g_z(x) = \frac{GM}{(z^2+x^2)} \left(\frac{z}{(z^2+x^2)^{1/2}} \right) \cdot \quad (6)$$

This is shown graphically in Fig. 4. Note that the vertical gradient of vertical gravity (Γ_{zz}) peaks to a maximum over the mass point, just as the vertical gravity (g_z) does (see Fig. 4), but drops off more rapidly with horizontal separation distance and becomes slightly negative at large separations. Despite this difference, we see there is a great deal of similarity in the general shape of the two curves, and one would expect that a contour map of the vertical gradient of vertical gravity would look very similar to a contour map of the vertical gravity. However, we might expect to see higher resolution data in the gradient map because the more rapid fall-off of the point function of the gradient.

In Fig. 5 we present contour maps of the vertical gradient of the vertical gravity calculated from the point mass model for 15, 30, and 60 km altitude. The vertical gravity contour map at 15 km is placed at the bottom for comparison. The units of the gradient plots are in Eotvos.* The present state of the art in gravity gradient instrumentation is a noise level of ± 1 Eotvos for a 10 sec integration time. (All three instrument concepts under development have demonstrated performance at close to these levels in their laboratory physical feasibility models and all three engineering models presently being assembled have this noise level as their goal.) Since the time for a spacecraft to pass over a 15 km resolution cell is 8.8 sec, the data point in each resolution cell can be expected to have an accuracy comparable to this. Until more

* (1 Eotvos = 10^{-9} gal/cm = 10^{-9} sec⁻² = 0.1 mgal/km = 10^{-10} g's/m.)

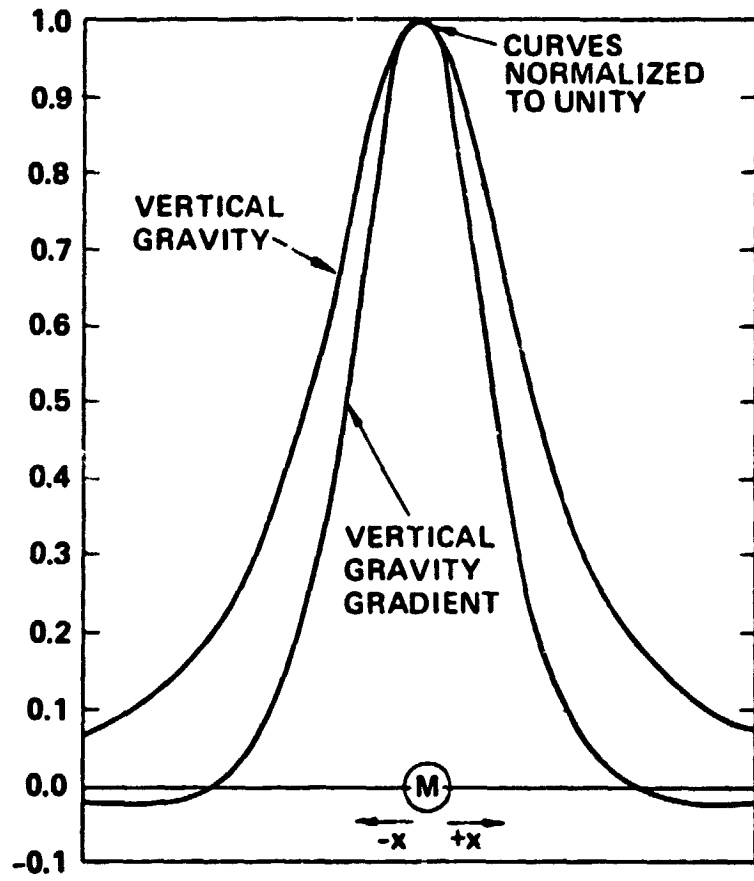
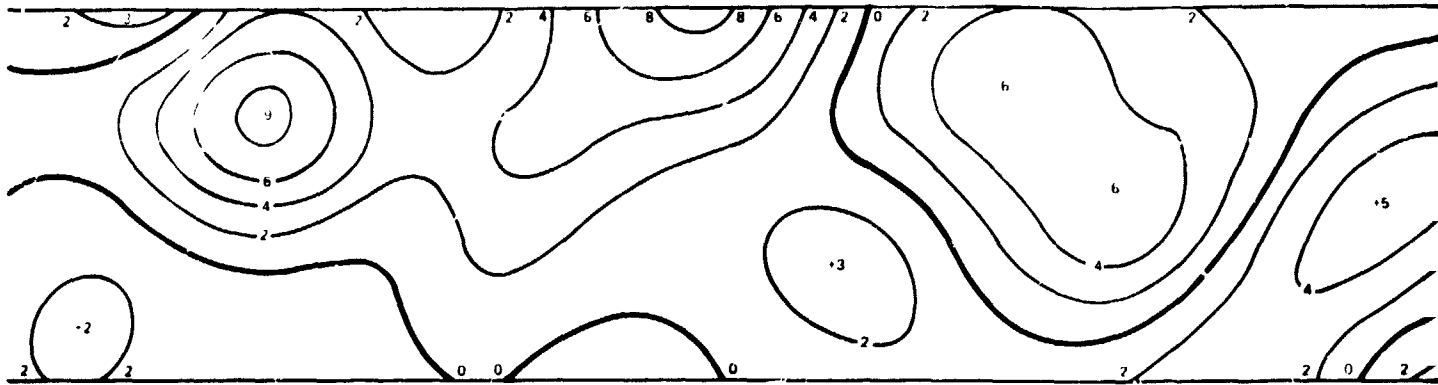


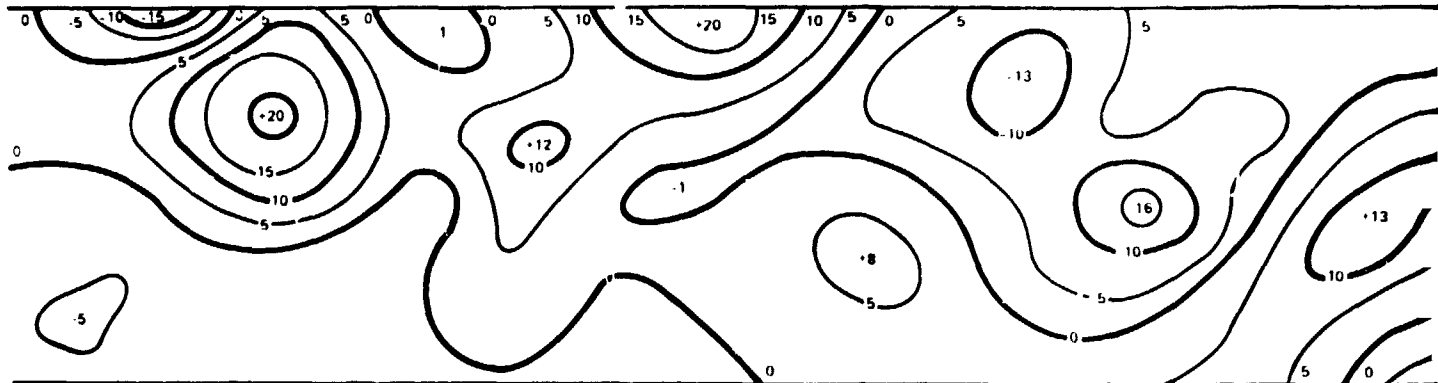
Fig. 4. Strength of vertical component of field as a function of horizontal separation.

Γ_{ZZ} VERTICAL GRADIENT OF VERTICAL GRAVITY, EOTVOS

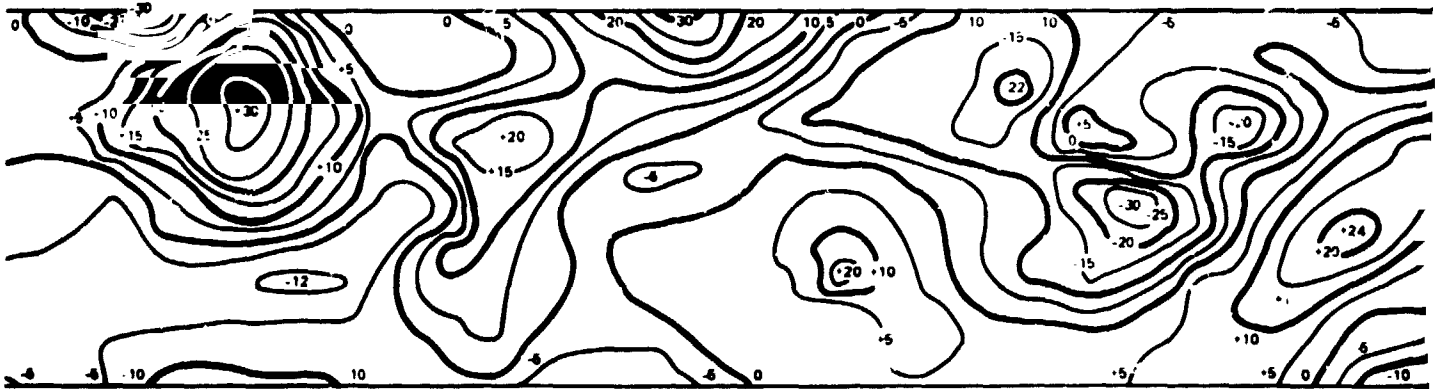
2 EOTVOS
CONTOURS



5 EOTVOS
CONTOURS



5 EOTVOS
CONTOURS



g_z VERTICAL GRAVITY, mgals

10 mgals
CONTOURS

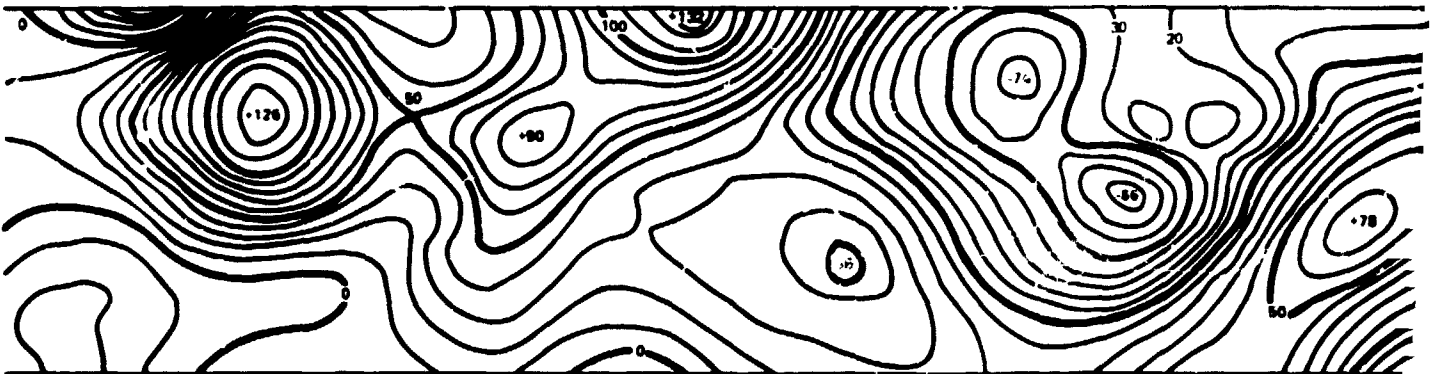
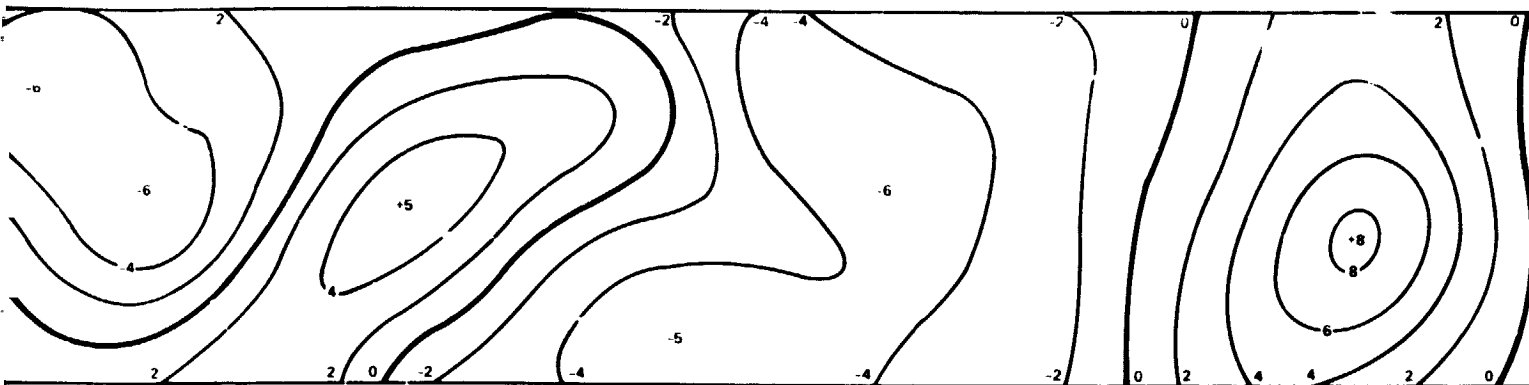


Fig. 5. Vertical gradient of vertical grav'

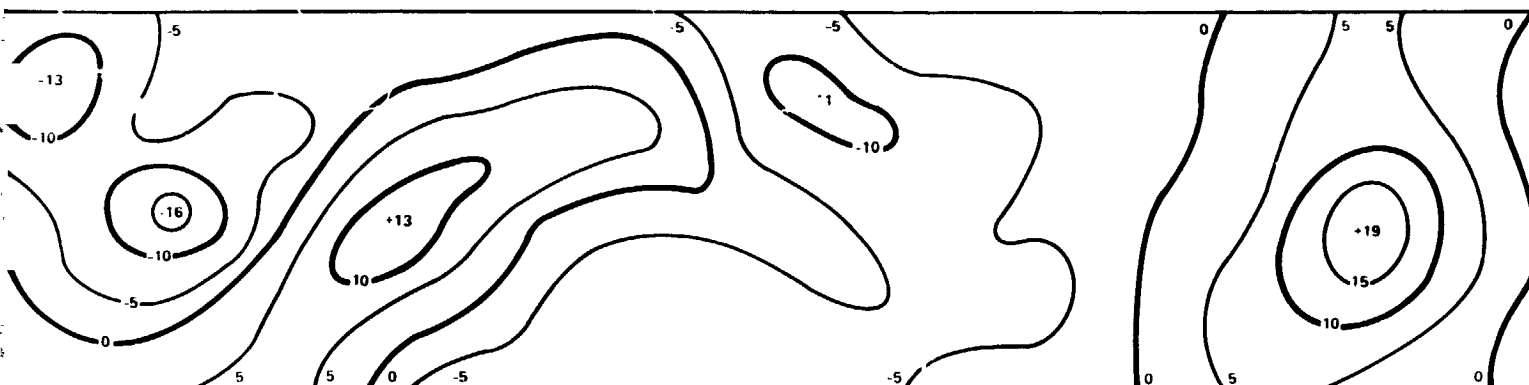
60 km ALTITUDE

4652-3



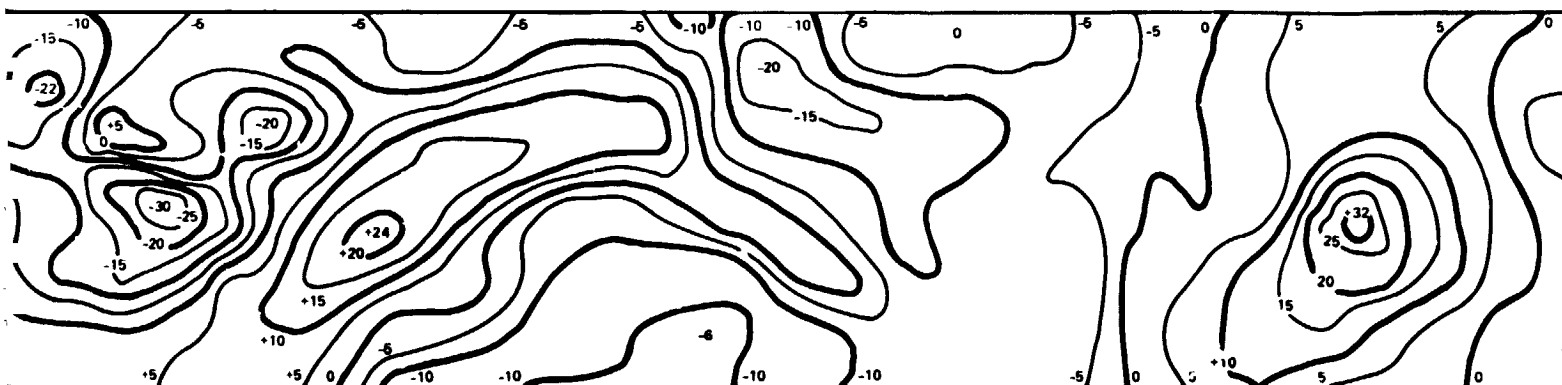
30 km ALTITUDE

4652-2



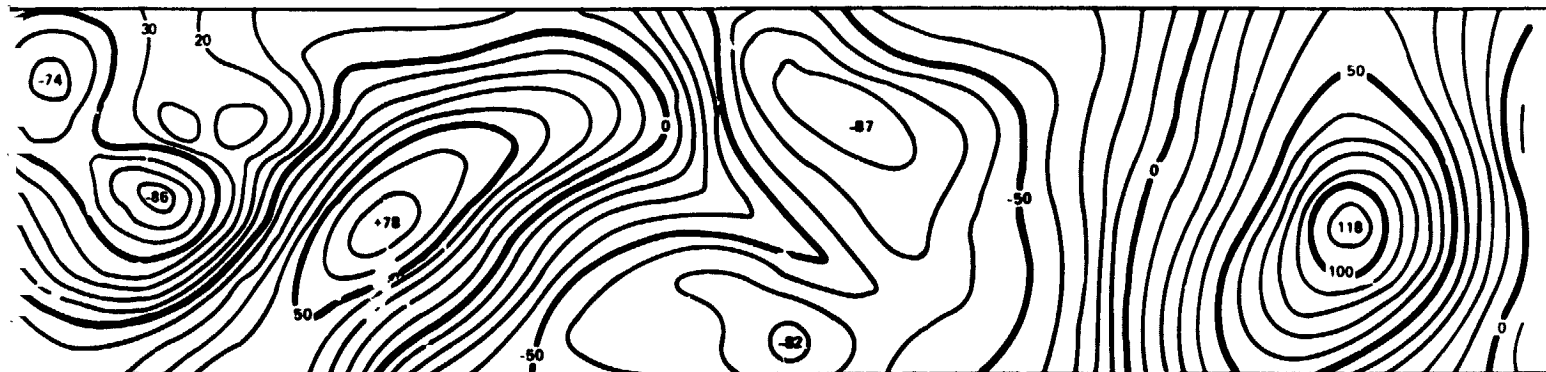
15 km ALTITUDE

4652-1



15 km ALTITUDE

4652-9



al gradient of vertical gravity contour plots.

A-39

FOLDOUT FRAME 2

definitive information of the exact performance of an LPO gravity gradiometer system is available, we will assume a system noise level of ± 1 Eotvos per 15 km resolution cell in our calculations.

The contours on the gravity gradient maps are 5 Eotvos for the 15 and 30 km plots (five times the single point noise level) and 2 Eotvos for the 60 km contours, (twice the single point noise level), thus the contour interval-to-single point noise level (a rough S/N ratio) is the same for these contour maps as for the Doppler velocity change contour maps in Fig. 2

There are two features to look for; one is that the higher resolution features are more readily resolved with the gravity gradient plots, this is especially evident in the features near -2° longitude. The other is that the larger, lower frequency, lower resolution features fall off more rapidly with altitude. For the Lamont peak at $+23^\circ$ longitude and the peak at -18° longitude, the factor of 4 in altitude from 15 km to 60 km causes a decrease in amplitude of a factor of 4, whereas in the Doppler velocity plots the decrease was only a factor of 2.5. Nevertheless, despite the more rapid decrease, the signal-to-noise of those peaks at 60 km altitude in the gravity gradient plots (8 Eotvos) is twice as good as the signal to noise of the same peaks in the Doppler velocity difference plots (4 mm/sec change per resolution time).

One of the more startling features of the gravity gradient plots is that the plot of the vertical gradient of vertical gravity at 15 km altitude almost seems to show more structure than is evident to the eye when looking at the original set of vertical gravity data. This may raise some questions as to the validity or reality of the high resolution features in the 15 km gravity gradient data.

First, we are fairly sure that the simple computational algorithms used are correct because of our previous tests of internal self-consistency. Second, although our contouring routine leaves something to be desired, the contours presented were rounded off by eye and therefore are smoother (have less detail) than the data set would have them. Third, although we used a real set of gravity data as a starting point, our whole simulation and the comparisons between the two gravity measurements

systems are based on their performance in measuring the gravity field of the point mass model. Since the gravity gradient plots show more detailed structure of the point mass model than the Doppler velocity plots, we would expect to see the same advantage when they are measuring the distributed mass variations of the moon.

Fourth, we generated a second point mass model consisting of the original 28 large masses, plus an array of smaller mass points, again spaced at 15 km intervals, but now placed 15 km below the lunar surface rather than on the surface. The convergence was not as good this time, and the milligal variations between the point mass model vertical gravity and the original lunar vertical gravity ranged as high as 8 mgals with an rms variations of 1.1 mgals. The plot of vertical gradient of vertical gravity from this point mass model at 15 km altitude (30 km from the mass points) has nearly all the high resolution features of the plot from the surface point mass model, and only differs significantly at the large peaks (where the convergence was poorest). This indicates that the detail seen in the gradient plots is in the gravity plots (although difficult to see with the eye) and is not an artifact caused by the closeness of the point mass model.

Now, the vertical gradient of the vertical gravity was chosen for the previous plots because the contour plots of this quantity are similar in shape to the vertical gravity contour plots and they can be easily compared by eye. Of the various possible instrument mechanizations for the gravity gradient experiment, most do not give the vertical gradient of vertical gravity directly, but instead give combinations of the components of the gravity gradient tensor. If two or three orthogonal instruments are used (two for certain types of instruments under certain conditions) then all the gravity gradient components (including Γ_{zz}) can be calculated from the instrument outputs. However, as we shall show, even one instrument, with its slightly ambiguous combination output, can give highly useful information. One type of gravity gradiometer instrument produces two outputs

$$\frac{1}{2}(\Gamma_{zz} - \Gamma_{yy}) \quad \text{and} \quad \Gamma_{zy} \quad (7)$$

if oriented in the vertical-east plane or

$$\frac{1}{2}(\Gamma_{zz} - \Gamma_{xx}) \quad \text{and} \quad \Gamma_{zx} \quad (8)$$

if oriented in the vertical-north plane (the orbital plane of a polar orbit). Now, the vertical gradient of the vertical gravity (Γ_{zz}) and the horizontal gradient of the horizontal gravity (Γ_{xx} or Γ_{yy}) are closely related to each other for most types of mass distributions. For a point mass, the relationship is simple and direct

$$\Gamma_{zz} = -2\Gamma_{xx} = -2\Gamma_{yy} = \frac{2GM}{R^3}$$

whereas for more complex features the relationships are only approximate. (The relationship is worst for linear features where the horizontal gradient along the feature is zero.) Thus a contour plot of just the instrument output

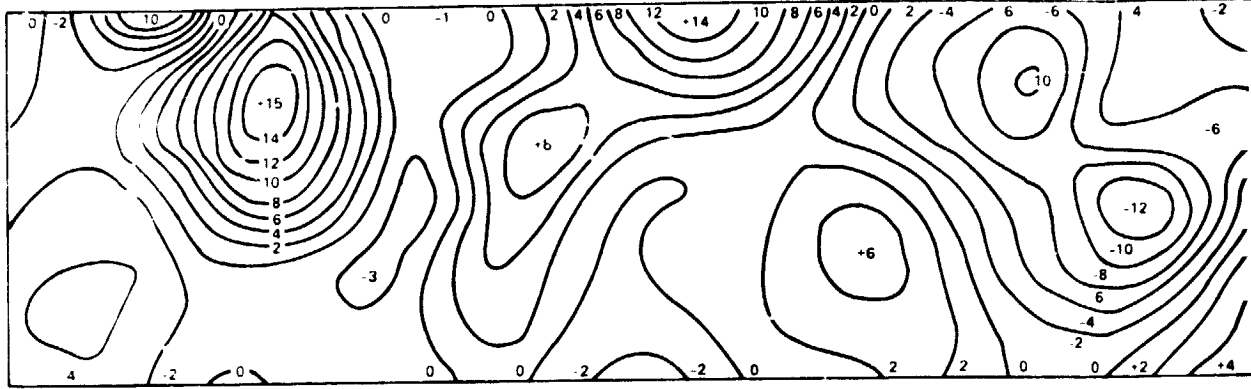
$$\frac{1}{2}(\Gamma_{zz} - \Gamma_{xx}) \approx \frac{3}{4} \Gamma_{zz} \quad (10)$$

can be expected to have nearly all of the features of a contour plot of vertical gradient of vertical gravity with some slight distortion. This can be seen in the plots in Fig. 6. These are all at 30 km altitude and have been contoured at 2 Eotvos (twice single-point-noise-level) to bring out the detail. As can be seen by inspection and comparison with the vertical gravity plot at 30 km, a simple contour plot of the instrument output can provide high resolution information that can be used for geophysical interpretation.

Now the plots of gradiometer instrument output are in units and parameters and mixtures of components that geophysicists are not used to working with. There are two approaches to alleviating the problem. One is to develop algorithms that will remove the ellipsoidal distortion to obtain the vertical gradient and others to obtain the vertical gravity.

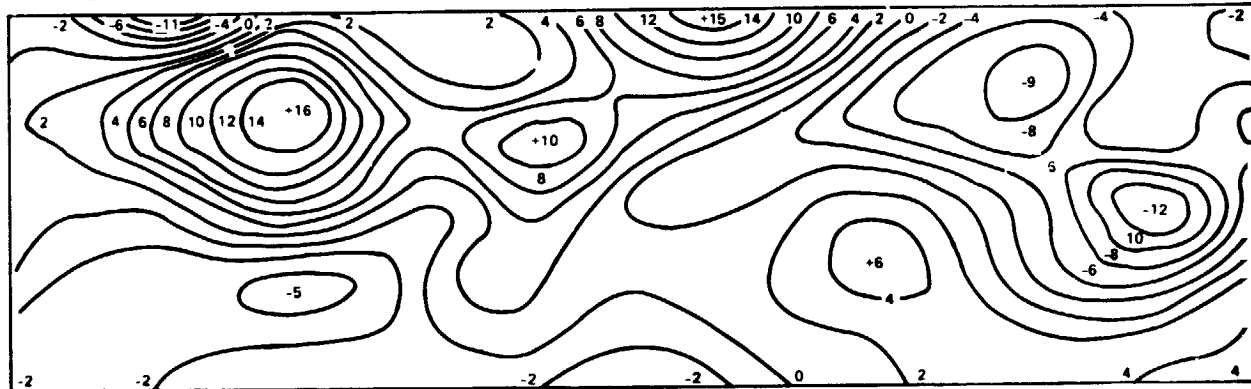
$1/2 (\Gamma_{ZZ} - \Gamma_{XX})$, ONE CHANNEL OF INSTRUMENT OUTPUT, EOTVOS

30



$1/2 (\Gamma_{ZZ} - \Gamma_{YY})$, ONE CHANNEL OF INSTRUMENT OUTPUT, EOTVOS

30



g_Z , VERTICAL GRAVITY, mgal

30

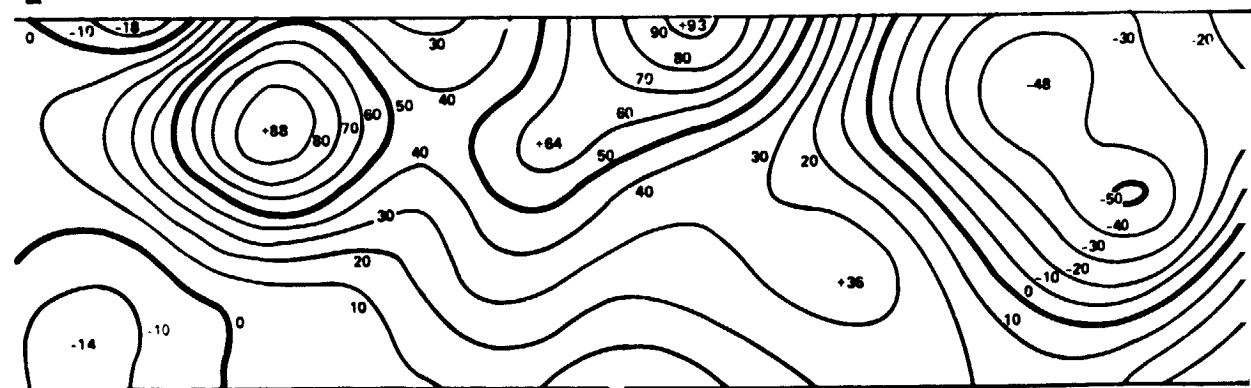


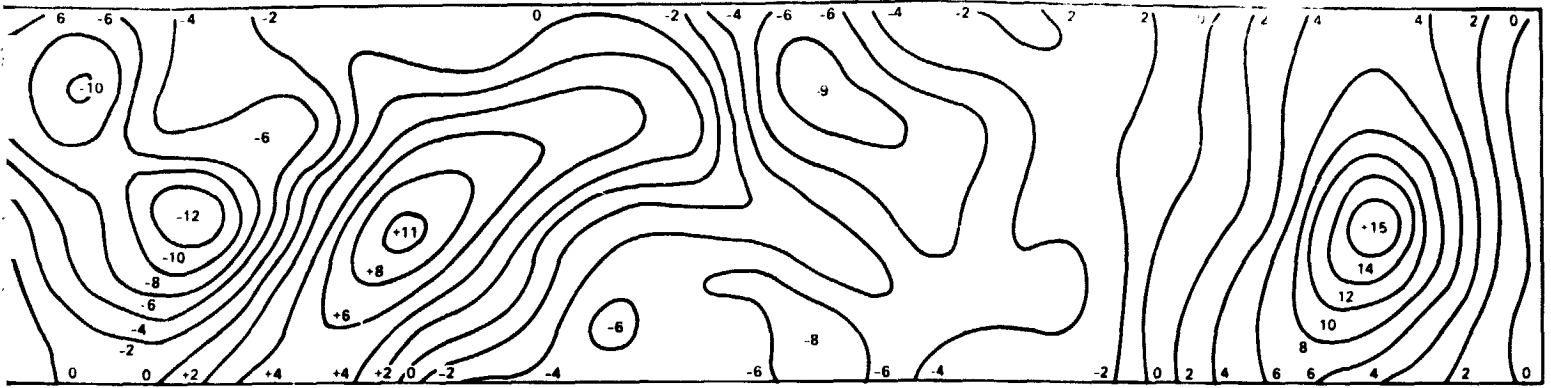
Fig. 6. Gravity gradiometer

PRECEDING PAGE BLANK NOT FILMED

FOLDOUT FRAME

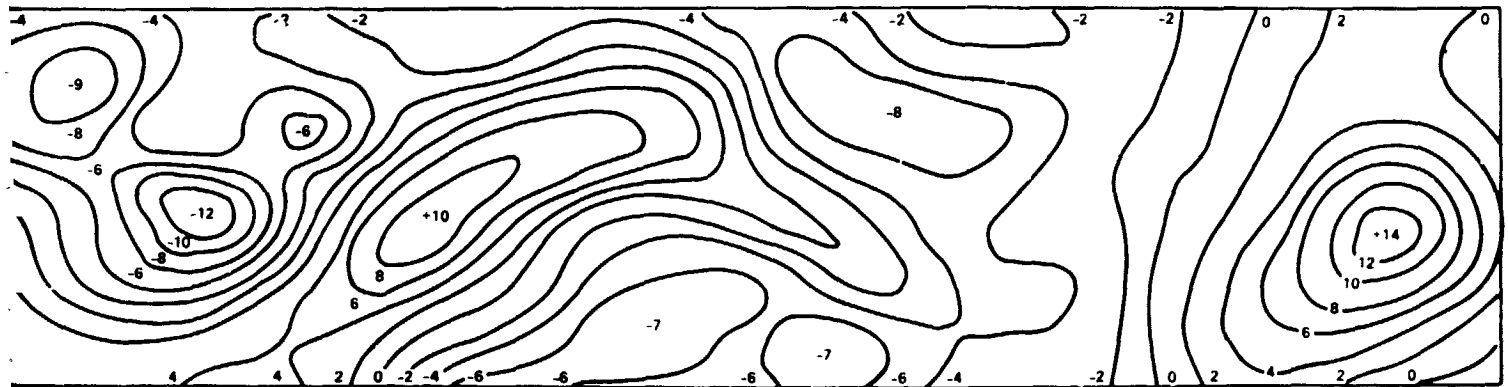
30 km ALTITUDE

4652-12



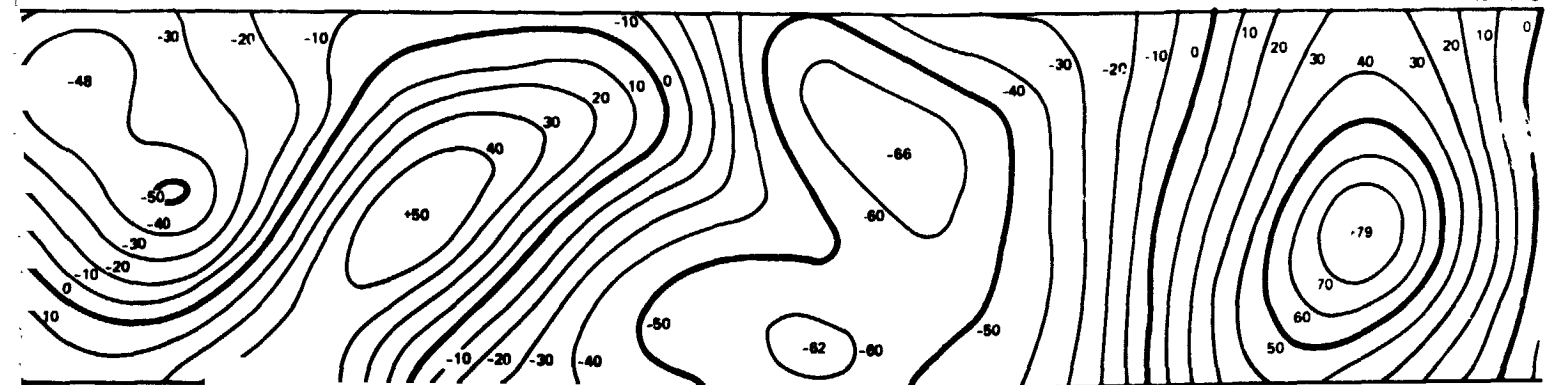
30 km ALTITUDE

4652-13



30 km ALTITUDE

4652-8



ity gradiometer instrument output contour plots.

A-45

FOLDOUT FRAME 2

However, with a little retraining, geophysicists may find that these plots are just as easy to work with as vertical gravity plots and more valuable because of their high resolution content.

At the present time, when a geophysicist looks at a contour gravity map, he compares the features with a topographical map, and then using experience and reasonable assumptions, constructs a mass model of layers, scarps, discs, rings and other geometrical features. He then uses a computer to calculate the gravity from these features and compares it with the real data set, and readjusts the model until he gets a good fit. The procedure with gravity gradient data could be the same, except that the computer program is changed to calculate the gradient components (or combinations of components) instead of the gravity component. The resultant mass distribution should be the same for either procedure.

VII. GRAVITY PLOTS FROM GRADIENT PLOTS^[6]

If the gravity anomalies are desired in the form of gravity contour plots, then it is possible to obtain these in a simple manner from the gravity gradients by integration of the gradient components.

The time variation of the components of the lunar gravity vector ($\dot{\vec{g}}$) are given by the product of gravity gradient tensor ($\bar{\bar{\Gamma}}$) and the vehicle velocity vector (\vec{v})

$$\dot{\vec{g}} = \bar{\bar{\Gamma}} \cdot \vec{v} \quad (11)$$

Equation (11) can be written component by component in a north, west, up (x, y, z) coordinate frame;

$$\dot{g}_x = \frac{\partial g_x}{\partial x} v_x + \frac{\partial g_x}{\partial y} v_y + \frac{\partial g_x}{\partial z} v_z \quad (\text{north component})$$

$$\dot{g}_y = \frac{\partial g_y}{\partial x} v_x + \frac{\partial g_y}{\partial y} v_y + \frac{\partial g_y}{\partial z} v_z \quad (\text{west component})$$

$$\dot{g}_z = \frac{\partial g_z}{\partial x} v_x + \frac{\partial g_z}{\partial y} v_y + \frac{\partial g_z}{\partial z} v_z \quad (\text{vertical component}) \quad (12)$$

where v_x , v_y , and v_z are components of the velocity, \vec{v} . Because the gravity gradient tensor is symmetrical and the Laplacian of the gravity potential is zero the following relations apply:

$$\frac{\partial g_x}{\partial y} = \frac{\partial g_y}{\partial x} \quad , \quad \frac{\partial g_x}{\partial z} = \frac{\partial g_z}{\partial x} \quad , \quad \frac{\partial g_y}{\partial z} = \frac{\partial g_z}{\partial y} \quad (13)$$

$$\frac{\partial g_x}{\partial x} + \frac{\partial g_y}{\partial y} + \frac{\partial g_z}{\partial z} = 0 \quad (14)$$

Note that the gravity vector can be computed from eqs. (12) by integration with time if the gravity gradients and vehicle velocity are known. Note also that if vehicle velocity is constrained so that certain components are zero (e.g., $v_y = 0$, $v_z = 0$), then it is unnecessary to measure all gravity gradients, because some terms drop out of these equations.

For the case of the LPO spacecraft in a polar orbit, the major component of the spacecraft velocity vector is in the north (x) direction, while the west (y) and up (z) components of the velocity vector are much smaller. For illustration, let us assume that:

$$\begin{aligned} v_x &= 1.7 \text{ km/sec} \\ v_y &= 0 \\ v_z &= 0 \end{aligned} \quad (15)$$

then the eq. (12) reduce to:

$$\begin{aligned} \dot{g}_x &= \frac{\partial g_x}{\partial x} v_x \\ \dot{g}_y &= \frac{\partial g_y}{\partial x} v_x \\ \dot{g}_z &= \frac{\partial g_z}{\partial x} v_x \end{aligned} \quad (16)$$

Thus by utilizing the fact that the velocity of the vehicle is uniform, we can see that from eqs. (16) that it is only necessary to measure three of the five components of the gravity gradient tensor to obtain all three components of the gravity field vector. If the spacecraft has two rotating gravity gradiometers, one oriented with its spin axis vertical to measure the gradient components in the (x, y) plane tangent to the surface of the moon, and the other with its spin axis along the orbit axis to measure the gravity gradients in the (x, z) plane of the orbit, then the sine and cosine outputs of the sensors will contain the following gravity gradient components:

$$\begin{aligned}
 S_{xy} &= \frac{\partial g_x}{\partial x} - \frac{\partial g_y}{\partial y} & , & & C_{xy} &= 2 \frac{\partial g_y}{\partial x} \\
 S_{zx} &= \frac{\partial g_z}{\partial z} - \frac{\partial g_x}{\partial x} & , & & C_{zx} &= 2 \frac{\partial g_z}{\partial x} .
 \end{aligned} \tag{17}$$

The two cosine outputs of the sensors are seen to give two of the desired gravity gradient components directly. The remaining gravity gradient term can be obtained by combining the two sine outputs and using the fact that the Laplacian of the gravity potential must be zero (eq. 14)

$$S_{xy} - S_{zx} = 3 \frac{\partial g_x}{\partial x} - \left(\frac{\partial g_x}{\partial x} + \frac{\partial g_y}{\partial y} + \frac{\partial g_z}{\partial z} \right) = 3 \frac{\partial g_x}{\partial x} . \tag{18}$$

Thus, by utilizing the fact that the LPO velocity vector is nearly entirely in the lunar north direction, we can obtain a good estimate of all the components of the lunar gravity field vector with the output data from only two rotating gravity gradiometers:

$$\begin{aligned}
\dot{g}_x &= \frac{1}{3} (S_{xy} - S_{zx}) v_x + \text{errors } O(v_y/v_x, v_z/v_x) \\
\dot{g}_y &= \frac{1}{2} C_{xy} v_x + \text{errors } O(v_y/v_x, v_z/v_x) \\
\dot{g}_z &= \frac{1}{2} C_{zx} v_x + \text{errors } O(v_y/v_x, v_z/v_x) \quad . \quad (19)
\end{aligned}$$

Alternatively, we can obtain a vertical gravity contour map from just one of the outputs (Γ_{zx}) of one gradiometer by integration:

$$\begin{aligned}
g_z &= \int \dot{g}_z dt = \int \frac{dg_z}{dx} \cdot v_x dt \\
&= \int \frac{dg_z}{dx} dx \quad . \quad (20)
\end{aligned}$$

If the orbit were truly polar, then the integration would start as the LPO passed over the pole. A nominal value for the gravity at the pole would be assumed as the constant of integration, and then the gradient variations from that point would be used to calculate the gravity variations from the nominal value. In practice, the orbit will not be truly polar and a fit would have to be made to the circle of closest approach to the pole to obtain starting values for each orbit.

In Fig. 7(a) we have presented a contour plot of the north variation of the vertical gravity (Γ_{zx}) as calculated from the point mass model at an altitude of 15 km. Since Γ_{zx} goes to zero over a point mass, the contours seem to have no relation to the vertical gravity. However, if we assume that integration has been taking place in the data along the orbit from the pole, then we will know the gravity field along the top edge of the region that we are plotting. If we take this

single line of vertical gravity data and then add or subtract an amount given by

$$dg_z = \Gamma_{zx} dx \quad (21)$$

(where dx is 15 km), then for every change of 1 Eotvos in 15 km we get a change in the vertical gravity of 1.5 mgals. This integrated set of data was contoured and plotted below the gradient plot (Fig. 7(b)) and is seen to be very close to the vertical gravity at 15 km calculated directly from the point mass model (Fig. 7(c)). Since the noise on the gradient data is ± 1 Eotvos, the noise of the gravity contours is ± 1.5 mgals.

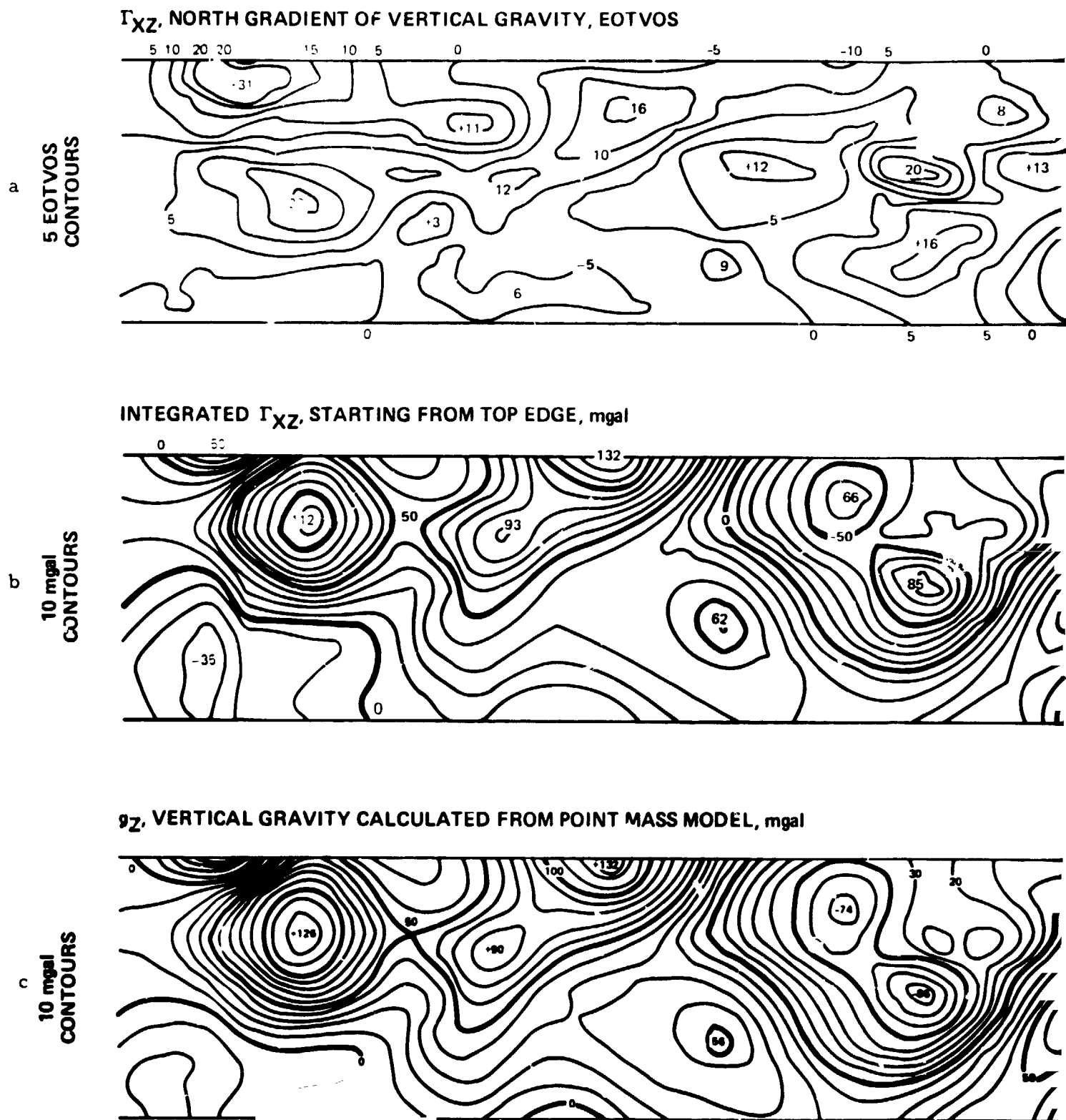
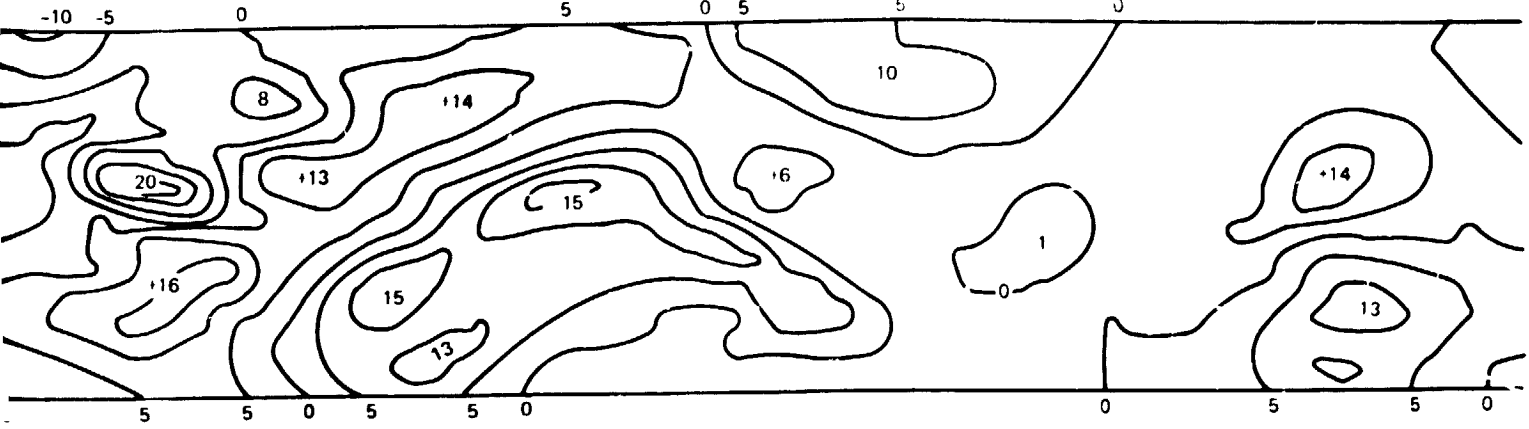


Fig. 7. Vertical gravity integrated from

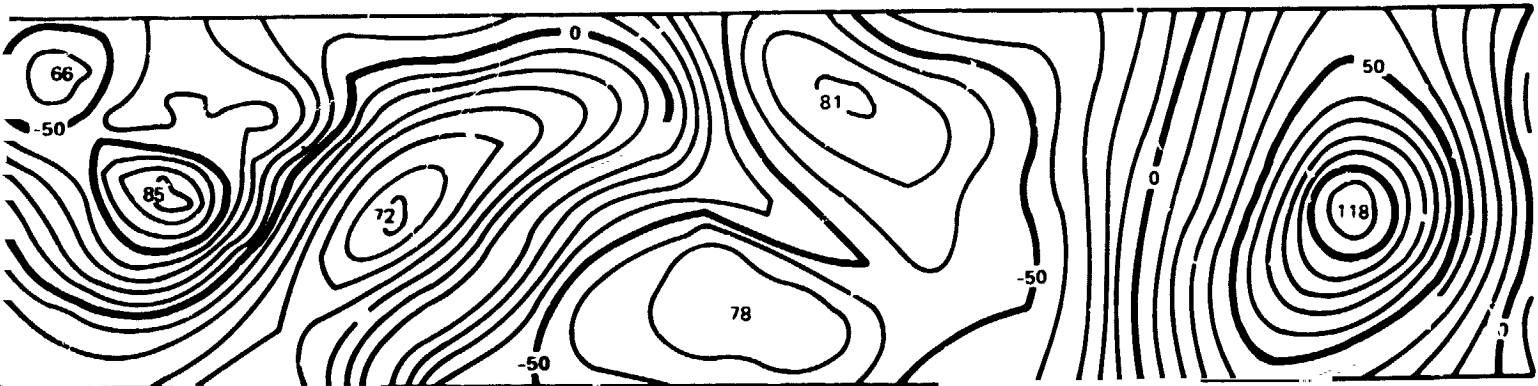
15 km ALTITUDE

4652-14



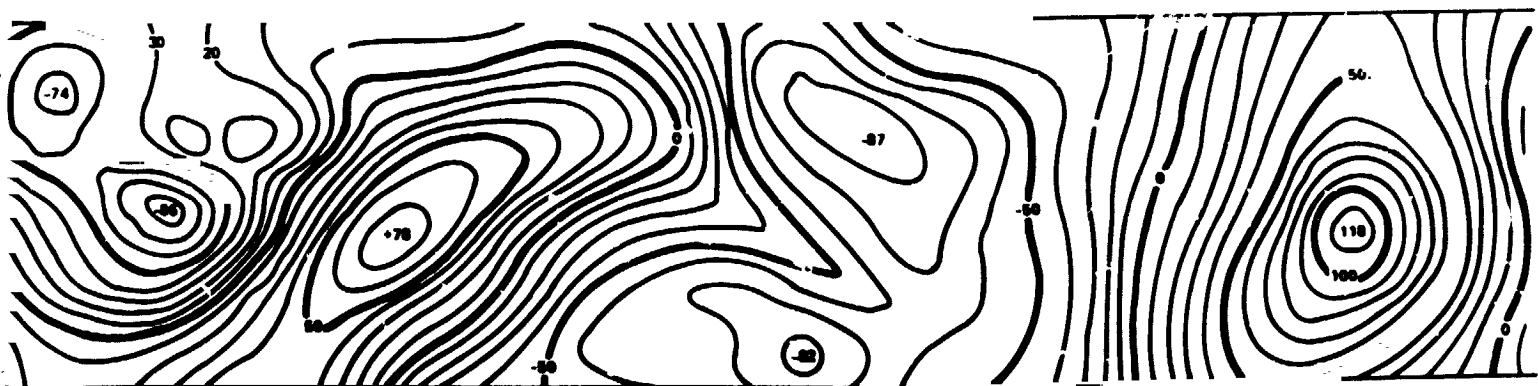
15 km ALTITUDE

4652-15



15 km ALTITUDE

4652-9



gravity integrated from horizontal gradients.

VIII. EFFECTS OF SYSTEM NOISE ON CONTOURS

It is difficult to give a direct and simple relationship that will describe how the noise of the measurement system affects the contours used in a plot. The measurement noise is a random variation of a single point measurement. In our simulations here, we assume a measurement every 15 km in both the x and y directions. The LPO spacecraft will be in a near polar orbit with a velocity in the north-to-south or south-to-north direction of about 1.7 km/sec, thus we are assuming a measurement every 8.8 sec. Naturally the measurements along the track, being sequential in time and at nearly the same altitude, will have more correlation than those across the track, which will come on different orbits.

To get a feeling for the effects of measurement noise on the contours, we ignored the correlation effects and assumed that each measurement point was an independent measurement. We then added gaussian random noise onto each calculated point for both the Doppler and gradient at 30 km altitude. The resultant noisy data caused havoc with our contour plotting routine, so it was necessary to apply some adjacent point smoothing to take out isolated noise peaks. This smoothing effectively reduced our rms noise level from ± 1 Eotvos and ± 1 mm/sec to ± 0.6 Eotvos and ± 0.6 mm/sec. (This was of course accompanied by a degrading of the resolution from 15 km to about 30 km, but there was probably not much 15 km resolution data left at 30 km altitude anyway.) These smoothed data were then contoured and plotted. This was repeated four times with four different sets of additive random noise and the contours plotted on top of each other to give an estimate of the "noise width" of the contours (see Fig. 8). From inspection, it is seen that most of the Doppler velocity contours have "noise widths" greater than 15 km, in some areas reaching 45 km, while most of the gradient contours have "noise widths" significantly less than 15 km. It should be emphasized that if we make only one LPO gravity survey at 30 km altitude, we will get only one "best" contour from that one set of noisy data, and that "best" contour would lie anywhere within the "noise width" of the contours described by the four superimposed contours of the plots.

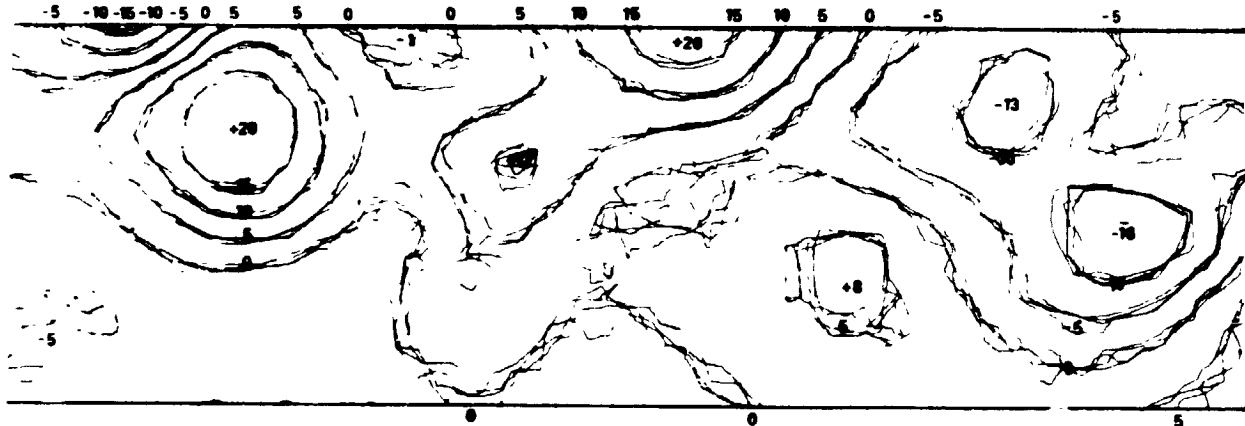
Δv_z , VERTICAL DOPPLER VELOCITY CHANGE, mm/sec CHANGE IN 15 km,
4 SUPERIMPOSED ADDITIVE NOISE PLOTS

5 mm/sec CHANGE
CONTOURS



Γ_{zz} , VERTICAL GRADIENT OF VERTICAL GRAVITY, EOTVOS,
4 SUPERIMPOSED ADDITIVE NOISE PLOTS

5 EOTVOS
CONTOURS



g_z , VERTICAL GRAVITY, mgal

10 mgal
CONTOURS

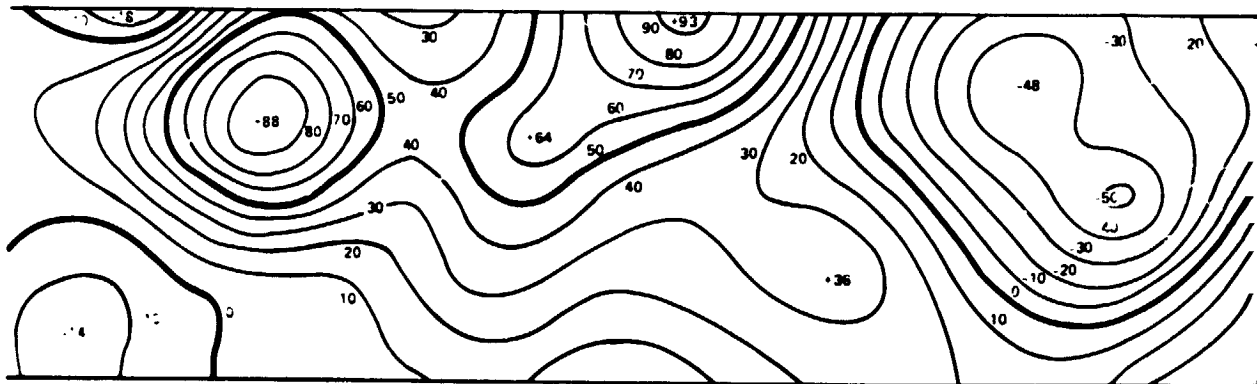


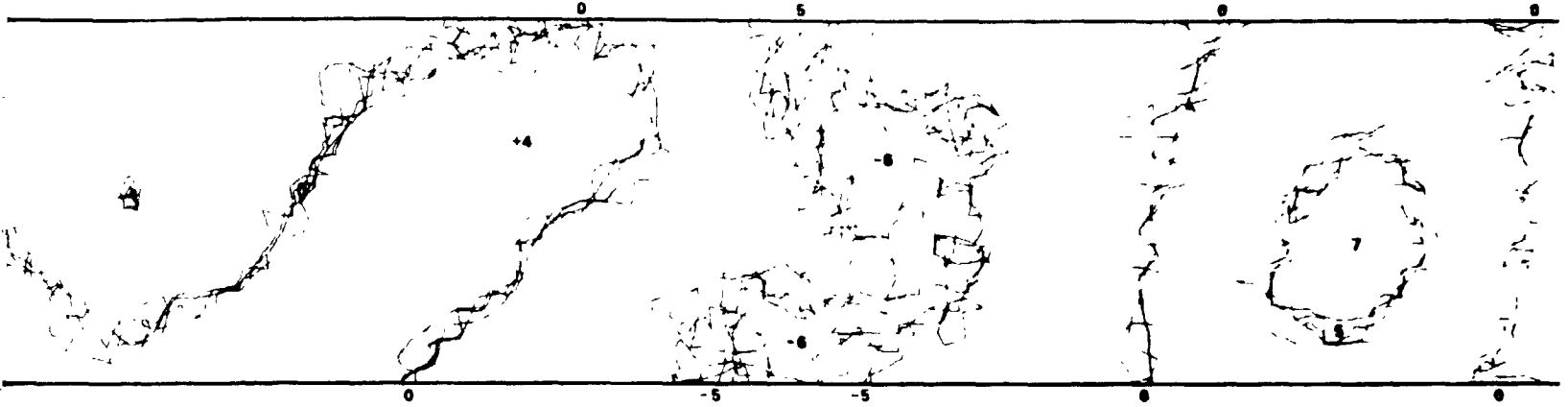
Fig. 8. Effect of noise

PRECEDING PAGE BLANK NOT FILMED

FOLDOUT FRAME /

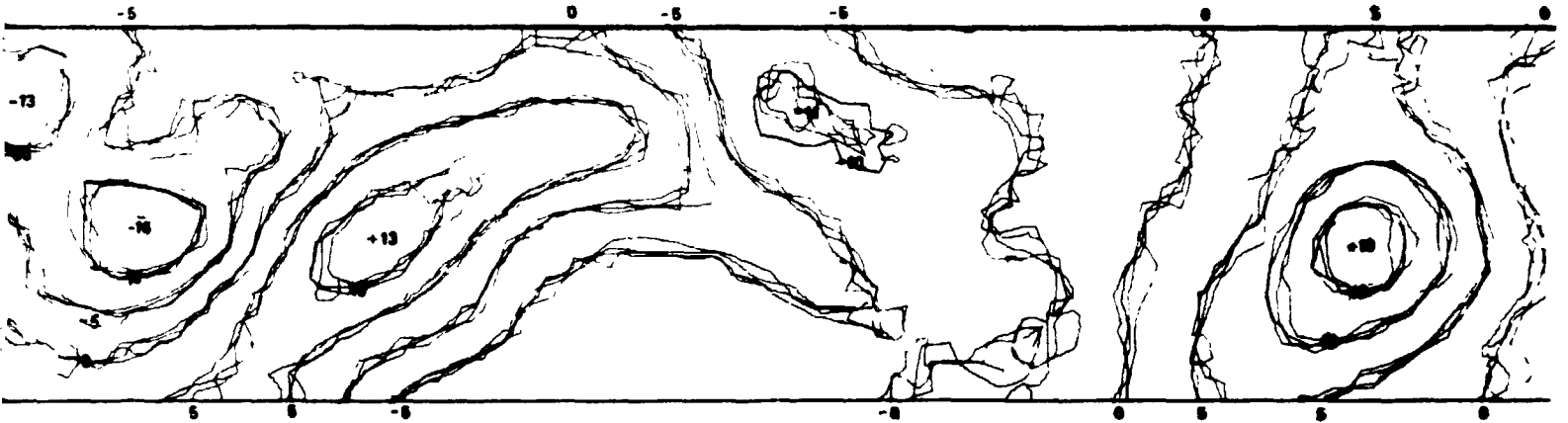
30 km ALTITUDE

4652-16



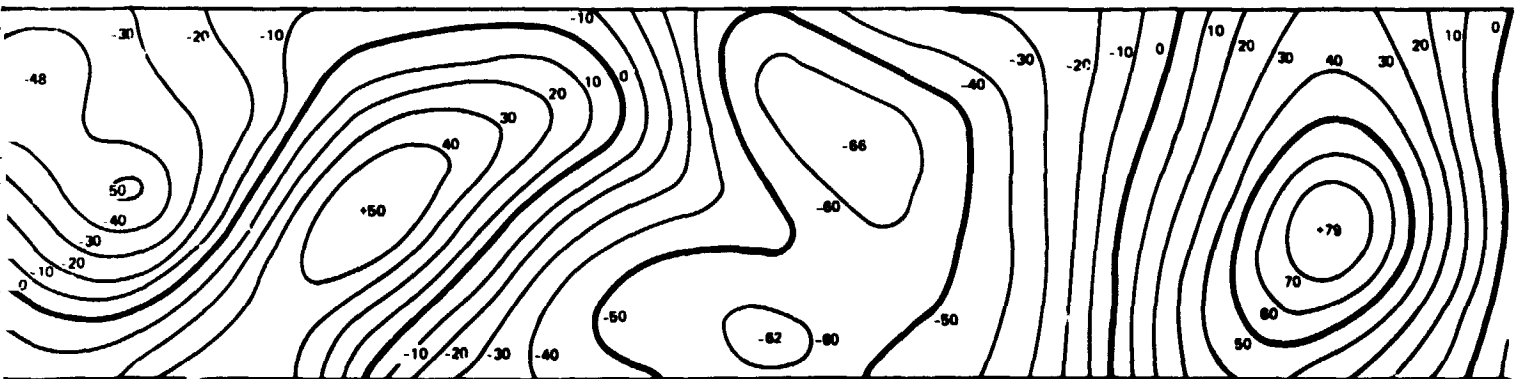
30 km ALTITUDE

4652-17



30 km ALTITUDE

4652-8



Effect of noise on contour plots.

A-57

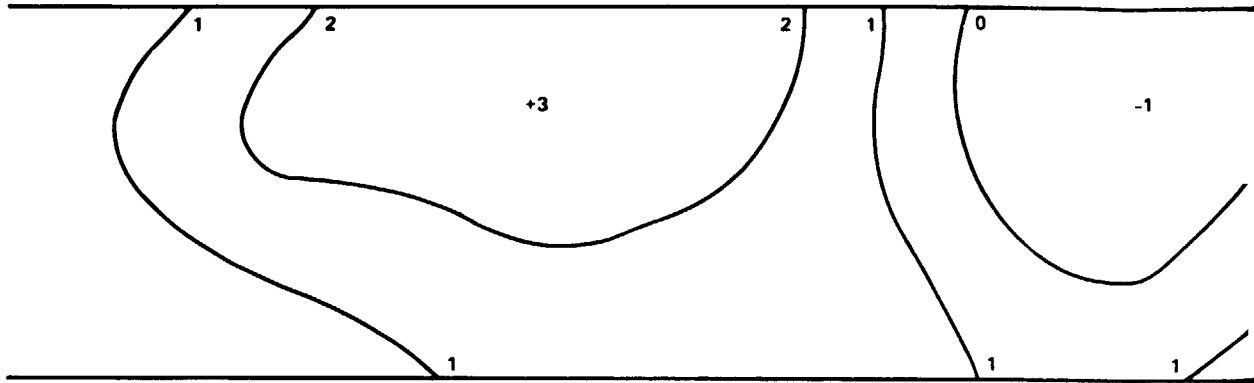
FOLDOUT FRAME 2

IX. GRAVITY MEASUREMENT AT HIGHER ALTITUDES

Most of the simulations presented in this paper have been at relatively low altitudes (15, 30, and 60 km). Although low, these altitudes were attained over many regions of the moon with the Apollo spacecraft and subsatellites and should be easily attainable with any reasonable spacecraft and mission design for an LPO mission, especially if the mission is planned to allow for initial surveys at higher altitudes (60 km) to obtain a good representation of the gravity field for orbital calculation before the spacecraft is moved into a lower orbit for the higher resolution surveys. However, for many reasons, the mission planners may want the option of operating at higher altitudes. What are the comparative merits of the two gravity measurement concepts at these altitudes? In Fig. 9 are plots of the vertical Doppler velocity change, the vertical gradient of the vertical gravity and the vertical gravity at 100 km. The contours for the Doppler velocity change are at 1 mm/sec change per resolution time (contour interval-to-single-point-noise level of 1) and the contours for the gradient are 1 Eotvos (similar signal-to-noise). We have plotted the contours directly without noise and feel that a direct comparison is valid since any measurement system integration, smoothing, spline fits, or other tricks to take advantage of the correlation between adjacent measurement points to reduce the noise level on the contours could be applied equally well to both Doppler velocity and gradient data. It seems obvious from inspection that even at 100 km altitude the gravity gradient data is superior in both resolution and amplitude-to-single-point-noise level. This does not hold true for higher altitudes, however. At 200 km the amplitude variations of the Doppler difference plot and the gradient plot have comparable S/N ratios (about 1:1) and at altitudes higher than 200 km, a 1 mm/sec at 10 sec Doppler system will outperform a 1 Eotvos at 10 sec gravity gradiometer system in exploring the larger anomalies.

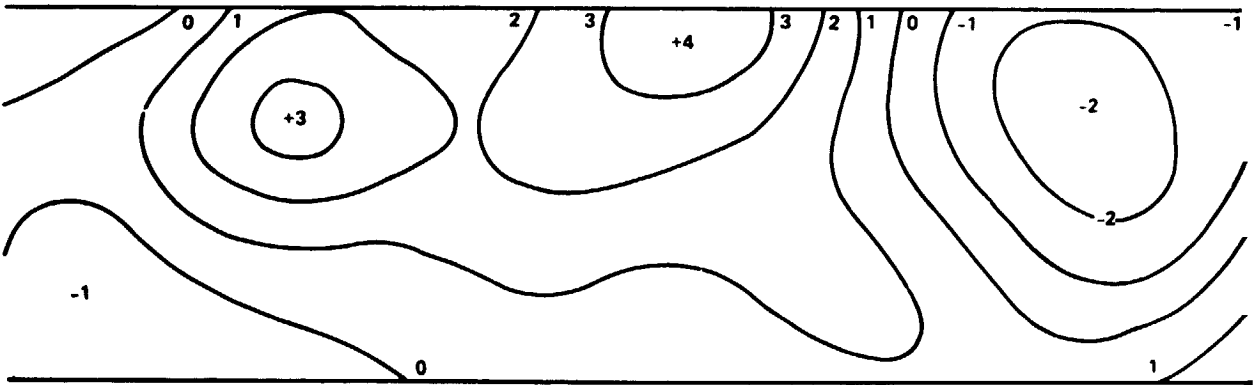
Δv_z , VERTICAL DOPPLER VELOCITY CHANGE, mm/sec CHANGE IN 15 km

1 mm/sec CHANGE
CONTOURS



Γ_{zz} , VERTICAL GRADIENT OF VERTICAL GRAVITY, EOTVOS

1 EOTVOS
CONTOURS



g_z , VERTICAL GRAVITY, mgal

5 mgal
CONTOURS

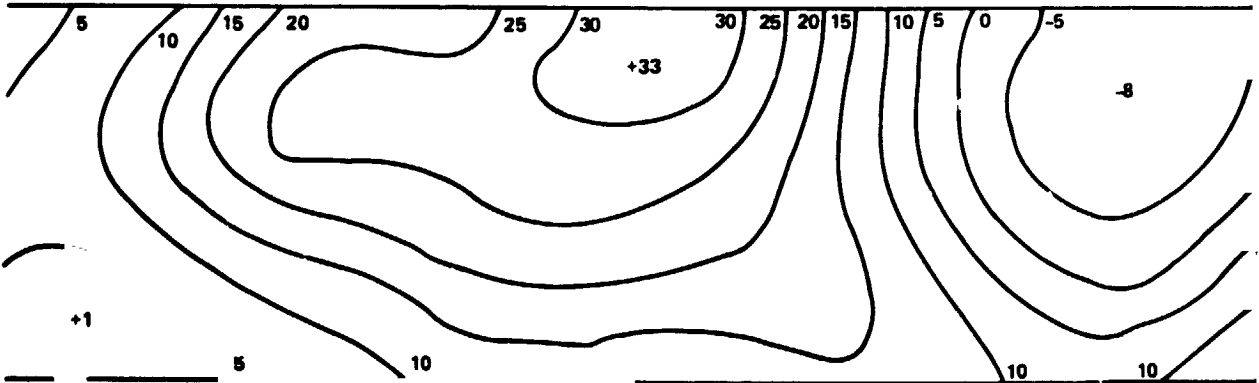


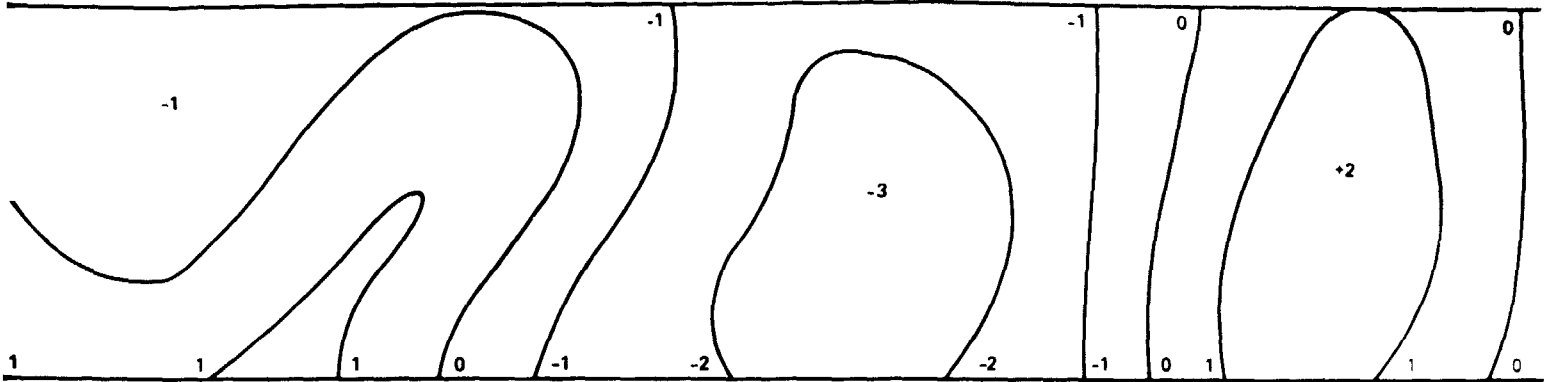
Fig. 9. Comparison of Dop

PRECEDING PAGE BLANK NOT FILMED

FOLDOUT FRAME /

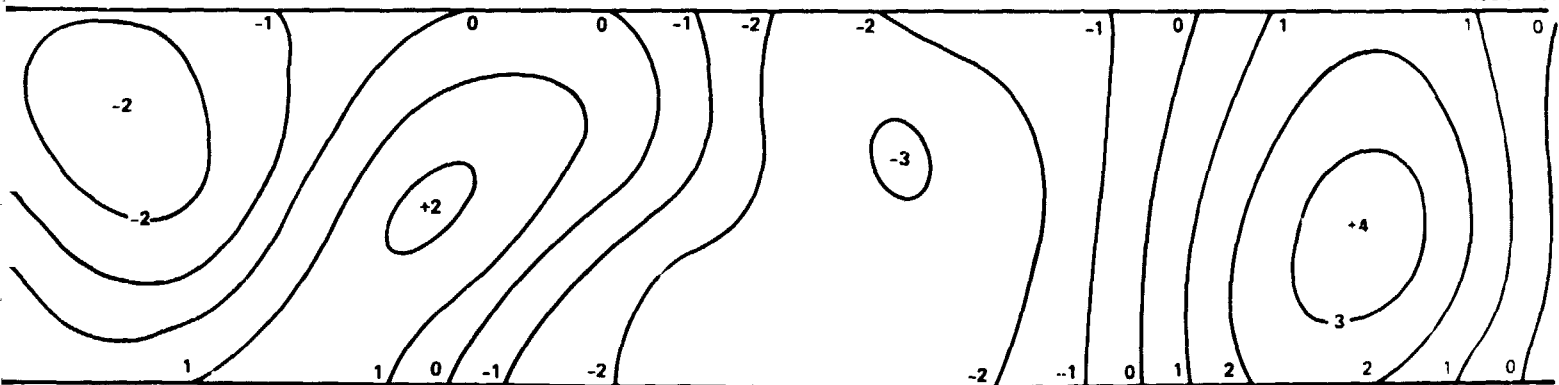
100 km ALTITUDE

4652-18



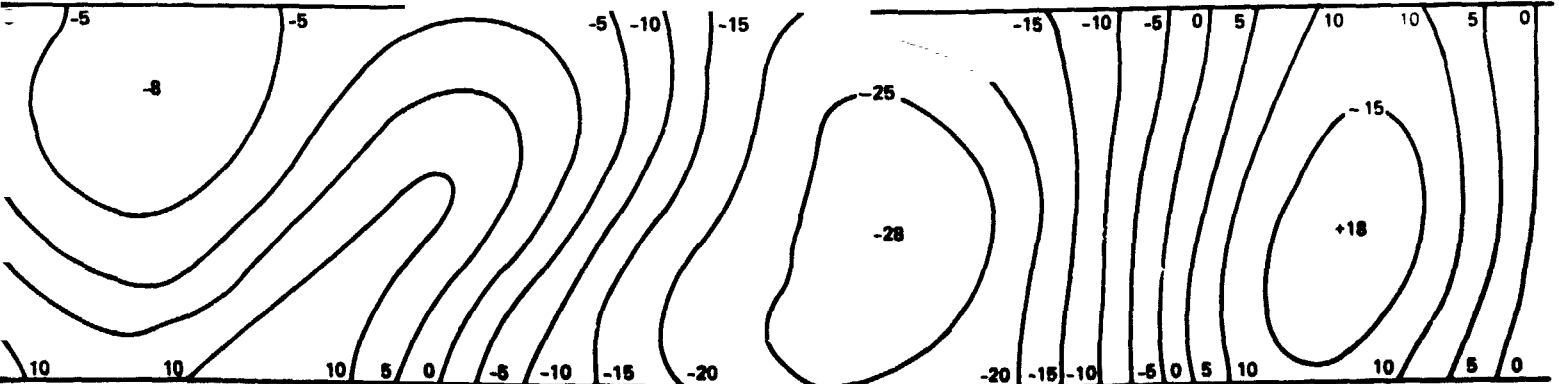
100 km ALTITUDE

4652-19



100 km ALTITUDE

4652-20



Comparison of Doppler and Gradients at 100 km.

A-61

FOLDOUT

X. SUMMARY

In summary, a set of simulations of the gravity data to be expected from an LPO spacecraft utilizing the state of the art in both Doppler velocity tracking systems and gravity gradiometer instrument systems has been simulated using a point mass model that gives an excellent representation of the types of gravity anomalies to be found on the moon. If the state-of-the-art in instrumentation of both systems remains at the levels of ± 1 mm/sec for 10 sec integration time for the Doppler velocity tracking system and ± 1 Eotvos for 10 sec integration time for the gravity gradiometer system, it is seen by inspection of the simulation plots that the gravity gradiometer system will give higher resolution data with higher signal-to-measurement noise ratio than the Doppler tracking system at all altitudes below 100 km. The simulations concentrated on instrumentation errors and did not cover many of the systematic error sources involving spacecraft altitude, attitude, angular rate, position or accelerations. It is recommended that the simulations be redone using a more complete error model and a more rigorous error analysis to quantify the differences in performance of the two systems.

ACKNOWLEDGEMENTS

The author would like to acknowledge helpful criticism from Bill Sjogren, Ananda Mohan, Jack Lovell, Andy Park and others that improved the presentation and tempered the assertions – for which the author takes full responsibility.

The author would especially like to acknowledge the expert assistance of Mr. Roger Lowe whose programming expertise kept the computer costs of these simulations within bounds.

REFERENCES

1. Lunar Polar Orbiter Program - Interim Technical Report, X-703-75-141, Goddard SFC, Greenbelt, Maryland (May 1975).
2. R. L. Forward, "Gravitational Field Measurements of Planetary Bodies with Gravity Gradient Instrumentation," Proc. AAS/AIAA Astrodynamics Specialists Conf., Ft. Lauderdale, Fla. (17-19 Aug. 1971).
3. R. L. Forward, "Review of Artificial Satellite Gravity Gradiometer Techniques for Geodesy," First International Symposium on Use of Artificial Satellites for Geodesy and Geophysics, Athens, Greece, (14-21 May 1973).
4. W. L. Sjogren, R. N. Wimberly and W. R. Wollenhaupt "Lunar Gravity via the Apollo 15 and 16 Subsattellites," The Moon, 9, 115-128 (1974).
5. W. L. Sjogren, R. N. Wimberly and W. R. Wollenhaupt, "Lunar Gravity: Apollo 17," The Moon, 11, 41-52 (1974).
6. Warren G. Heller, "Gradiometer-Aided Inertial Navigation," Report TR-312-5 prepared under Contract DMA 700-74-C-0075, The Analytical Sciences Corp (TASC), 6 Jacob Way, Reading, Mass. 01867 (7 April 1975).

APPENDIX A

ROTATING COMPONENTS OF THE TENSOR GRAVITY GRADIENT FIELD OF A POINT MASS TO A MEASUREMENT POINT COORDINATE SYSTEM FROM THE POINT MASS COORDINATE SYSTEM.

As shown in Fig. A-1, a point mass at the position $(x_1, y_1, 0)$ produces a gravity gradient tensor field at the measurement point $(0, 0, h)$ that is tilted with respect to the x, y, z lunar coordinate system. To determine the gravity gradient tensor components in the lunar vertical coordinate system we must determine the rotation matrix coupling the two coordinate systems.

To rotate from lunar coordinates to the coordinate system defined by the mass point and the measurement point we first rotate the lunar (x, y, z) coordinate system about z until the y axis goes through $(x_1, y_1, 0)$. This is a negative ϕ rotation that moves y to the η axis and x to the ξ axis, with the ζ axis remaining identical to the z axis. We then rotate the (ξ, η, ζ) coordinate system an angle θ about the ξ axis through the point $(0, 0, h)$ to tilt the ζ (vertical) axis until it intersects $(x_1, y_1, 0)$. The rotation moves the η axis to the y' axis the ζ axis to the z' axis while the ξ axis becomes the x' axis. The principal axes of the gravity gradient tensor of the mass point are now seen to be oriented along the (x', y', z') coordinate system. To rotate the tilted tensor into lunar coordinates, reverse the above. Using the general rotation matrix from Goldstein page 109,* with $\psi = 0$ ($\sin \psi = 0, \cos \psi = 1$). The rotation matrix is:

$$S_{ki} = \begin{pmatrix} \cos \phi & \sin \phi & 0 \\ -\cos \theta \sin \phi & \cos \theta \cos \phi & \sin \theta \\ \sin \theta \sin \phi & -\sin \theta \cos \phi & \cos \theta \end{pmatrix}$$

*H. Goldstein, Classical Mechanics, Addison-Wesley, Cambridge, Mass. (1950).

and it's inverse is:

$$S_{j\ell}^{-1} = \begin{pmatrix} \cos \phi & -\cos \theta \sin \phi & \sin \theta \sin \phi \\ \sin \phi & \cos \theta \cos \phi & -\sin \theta \cos \phi \\ 0 & \sin \theta & \cos \theta \end{pmatrix} .$$

The gravity gradient tensor at a point $(0, 0, h)$ from a mass M at $(x, y, 0)$ is given in the x', y', z' system as

$$\Gamma'_{ij} = \frac{GM}{R^3} \begin{pmatrix} -1 & 0 & 0 \\ 0 & -1 & 0 \\ 0 & 0 & 2 \end{pmatrix} .$$

We now want to rotate this to the lunar x, y, z system, so we reverse the rotation

$$\Gamma_{kl} = S_{ki}^{-1} \Gamma'_{ij} S_{j\ell}$$

to obtain the gravity gradient components in the (x, y, z) lunar coordinate system:

$$\Gamma_{kl} = \begin{pmatrix} [-1 + 3 \sin^2 \theta \sin^2 \phi] & [-3 \sin^2 \theta \sin \phi \cos \phi] & [3 \sin \theta \cos \theta \sin \phi] \\ [-3 \sin^2 \theta \sin \phi \cos \phi] & [-1 + 3 \sin^2 \theta \cos^2 \phi] & [-3 \sin \theta \cos \theta \cos \phi] \\ [3 \sin \theta \cos \theta \sin \phi] & [-3 \sin \theta \cos \theta \cos \phi] & [2 - 3 \sin^2 \theta] \end{pmatrix} \frac{GM}{R^3} .$$

$$= \begin{pmatrix} \Gamma_{xx} & \Gamma_{xy} & \Gamma_{xz} \\ \Gamma_{yx} & \Gamma_{yy} & \Gamma_{yz} \\ \Gamma_{zx} & \Gamma_{zy} & \Gamma_{zz} \end{pmatrix} .$$

From the geometry of Fig. A-1 we see that:

$$\rho^2 = x_1^2 + y_1^2$$

$$R^2 = \rho^2 + h^2$$

$$\cos \phi = \frac{y_1}{\rho} \quad , \quad \cos \theta = \frac{h}{R}$$

$$\sin \phi = \frac{-x_1}{\rho} \quad , \quad \sin \theta = \frac{\rho}{R} .$$

These can be used in place of the angles in computing the tensor components. (Take care to reduce the equations to eliminate ρ from the denominator since $\rho = 0$ for a mass point directly under the measurement point.)

6337-26

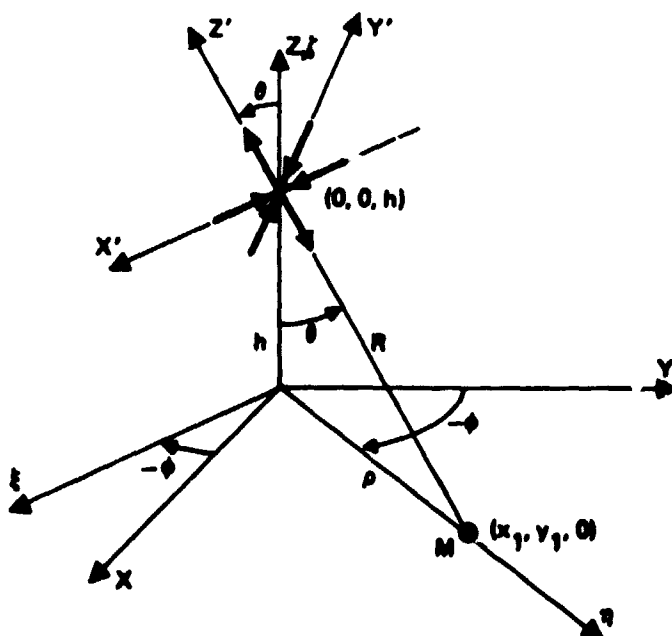


Fig. A-1.
Rotation of gradient tensor.

APPENDIX B

FUNCTIONAL AND PHYSICAL DESCRIPTION
GRAVITY ENVIRONMENT MEASUREMENT SYSTEM
(GEMS)

FUNCTIONAL AND PHYSICAL DESCRIPTION
GRAVITY ENVIRONMENT MEASUREMENT SYSTEM
(GEMS)

JUNE 1976

R. M. TEMPLE, HUGHES AIRCRAFT COMPANY
D. H. SWENSON, JET PROPULSION LABORATORY
I. TONAI, HUGHES AIRCRAFT COMPANY
W. E. WILLIAMS, HUGHES AIRCRAFT COMPANY

TABLE OF CONTENTS

- 1.0 SCOPE
- 2.0 APPLICABLE DOCUMENTS
- 3.0 FUNCTIONAL DESCRIPTION
 - 3.1 SCIENTIFIC OBJECTIVES
 - 3.2 EXPERIMENTAL APPROACH
 - 3.3 MAJOR FUNCTIONAL ELEMENTS
 - 3.3.1 RGG Sensor
 - 3.3.1.1 Arm/Pivot Structure
 - 3.3.1.2 Transducer
 - 3.3.1.3 Spin Bearings
 - 3.3.1.4 Spin Motors
 - 3.3.1.5 Speed Sensing
 - 3.3.1.6 RF Transformers
 - 3.3.2 Electronics
 - 3.3.2.1 Speed Control Elements
 - 3.3.2.2 Power Supply and Thermal Control Electronics
 - 3.3.2.3 Data Output Electronics
 - 3.3.2.4 Test and Control Electronics
 - 3.4 OPERATING MODES
 - 3.5 PRELIMINARY SPACE GEMS ELECTRONICS SUBSYSTEM DESIGN
- 4.0 PHYSICAL DESCRIPTION
 - 4.1 SENSOR ARMS
 - 4.2 INNER ROTOR HOUSING
 - 4.3 PIVOT SPRINGS
 - 4.4 ARM/PIVOT/CENTER PLATE FABRICATION
 - 4.5 TRANSDUCERS
 - 4.6 OUTER ROTOR

- 4.7 STATOR
- 4.8 INTERNAL ELECTRONICS PACKAGING
- 4.9 EXTERNAL ELECTRONICS PACKAGING
- 5.0 SPECIAL REQUIREMENTS
 - 5.1 SENSOR LOCATION ON S/C
 - 5.2 SENSOR ALIGNMENT
 - 5.3 S/C ATTITUDE CONTROL RATES
 - 5.4 S/C ATTITUDE CONTROL ACCELERATIONS
 - 5.5 SENSOR THERMAL CONTROL
 - 5.5.1 Objective
 - 5.5.2 Assumptions
 - 5.5.3 Preliminary Analysis
 - 5.5.4 Thermal Design Approach
 - 5.5.5 Results
 - 5.5.6 Conclusions
 - 5.6 SENSOR DYNAMIC CHARACTERISTICS
- 6.0 INTERFACE DEFINITIONS
 - 6.1 MECHANICAL/WEIGHT/VOLUME
 - 6.2 THERMAL
 - 6.3 POWER
 - 6.4 COMMAND
 - 6.5 DATA
- 7.0 PERFORMANCE PARAMETERS
 - 7.1 SENSITIVITY
 - 7.2 DYNAMIC RANGE

- 7.3 QUANTIZATION
- 7.4 ALIGNMENT
- 7.5 SPIN SPEED
- 7.6 SPIN SPEED ACCURACY
- 7.7 TEMPERATURE
- 7.8 SENSITIVITY TO SPURIOUS EXTERNAL FIELDS
- 7.9 GENERATION OF INTERFERENCE FIELDS
- 8.0 SAFETY CONSIDERATIONS
- 9.0 MISSION CONSIDERATIONS

1.0 SCOPE

This document covers the functional and physical description and the functional performance parameters of the Gravity Environment Measurement Subsystem (GEMS). In addition, the sensor/spacecraft interface characteristics and constraints are defined. This document is intended to be a working document with the addition of data following selection of the specific spacecraft.

2.0 Applicable Documents

- (1) MJU Spacecraft Description Document
- (2) JPL Document 660-6
- (3) "Rotating Gravity Gradiometer Study", Final Report on JPL Contract 954309 under NASA Contract NAS7-100 for the period from August 1975 through June 1976, Hughes Research Laboratories, Malibu, CA 90265. (The final report of which this document is an Appendix.)

3.0 Functional Description

3.1 Scientific Objectives

The objective of the Gravity Experiment is to obtain a high resolution, free-air gravity map of the moon. The gravity data will be combined with orbital, Doppler tracking, altimetry and photographic data to obtain a high resolution global gravity map for:

- a. Orbital dynamics predictions
- b. Geodesy
- c. Geophysics
- d. Cartography

Gravity gradient data may also be combined with other data to improve post-mission knowledge of spacecraft orbit and attitude.

3.2 Experimental Approach

The Gravity Environment Measurement System (GEMS), which consists of one or more Rotating Gravity Gradiometer (RGG) sensors and supporting electronics, will be used to obtain the in-situ lunar gravity field data. A general block diagram of a typical GEMS for space application is illustrated in Figure 1.

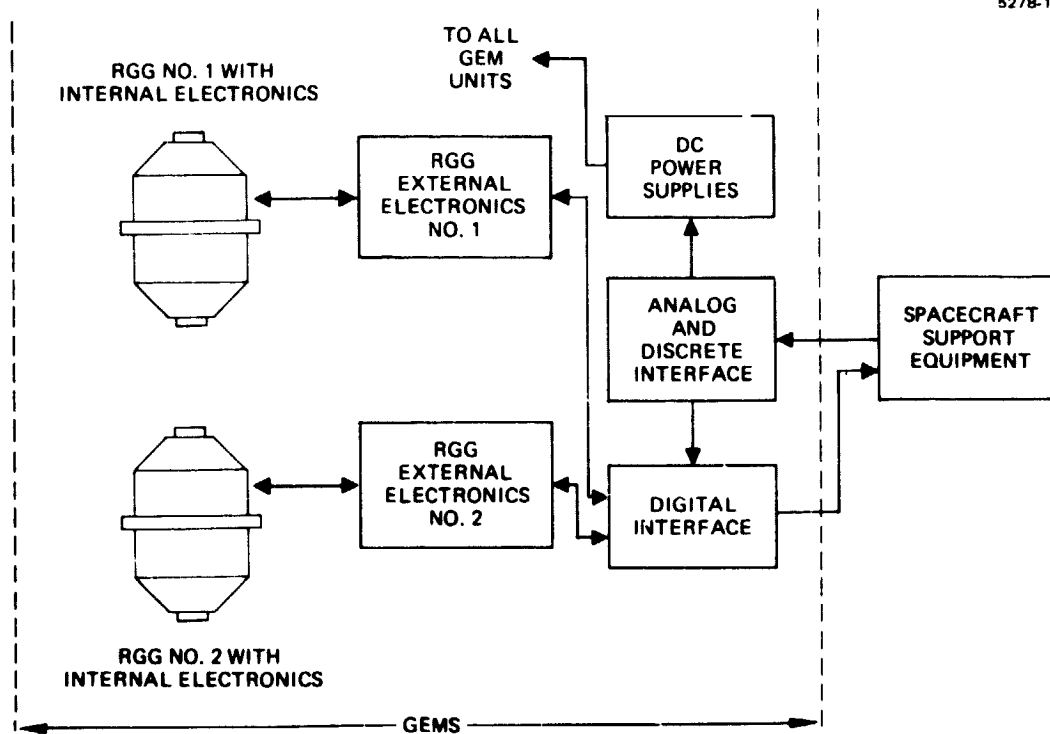


Figure 1. Gravity Environment Measurement System (GEMS) for Space Applications

The system illustrated comprises two Rotating Gravity Gradiometers (RGG's) with internal electronics, an external electronics unit for each RGG, and common power supplies and interface units. The LPO spacecraft (S/C) support equipment is also shown to indicate the interface requirement. The interface is functionally the same regardless of the number of RGG's in the system. However, the number of data and command registers would vary.

Each RGG instrument or "sensor" has two output signals. One of these is a direct measure of the cross gradient tensor component in the plane of the sensor rotation and the other signal is a measure of the difference of the two principal gradient tensor components in the plane of rotation. The "principal gradient difference" outputs of three mutually orthogonal sensors are required to determine the principal gradient tensor components separately. However, for the LPO application, studies indicate that it is possible to obtain adequate data for determining subsurface mascon densities with

two, or even one RGG sensor. This is discussed in detail in Task 3 and 5 of document (3) referenced in Section 2 above.

For simplicity, the following discussions will be based on a one-RGG system.

3.3 Major Functional Elements

3.3.1 RGG Sensor

Figure 2 is a photograph of a prototype RGG. The connector panels at top left and bottom left and the base against which the rule is leaning are temporary items used for laboratory testing. In operation, the RGG is mounted by the center flange which is about 23 cm in diameter. The RGG is 30 cm long as pictured, but will be slightly longer when cooling fins are added at each end.

3.3.1.1 Arm/Pivot Structure

The basic elements of the RGG sensor are shown diagrammatically in Figure 3. Two arms with masses, M , at the ends are oriented at 90 degrees with respect to each other. They are mechanically coupled by a torsional pivot spring and supported within a housing by additional torsional pivot springs.

3.3.1.2 Transducer

Figure 4 shows a piezoelectric transducer attached to the arms. The supports cause the transducer to bend in proportion to the differential motion of the arms about the pivot axis. This bending action produces an output voltage proportional to the gravity gradient field.

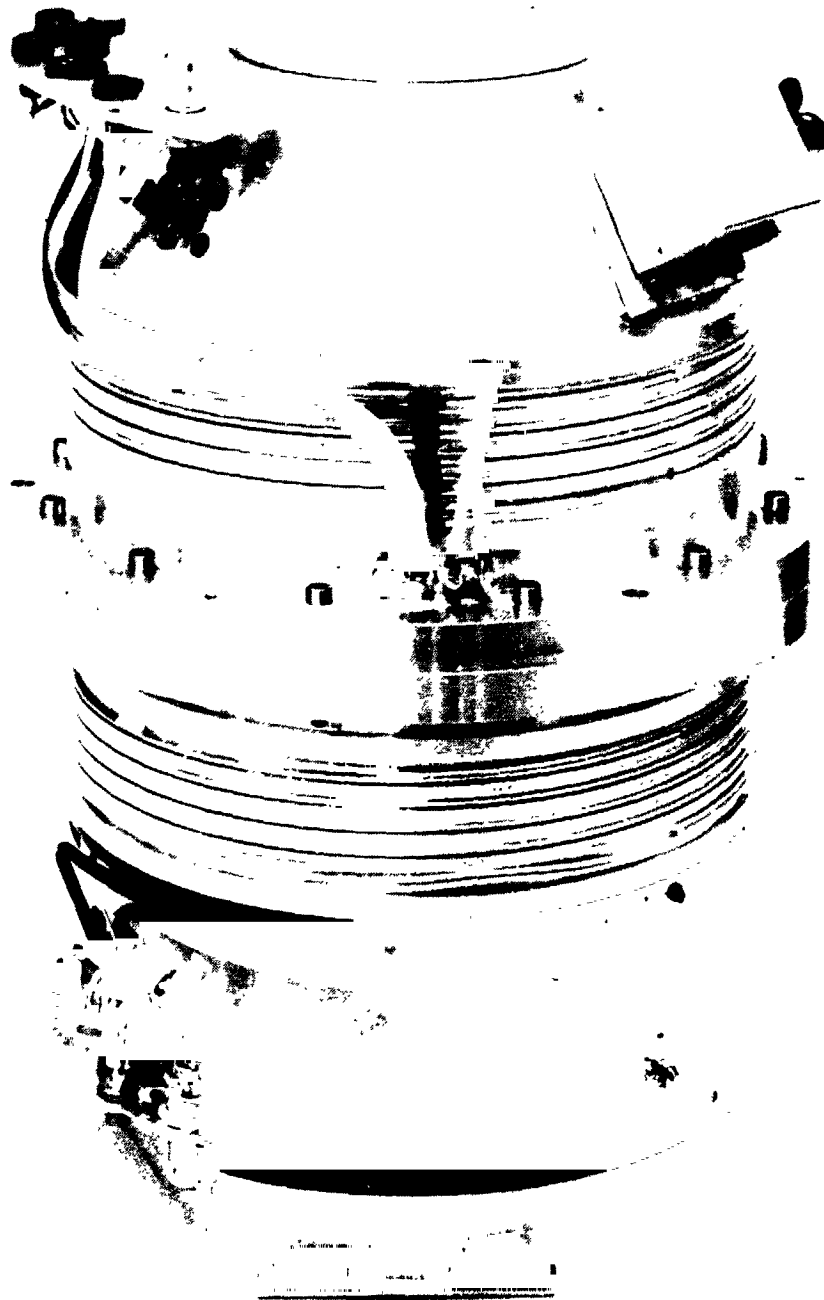


Figure 2. Hughes Prototype Rotating Gravity Gradiometer (RGG)

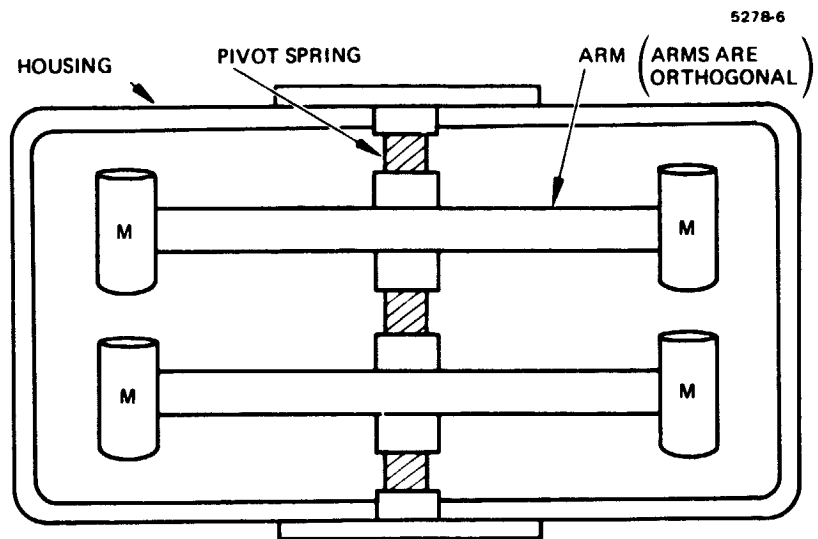


Figure 3. RGG Arm/Pivot Structure

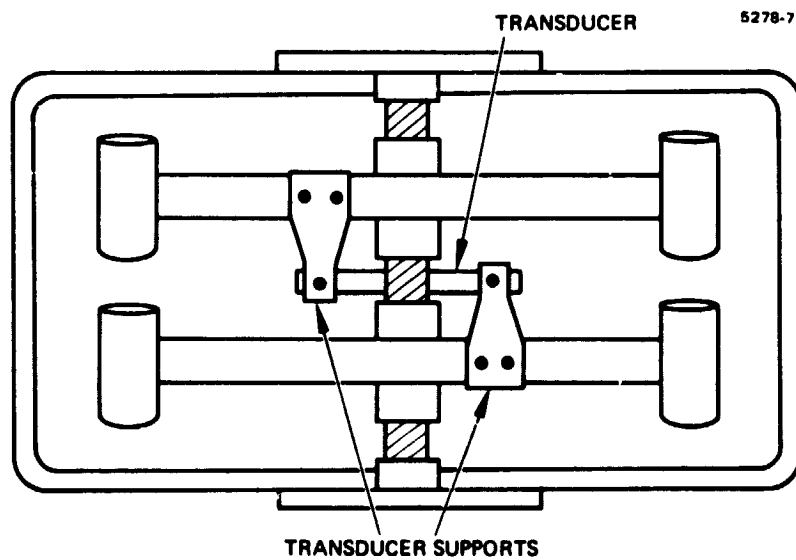


Figure 4. Addition of Piezoelectric Transducer

3.3.1.3 Spin Bearings

The arm/pivot/transducer/inner-case assembly called the rotor, which also includes other elements such as the internal electronics discussed below, is supported on a pair of precision hydrodynamic oil bearings, as diagrammed in Figure 5.

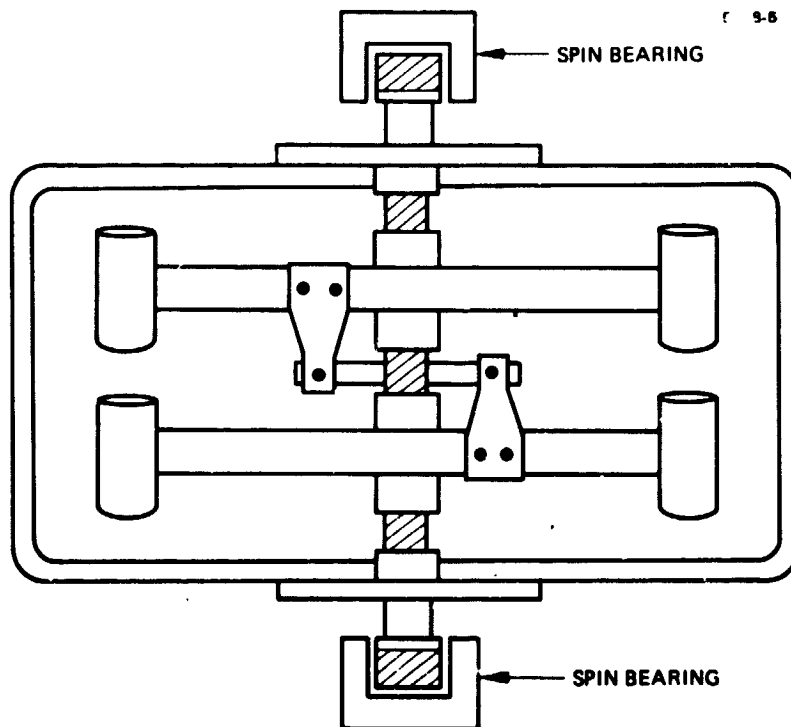


Figure 5. Addition of Spin Bearings

3.3.1.4 Spin Motors

The rotor is spun within an evacuated outer case called the stator by a pair of asynchronous eddy-current drag-cup motors, one at each end, as diagrammed in Figure 6.

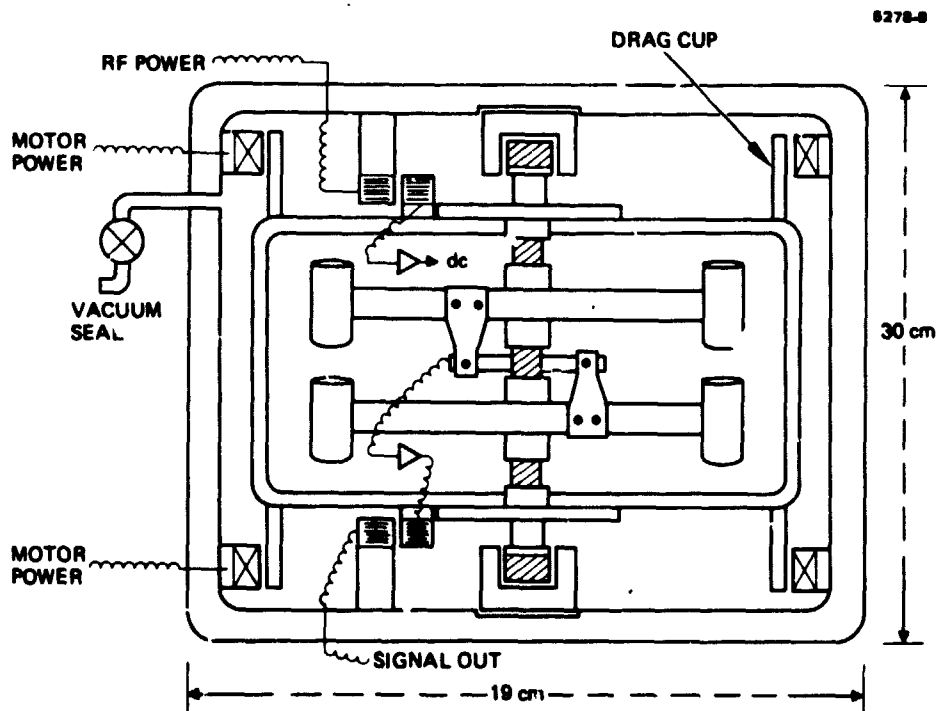


Figure 6. Addition of Motors, Transformers and Stator

3.3.1.5 Speed Sensing

An eight-slot disc at the base of one drag cup is pictured in Figure 7. Optical sensing of the slots, one of which is wider

5278-19

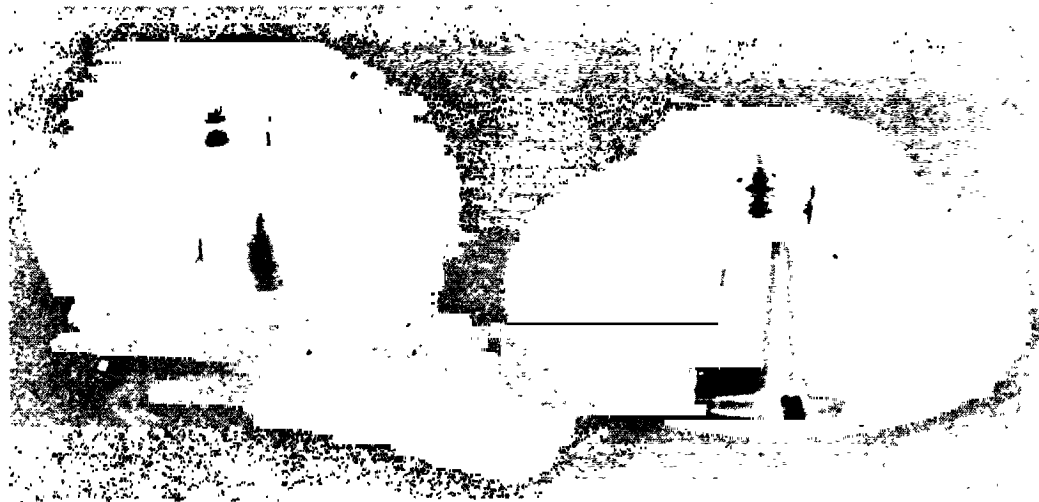


Figure 7. RGG Drag Cups, One with Speed Control Slotted Disc

than the other, plus digital processing and a closed loop servo provides the rotor-to-stator position, speed data, and speed control. This is covered in more detail under electronics, Section 3.3.

3 3.1.6 RF Transformers

The sensor has two rotary transformers, also shown in Figure 6. One is used to transmit RF power and logic signals to the rotor to supply power for the internal electronics and control the sensor output mode condition. The other transformer is used to transmit gravity gradient and test signals from the rotor to external electronics.

3.3.2 Electronics

The GEMS electronics and related elements for space applications, as shown in Figure 8, contains three parts. The portion which is contained within the RGG is shown at the left within the symbolic RGG outline; related electronics, which are external to the RGG, are shown in the center; and the spacecraft support equipment is at the right. However, for easier comprehension, the electronics will be divided into functional portions in the following discussions.

3.3.2.1 Speed Control Elements

Figure 9 shows the GEMS functional elements which constitute the speed control. A light emitting diode (LED) and photo diode sensor (under the box protruding from the sensor case at the upper right in Figure 2) detect the eight slots in the slotted disc (See Figure 7). This signal is amplified and shaped by the photo pickoff providing eight digital pulses per revolution of the rotor (8 w pulses) to the digital interface. Here the time between octant pulses is determined by counting the output of a high precision 10 MHz clock.

The count for each octant is corrected for irregular slot spacing and compared with a commanded number representing the required speed. The difference between the corrected octant count and the command speed number is added to a long-term error count forming the speed error value. This digital number is converted to an analog signal by the D/A converter and sent to the motor driver and 2-channel amplifier to drive the RGG motors to a higher or lower speed. This correction is accomplished 8 times per revolution and maintains the rotor speed to within one part in ten million. RGG speed control timing and flow chart are shown in Figures 10 and 11.

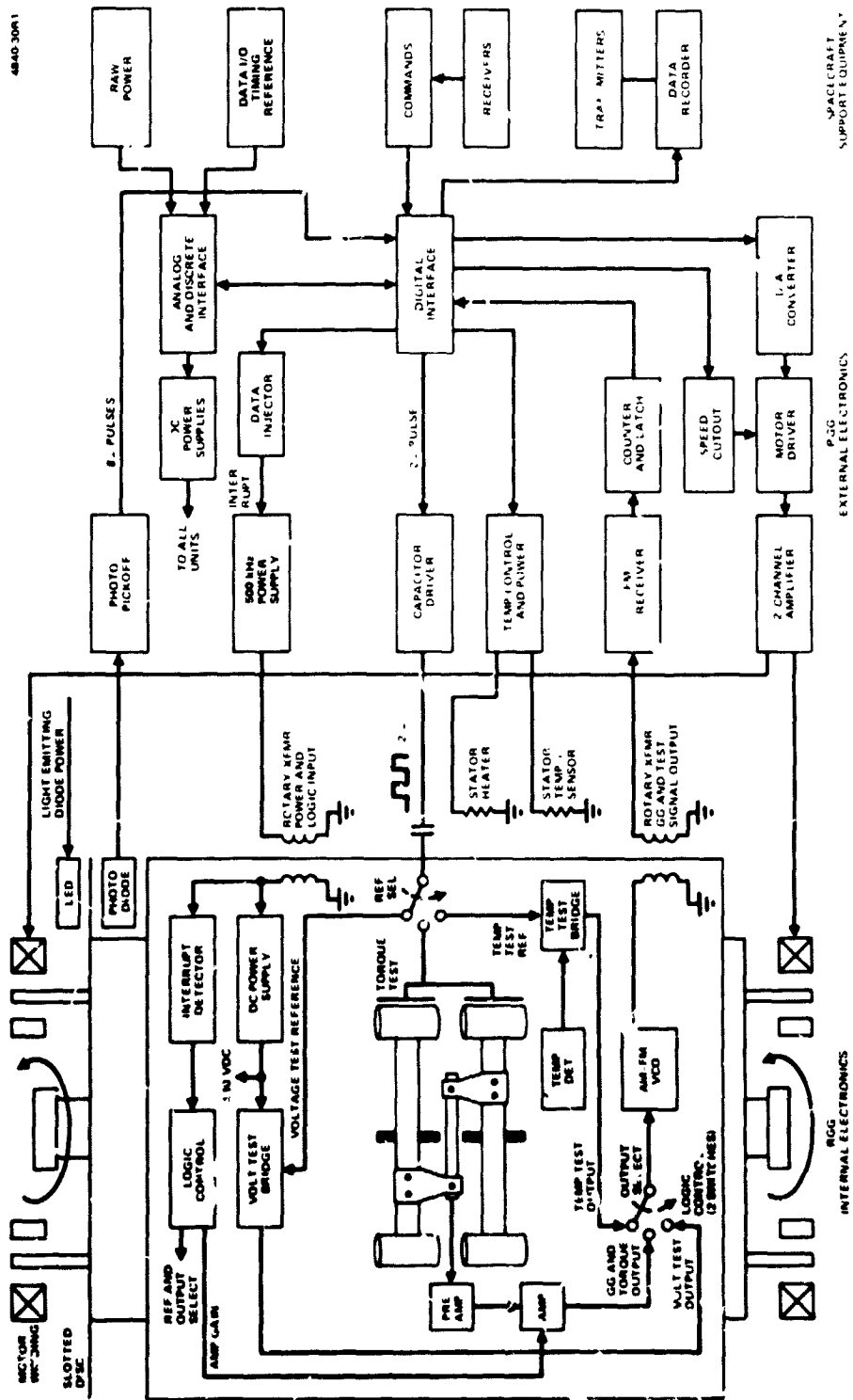
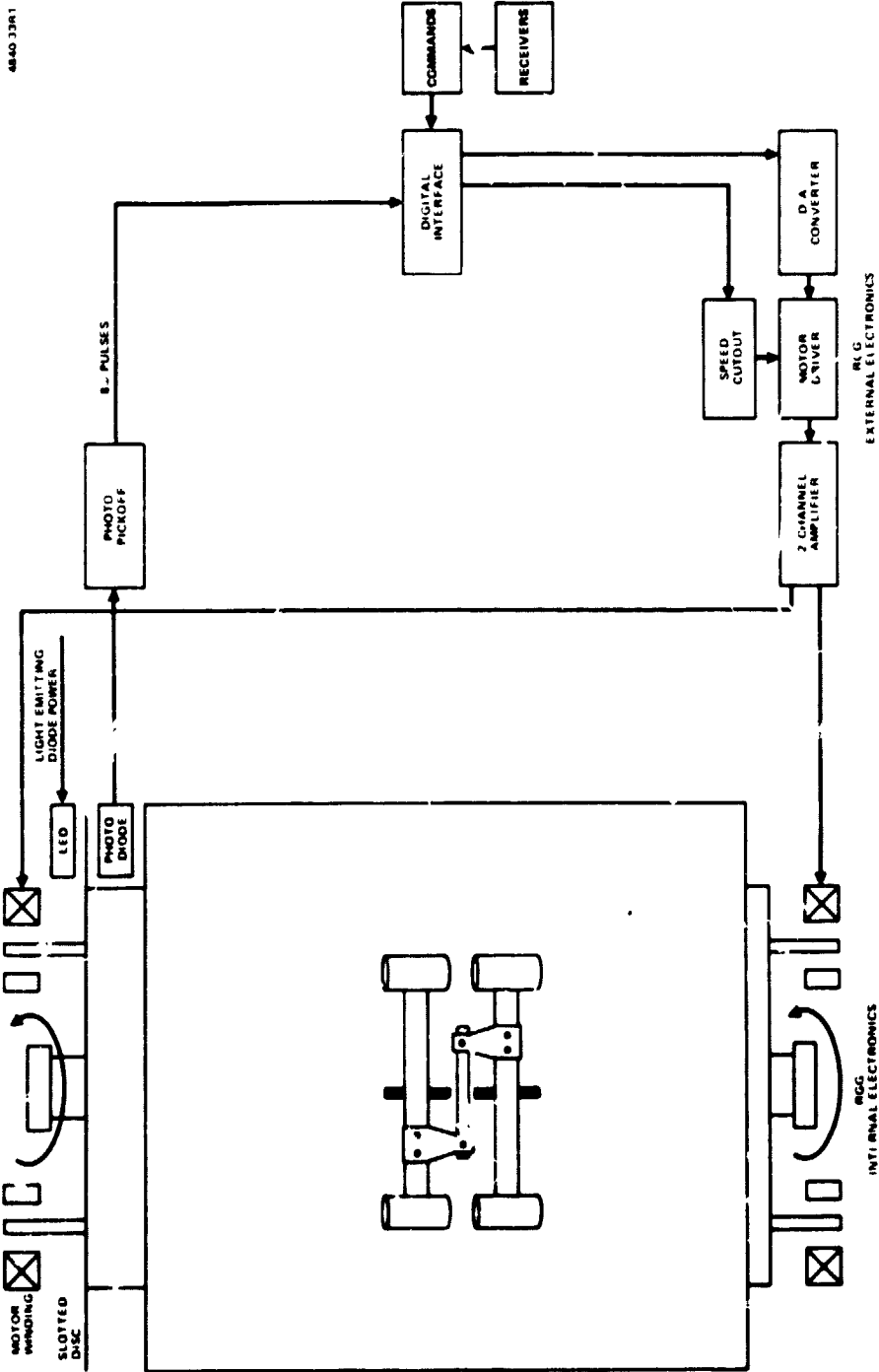


Figure 8. GEMS KGG and Electronics for Space Applications

ORIGINAL PAGE IS
OF POOR QUALITY



4840 13R1

Figure 9. GEMS Speed Control Elements

ORIGINAL PAGE IS
OF POOR QUALITY

4880-24

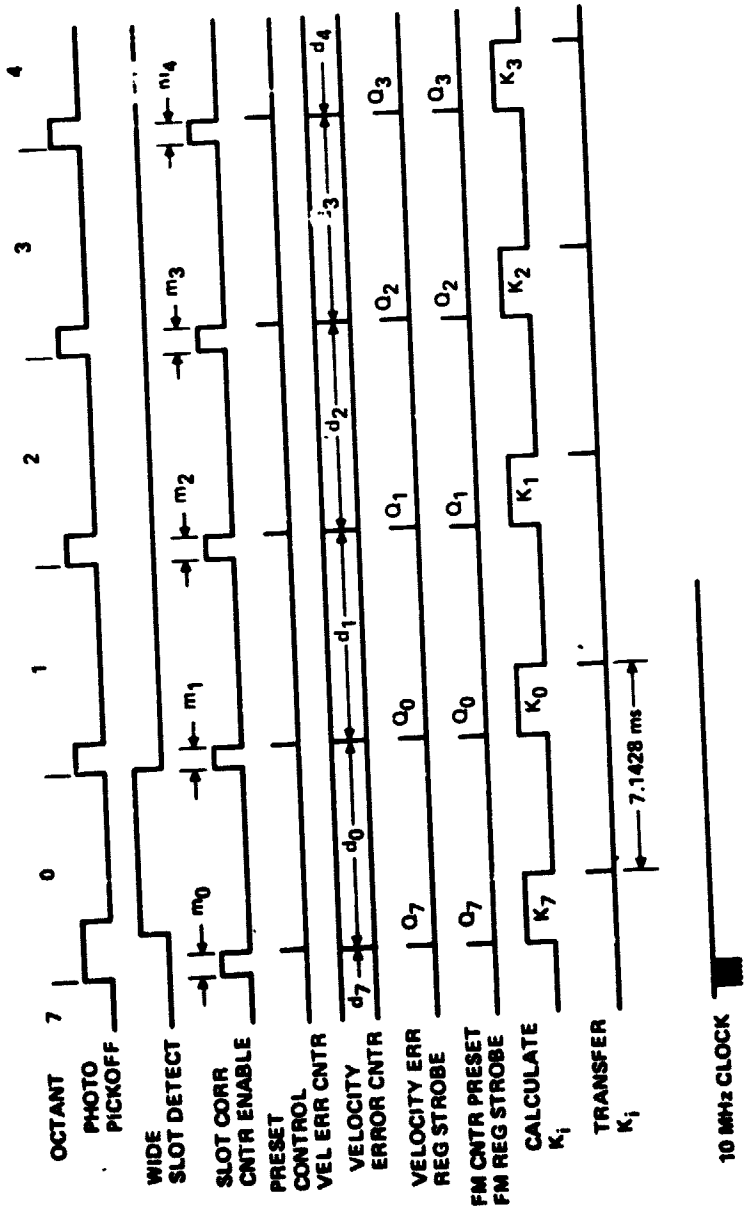
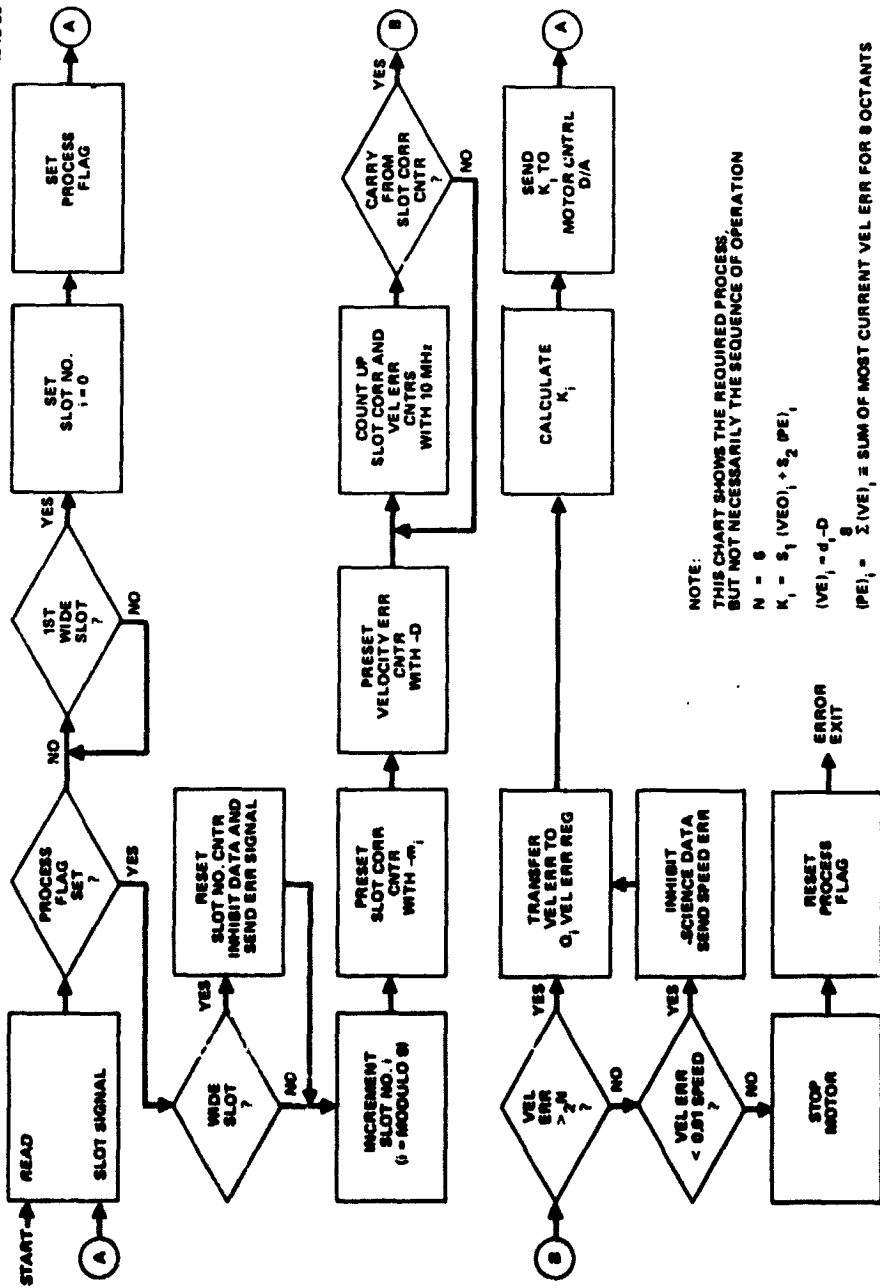


Figure 10. RGG Speed Control Timing

ORIGINAL PAGE IS OF POOR QUALITY



NOTE:
 THIS CHART SHOWS THE REQUIRED PROCESS
 BUT NOT NECESSARILY THE SEQUENCE OF OPERATION
 $N = 8$
 $K_1 = S_1 (VE)_1 + S_2 (PE)_1$
 $(VE)_1 = d_1 - D$
 $(PE)_1 = \sum (VE)_i = \text{SUM OF MOST CURRENT VEL ERR FOR 8 OCTANTS}$

Figure 11. RGG Speed Control Flow Chart

3.3.2.2 Power Supply and Thermal Control Electronics

GEMS receives raw 28 VDC power from the S/C. This raw power is converted to the required power forms in the external electronics or into RF for transmission through one of the rotary transformers to the RGG rotor. The RF is rectified and filtered to provide DC for the RGG internal electronics. It is assumed that raw power switching will be performed by the S/C power subsystem.

Temperature control of the RGG stator begins with a commanded temperature operating point received via the digital interface, as shown in Figure 12, and set into the temperature control unit. Two temperature sensors are used; one measures the ambient temperature and the other the RGG case temperature. The latter sensor is a special wire wound in a small helical slot on the periphery of each half of the stator and a heater wire is likewise wound in a larger helical slot in each half interleaved with the sensor wire slot (See Figure 2). The sensors and heaters together with the temperature control and power unit provide a closed loop servo to maintain the RGG case within ± 0.06 C of the commanded operating temperature point.

3.3.2.3 Data Output Electronics

Gravity gradients stimulate the rotating arm/mass/pivot/transducer structure to oscillate with an alternating angular motion at the 2ω (approximately 35 Hz) resonant frequency, producing an amplitude modulated signal from the piezoelectric transducer. Operating at resonance results in (1) a mechanical amplification of the gradient induced differential arm motion of about 300 (Q approximately equal to 300) and (2) mechanical filtering of noise signals before the transducer converts the mechanical motion to an electrical signal. This significantly increases the signal-to-noise ratio over that which could be attained with electronic amplification alone.

The electrical signal is amplified, first by a balanced pair of low-noise field-effect transistors (FET's) in the preamplifier, and then by an amplifier with controllable normal-gain and low-gain modes (See Figure 13). Additional electronic tuned filtering is also provided.

The amplitude-modulated signal is converted to a frequency-modulated (FM) signal by a 200 KHz mid-frequency voltage controlled oscillator (VCO) type modulator. This FM signal is then transmitted to the external electronics through a rotary transformer. Another rotary RF transformer at the other end of the sensor is used for transmitting power into the RGG rotor.

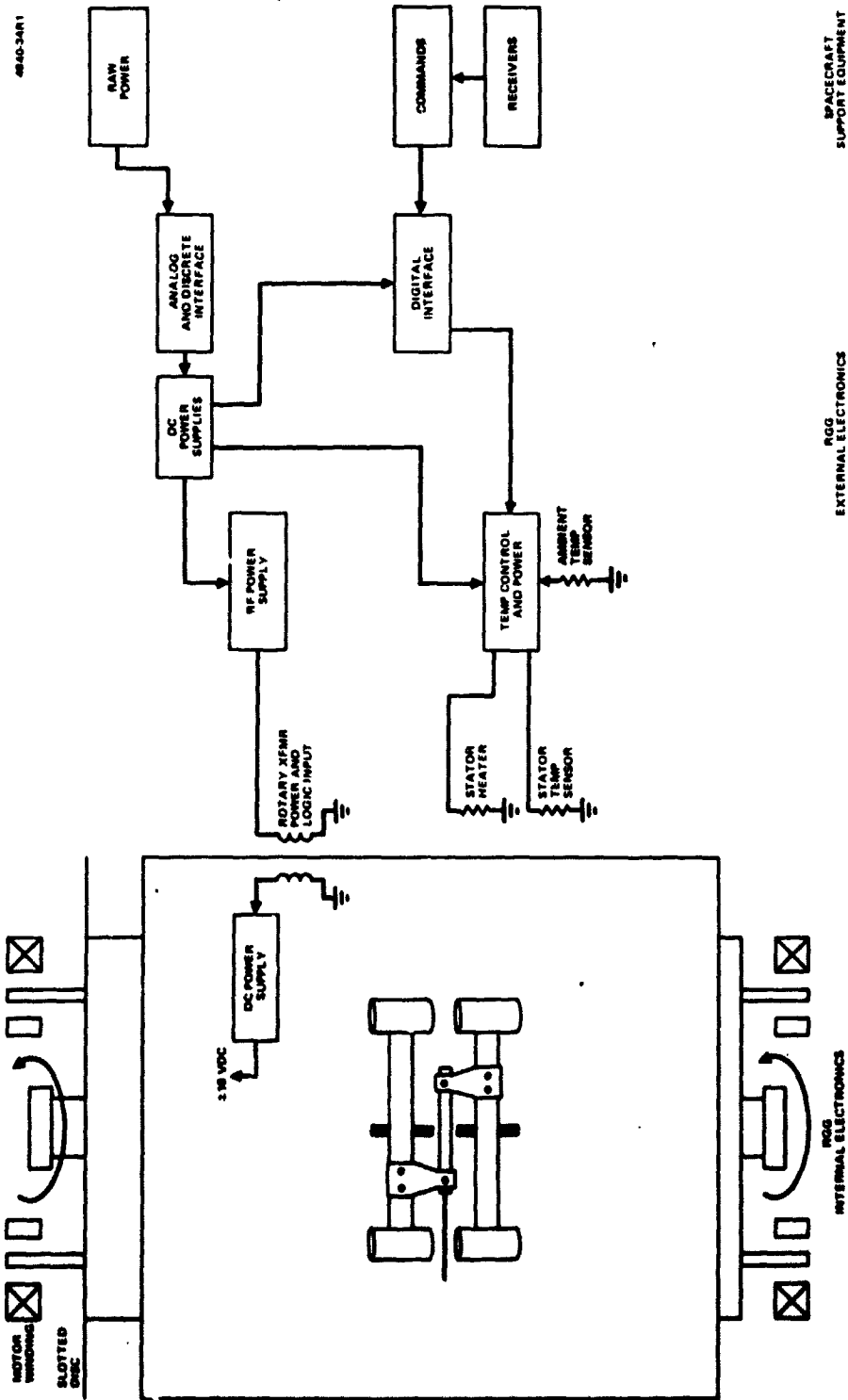
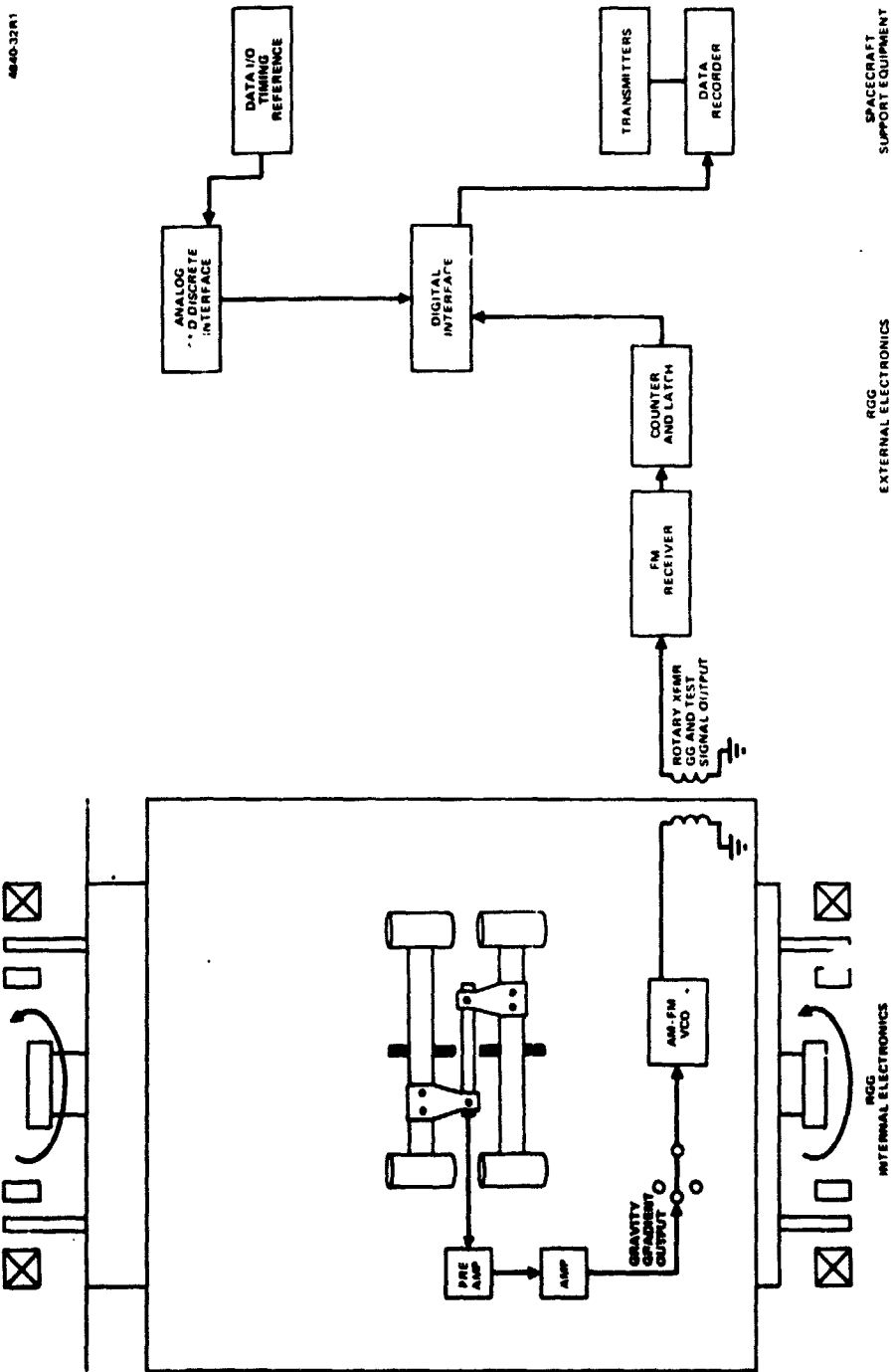


Figure 12. GEMS Power Supply and Thermal Control Electronics

ORIGINAL PAGE IS
OF POOR QUALITY



4840-32R1

Figure 13. GEMS Data Output Electronics

ORIGINAL PAGE IS
OF POOR QUALITY

The FM sensor signal from the RGG rotary transformer goes to an FM receiver, then to a zero-crossing counter and latch with a digital output which is directly related to the voltage from the piezoelectric transducer and thus directly related to the sensed gravity gradient. The counts for each octant of rotation (quadrant of space) are averaged over a selectable period, typically 64 rotations or approximately 3.6 seconds. The output is fed to the digital interface for output to the spacecraft data system.

3.3.2.4 Test and Control Electronics

GEMS test and control functions related to the RGG are illustrated in Figure 14.

(1) Logic Control: The RF power control transmitted into the rotor is interrupted in a time sequence digitally coded signal by the data injector unit. This signal is received and decoded by the interrupt detector for use in the logic control of the functions discussed in (2) through (6) below.

(2) Amplifier Gain: This logic control selection provides for normal gain or low gain of the sensor output amplifier. Low gain is used during sensor check out and test to avoid overdriving the amplifier output stages when the bias or signal level is higher than normal.

(3) Voltage Test: An accurate bridge measurement of the RGG internal raw or regulated dc voltage can be selected for output in place of the gravity gradient signal. Simultaneously, an input reference 2 w square wave voltage is switched to the voltage test bridge.

(4) Torque Test: A test and calibration torque can be applied to the RGG arms by routing of the input reference 2 w square wave to capacitor plates located near the end masses. The 2 w signal is correctly phased by the digital interface unit using the 8 w pulses from the photo pickoff unit as a reference. Because the output signal from the transducer is a sum of the gravity gradient signal and the calibration output signal produced by capacitor torquers, the same preamplifier, amplifier and output switch logic selection are used.

(5) Temperature Test: Internal RGG temperature measurements are made by logic switching of the input 2 w square wave to the temperature test bridge. This along with the input from the temperature detector produce an output which is simultaneously selected for transmission to the external electronics in place of the gravity gradient and torque signal.

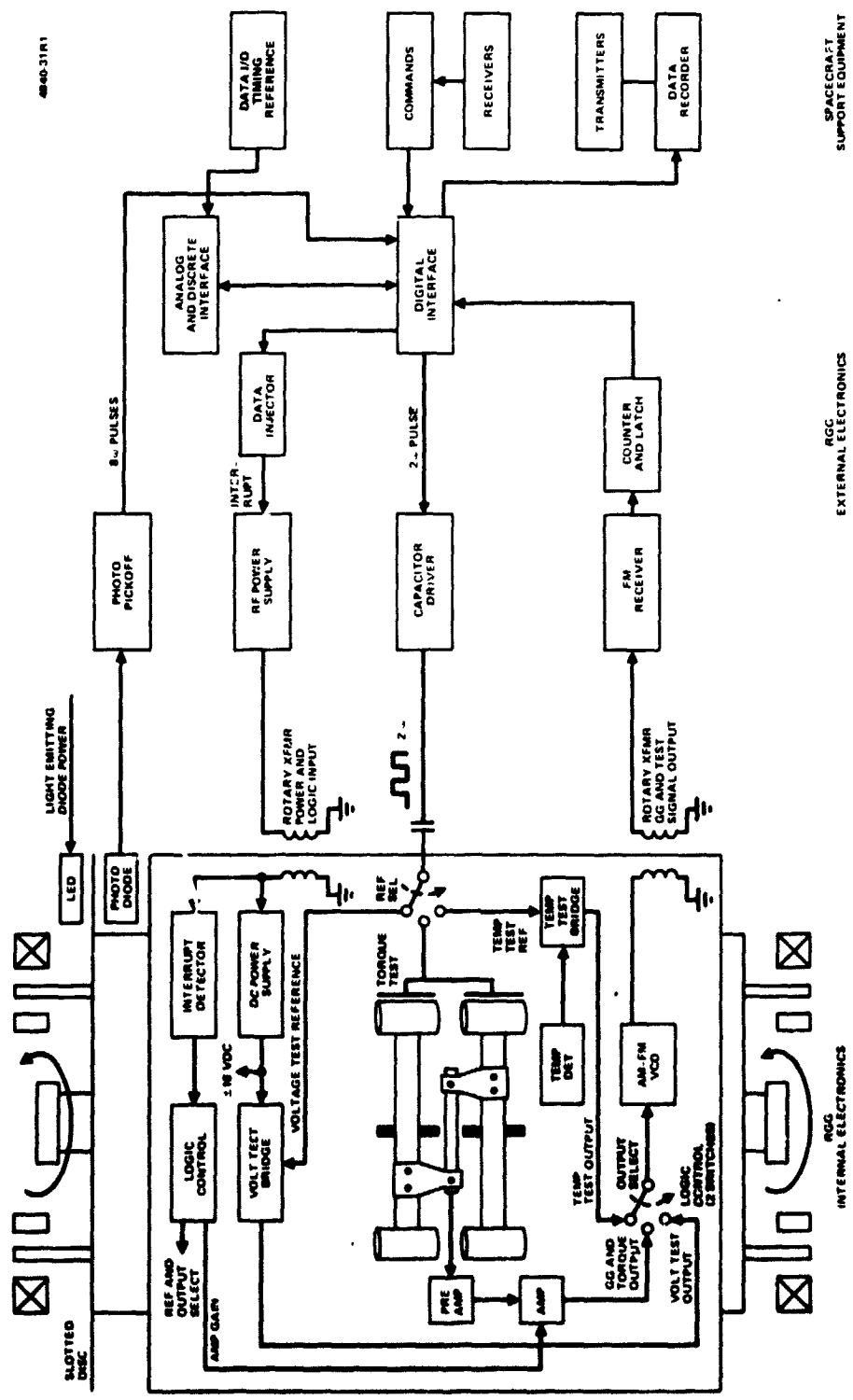


Figure 14. GEMS Test and Control Electronics

ORIGINAL PAGE IS OF POOR QUALITY

(6) GEMS Input/Output: Command data to GEMS from the S/C computer, or from earth, and science and engineering data from GEMS for storage in the S/C recorder or for transmission to earth are handled through the digital interface unit's input/output (I/O) addressable registers. Clock and sync signals for I/O timing reference are received from the S/C through the analog and discrete interface unit. I/O is discussed in greater detail in Sections 6.4 and 6.5.

3.4 Operating Modes

The GEMS operating modes are controlled by command and vary only in the characteristics of the data being acquired (science or engineering), the spin speed, sensor operating temperature, etc. Therefore, the GEMS has only three power modes: Standby (temperature stabilization); Operate; and Off.

3.5 Preliminary Space GEMS Electronics Subsystem Design

A first look at the electronics subsystem design for the LPO and other space applications was done with the primary purpose of determining interface requirements and approximate size and weight of the external electronics. It was based on the use of standard Hughes space-qualified and proven design and fabrication techniques and hardware. In the process of accomplishing this task, the functional block diagrams of Figures 15 and 16 were generated along with other information included in other parts of this report. For specific information on size, weight, power, etc, see Section 6.0.

Figure 15 shows the functional relationships of a number of electronic elements which require digital registers and the register sizes. Figure 16 shows GEMS-Spacecraft command and data interface requirement including timing and control lines.

Lists of the command, science and engineering data items with the requirements for registers (words), register sizes (bits/word) and data rates are included in Sections 6.4 and 6.5.

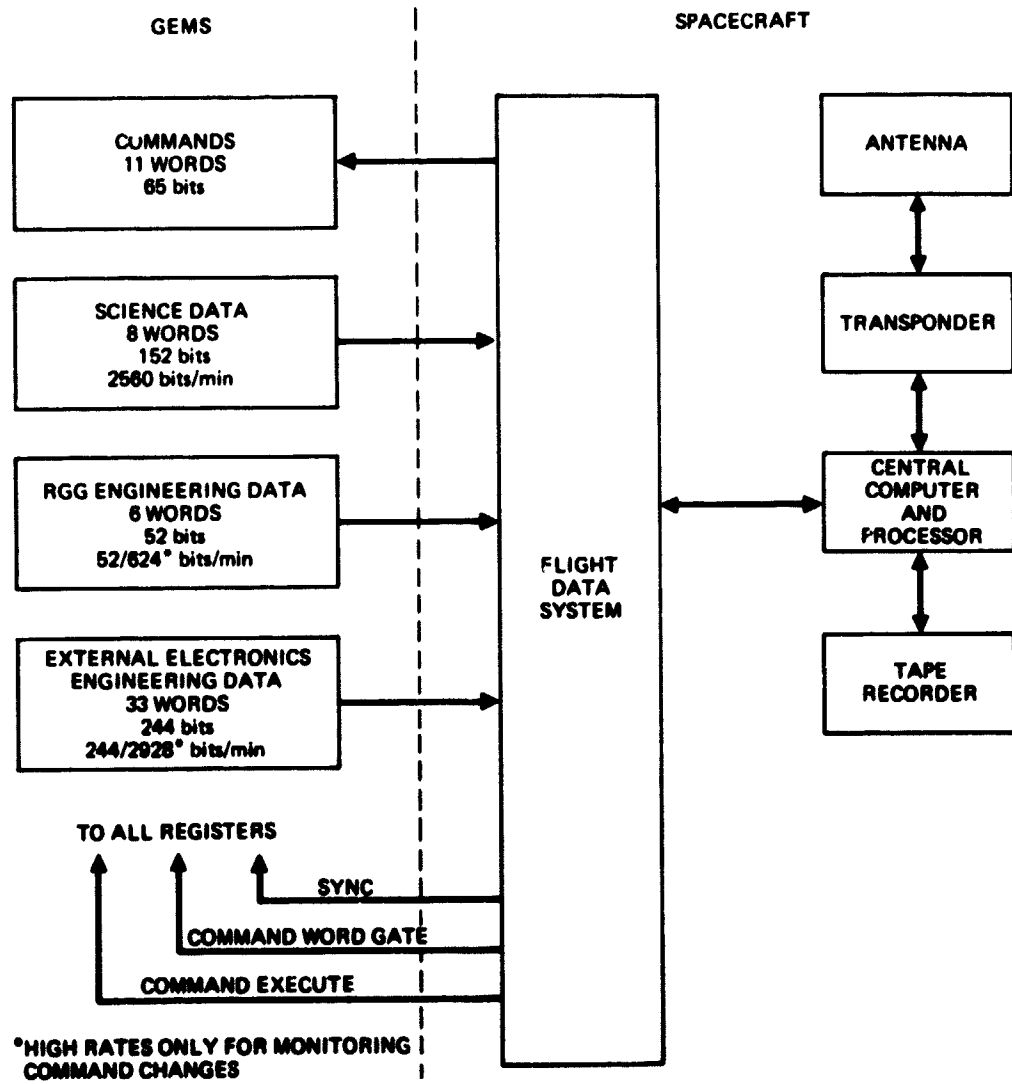


Figure 16. GEMS/Spacecraft Interface

4.0 PHYSICAL DESCRIPTION

In the discussion of GEMS above, the simplified representation of the RGG was used for ease of functional description. There are some differences between the simplified version and the actual hardware which are described in the following paragraphs.

4.1 Sensor Arms

Rather than the single "bar" type arm depicted in the functional diagrams, each sensor arm is actually a pair of arm plates with the end masses bolted between as shown in the photograph of Figure 17. This forms a rigid box structure resistant to bending under high-g shock and launch conditions. It also reduces errors due to anisotropy of the arms. Cutouts in the arm plates are made to render the arms isoelectric and minimize these errors. The arms are interleaved to get the centers of mass closer together and for better position of the torsion spring supports.

4.2 Inner Rotor Housing

The arms with their end masses are enclosed in a case comprising a circular center plate shown in Figure 17 and two end bells shown in Figure 18. The bells are bolted to the center plate and to the bases at the ends of the pivots (one of which is shown at the top of Figure 17) forming a very rugged dual box structure.

The relationship between these parts and others discussed below is shown in Figure 19.

**ORIGINAL PAGE IS
OF POOR QUALITY**

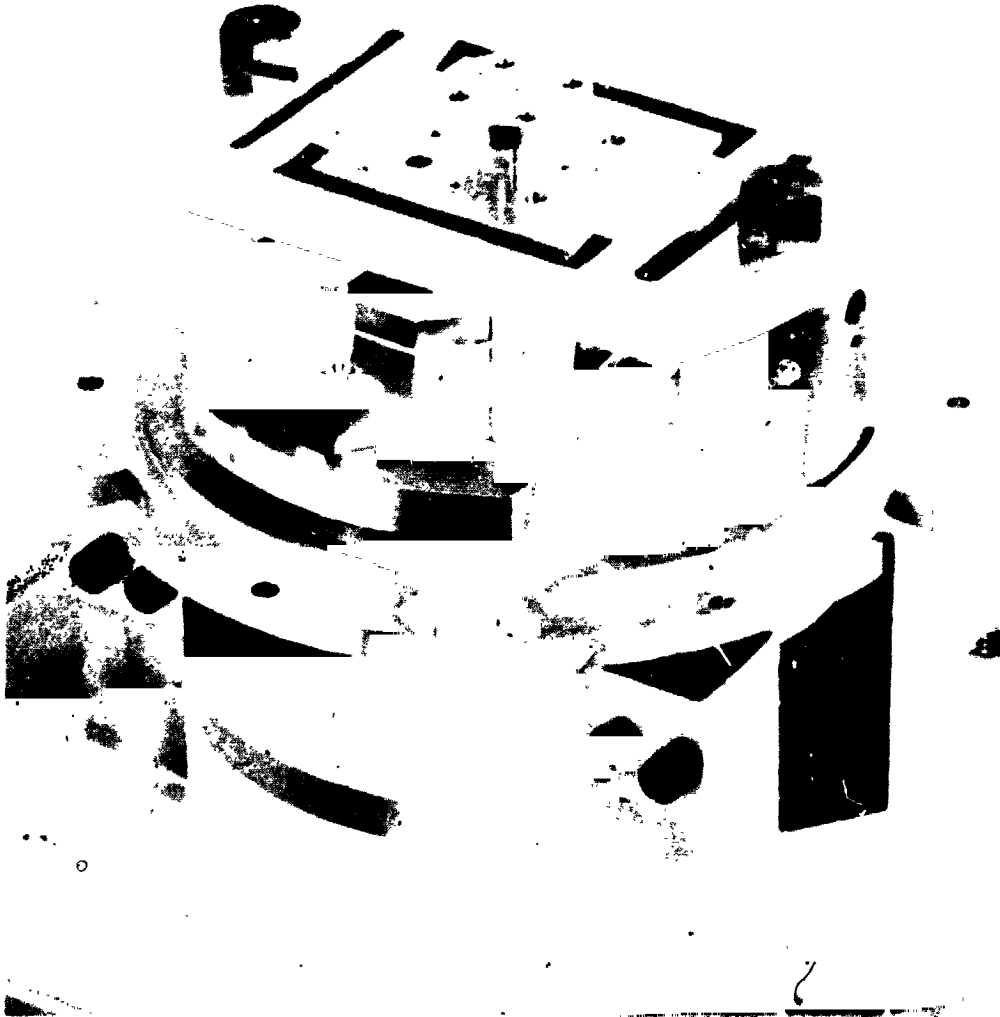


Figure 17. RGG/End Mass/Center Plate Structure

4.3 Pivot Springs

Because of the dual-plate, interleaved arm design and the center-plate, dual-bell inter rotor housing design, there are six torsional pivot springs as shown in Figure 19. Two of these are between arm plates of different arms and tend to keep the arms orthogonal but permit them to rotate slightly relative to one another. The other four pivots keep the arms fixed to the inner rotor case except for slight rotation of the arms relative to the case.

5278-21

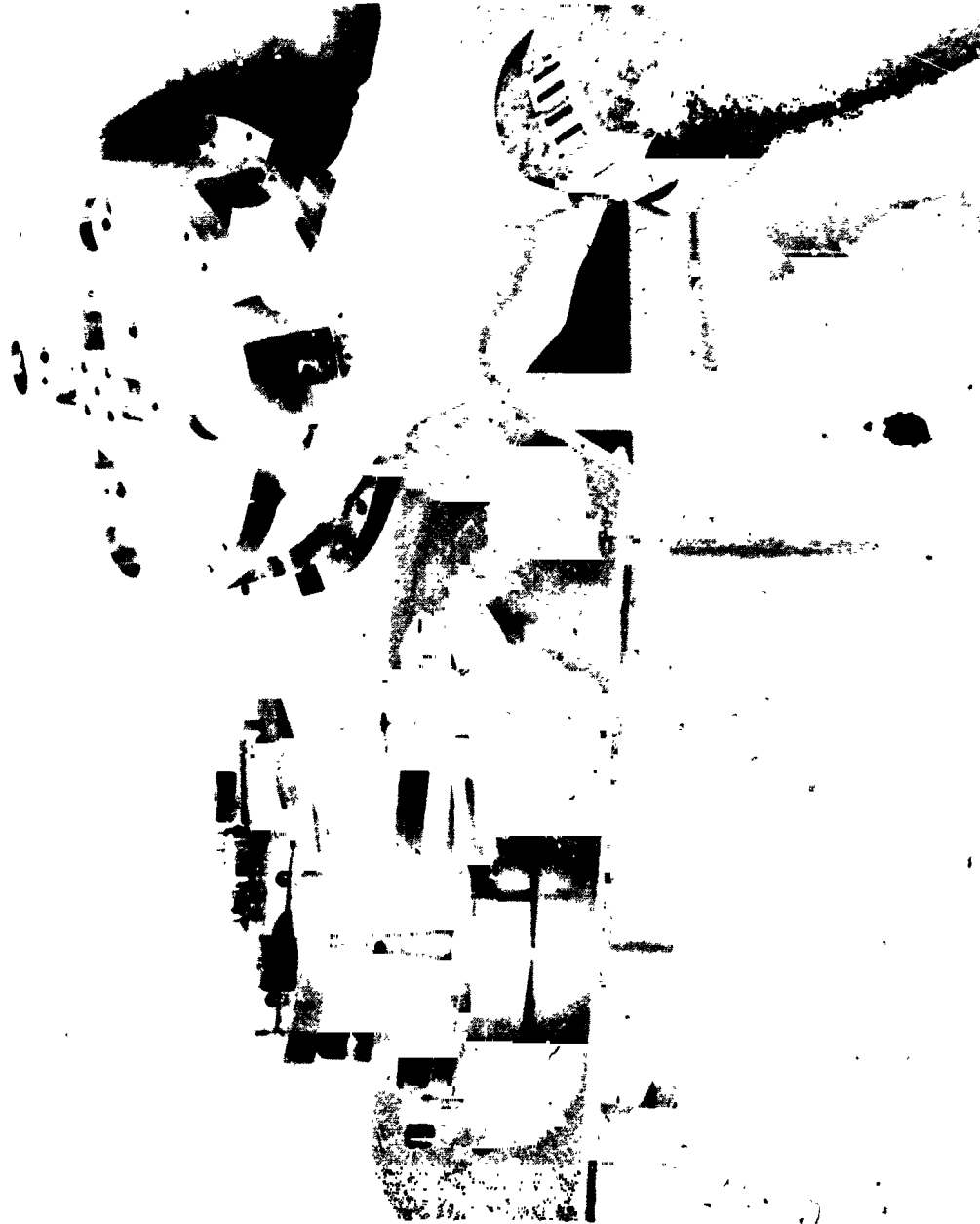


Figure 18. RGG Arm/Mass/Center-Plate Assembly with Bottom Inner Rotor Bell in Place and Top One Held

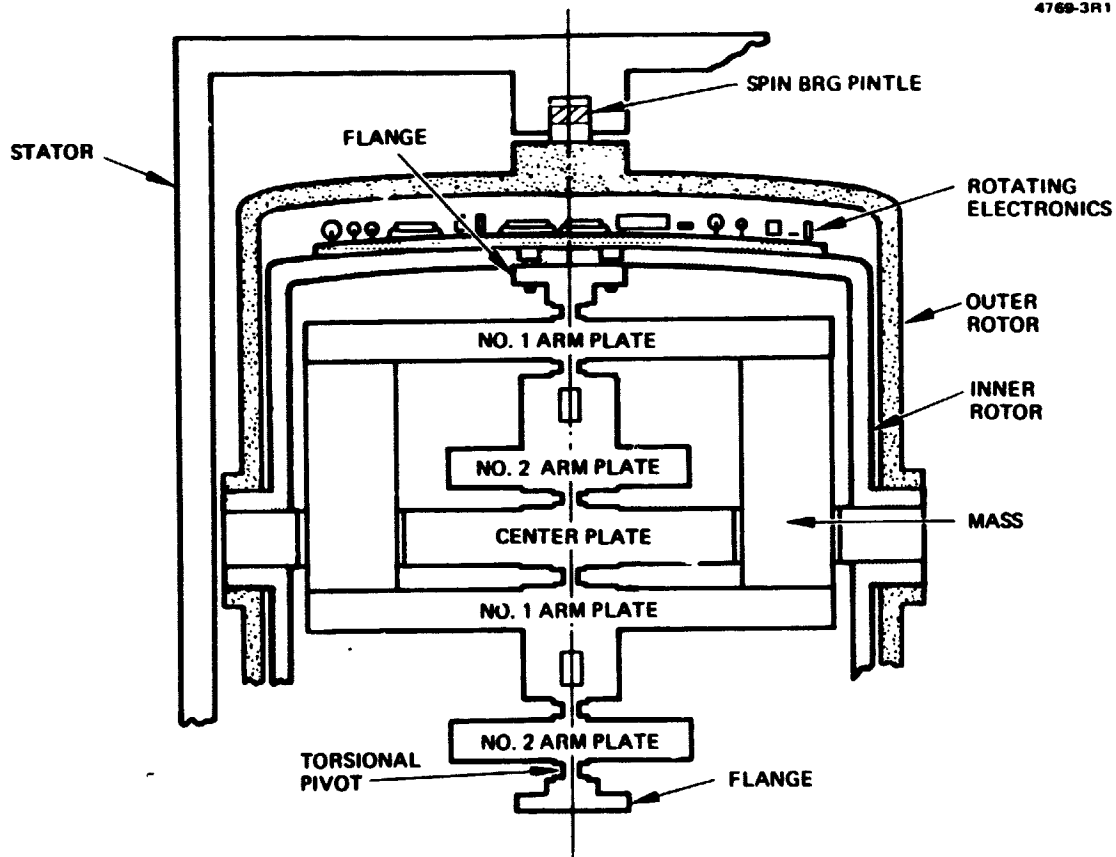


Figure 19. Relationship of RGG Structural Parts

Five of the six pivots are visible in Figure 20. They vary from about 3 to 4 mm in diameter and 2.7 to 2.8 mm in length depending on position.

4.4 Arm/Pivot/Center Plate Fabrication

All of the structure comprising the four arm plates, center plate, six pivots and two end bases are machined from a single forged aluminum billet and remain a single piece of metal throughout fabrication. This avoids a very difficult assembly

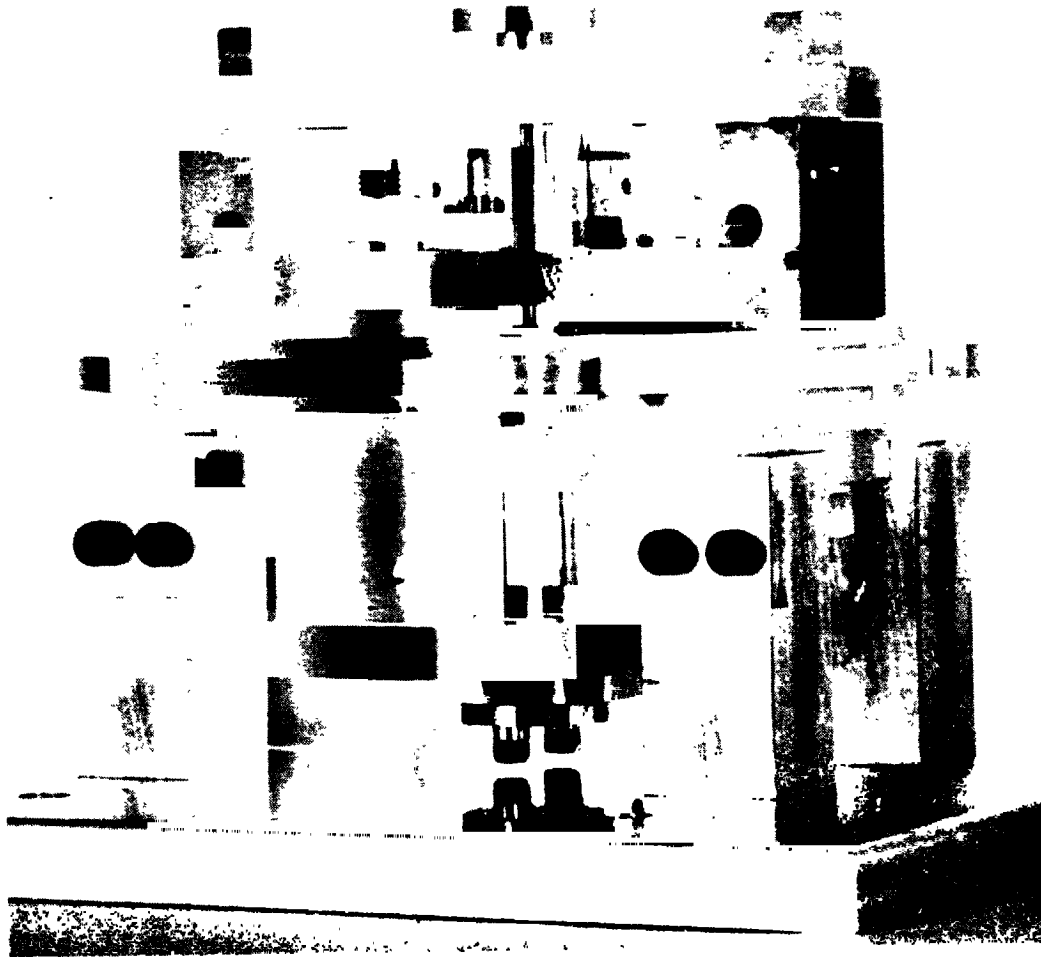


Figure 20. RGG Arm/Pivot/Center Plate and End Mass Assembly
Showing Top Five of the Six Pivots

and fastening process, which would be required if these functional elements were machined as separate pieces. Figure 21 shows a section of a forged aluminum billet at the upper right, a rough machined part at the left and a final machined part at the lower center.



Figure 21. RGG Arm/Pivot/Center-Plate Unit in Three Steps of Fabrication (see text)

4.5 Transducers

Instead of a single transducer as depicted in the functional sketches, there are two. Each one passes through a hole in an enlarged portion of the two pivot sections connecting arm plates of opposite arms. These rectangular holes are visible in Figure 20. Thus, one transducer is attached between the two upper plates and the other between the two lower plates. Relative rotation of the arms produced primarily by gravity gradients causes the transducers to bend and produce an output signal, while rotation of the arms in unison relative to the case does not bend the transducers or produce an output. Thus, vibration of the instrument caused by environmental disturbances do not produce first order errors in the output. Slight errors can be induced by coupling of the vibrations with residual imperfections in the instrument. Adjustments are provided to reduce these errors to levels below the design sensitivity of the sensor.

4.6 Outer Rotor

The inner rotor case supporting the arm/end mass/pivot structure, defines the torsional pivot axis. To minimize one of the error sources requires adjustment of the pivot axis for alignment with the rotor spin axis. Thus, an outer rotor case comprising a pair of end bells similar to the inner rotor end bells but slightly larger, are also attached at the center plate and support the rotating halves of the two bearings. The top one is diagrammed in Figure 19. The two motor drag cups and the slotted disc are also attached to the outer rotor. The RGG sensor with half of the stator removed is shown in the photograph of Figure 22. The upper half of the rotor appears protruding from the bottom half of the stator. At the top is the upper drag cup and around its base is the rotor half of the ring capacitor used to couple the 2 w square wave reference and torque driver signal to the rotor. The slotted disc shown in Figure 7 is attached to the opposite end of the rotor at the base of the second drag cup.

4.7 Stator

The outer case of the RGG, called the stator, supports the rotor by the spin bearings as shown in Figure 19. It contains the stationary parts of the two rotary transformers, the capacitance coupler and the two spin motors. It also supports the optical sensor for speed sensing and provides an air-tight chamber which is evacuated after assembly. The vacuum reduces windage on the rotor and thermal conductivity between the stator and the rotor.

5278-24



Figure 22. RGG with Half of the Stator Removed

The completely assembled prototype RGG sensor (No. 1) is shown in the photograph of Figure 2. See the first paragraph in Section 3.3.1 for further information. Heating wires and temperature sensing wires can be seen in the helical grooves on each stator half. Fins will be added to the case ends for added radiative heat dissipation in space applications. See Section 5.5 for report on the thermal control study.

4.8 Internal Electronics Packaging

The internal RGG electronics is located on two printed circuit boards one at each end of the rotor between the inner and outer rotor bells. The boards for prototype RGG No. 1 are shown in Figures 23 and 24. They are slightly saucer shaped and attached to the outside of the inner rotor as shown in Figure 19. The internal electronics circuit boards for prototype RGG No. 2 will be flat and attached to the inside of the outer rotor. This change will result in more uniform temperature of the pivots which are the most critical temperature sensitive elements in the RGG.

4.9 External Electronics Packaging

The prototype RGG external electronics comprises mostly standard laboratory electronics equipment and special units built by Hughes for laboratory testing. However, a preliminary design analysis has been made of the external electronics requirements for the LPO mission gravity experiment and other similar gravity survey space missions. This analysis indicates that the external electronics can be contained in one package 8x15x137 cm. Figure 25 is an outline and mounting drawing of the proposed package. Design and fabrication would be in accordance with standard Hughes space qualified electronics equipment, which has proven highly reliable in many space systems.



Figure 23. RGG Internal Electronics Top Circuit Board

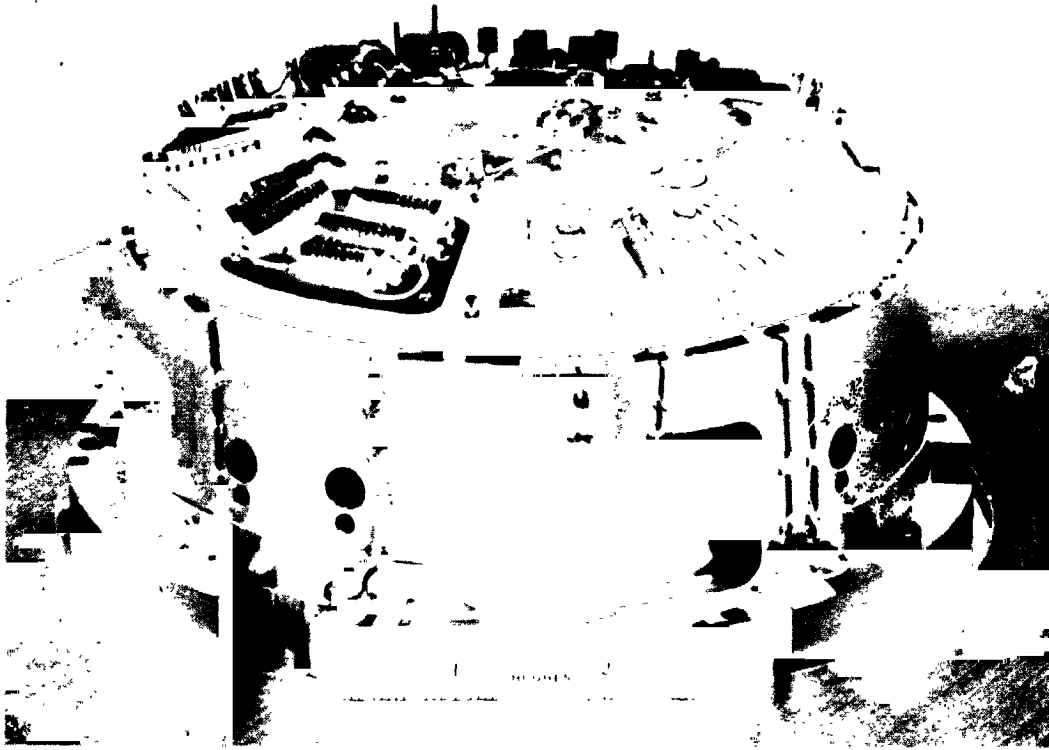


Figure 24. RGG Internal Electronics Bottom Circuit Board

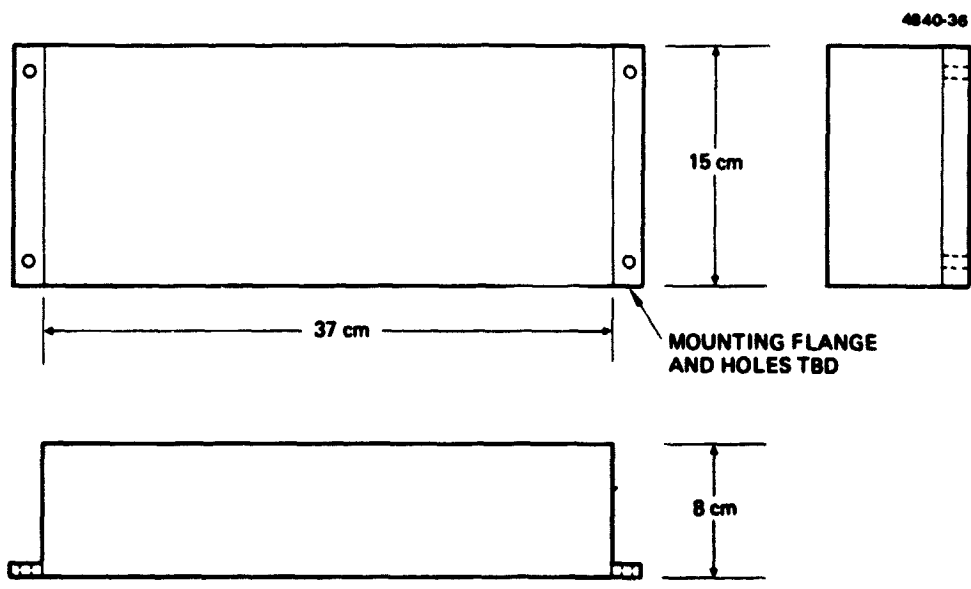


Figure 25. RGG External Electronics Unit Outline and Mounting

5.0 SPECIAL REQUIREMENTS

5.1 Sensor Location on Spacecraft

The KGG and electronics can be placed at any convenient location on the S/C. There is no requirement to locate the sensor at the S/C center-of-gravity (CG) nor to control the spacecraft CG. If the sensor is located in close proximity to either movable devices (scan platform) or expendables (fuel) these effects can be removed from the data by modeling or by disregarding the data taken during periods when large masses are moving.

One factor which may affect location of the KGG is power for thermal control. To keep this near the low end of the range, it is desirable to place the KGG in a location which has a low thermal gradient. This is discussed in detail in Section 5.5.

5.2 Sensor Alignment

The sensor spin axis alignment, both control and knowledge, is not critical. Nominal S/C alignment tolerances of 1 to 5 degrees will suffice since alignment errors only cause a nominal initial bias which will be removed from the data along with other initial biases including the S/C gravity gradient. Actual low frequency GEMS gravity data plus what is previously known about the lunar gravitational field in the low frequencies can be used to later calculate the sensor attitude with respect to the mean Lunar vertical to better than a milliradian (See Appendix D).

5.3 Sensor Attitude Control Rates

The GEMS experiment uses a "specific force" gradiometer and if the S/C is undergoing rotation, then the induced rotational velocity field produces a rotational gradient that is sensed by the gradiometer. The gradient produced by a rotational rate has an amplitude equal to the square of the rotational rate and is cylindrically uniform about the axis of rotation. The following two conditions have been considered.

(a) If the S/C is gravity gradient stabilized it is rotating about the orbit axis at a rate equal to the instantaneous orbital angular rate. There will then be a positive rotational gradient that is uniform in the plane of the orbit and whose amplitude (for a circular orbit) is identical to the negative horizontal gradient of the moon. This rotational gradient is well within the dynamic range of the sensor and together with the horizontal gravity gradient of the moon will be part of the data set that will be used to produce not only the gravity field, but also the S/C orientation and motion (See Appendix D).

(b) The gradients of the S/C attitude control system rotational rates will also be sensed. If momentum wheels are used and the rate errors are 2 microradians per second, the resulting error signal will be 0.004 Eotvos.

This error is negligible for a sensor with a sensitivity of 1 Eotvos. The uncertainties in the attitude control rate errors would have to be greater than 30 microradians per second to generate an error signal equal to the GEMS sensitivity.

5.4 Attitude Control Accelerations

The GEMS does not have first order sensitivity to S/C rotational or linear accelerations because of the common-mode rejection inherent in the design.

5.5 Sensor Thermal Control

5.5.1 Objective

A thermal control study was conducted to determine the feasibility of maintaining RGG case temperature time gradient (rate of change) within ± 0.06 C/hr for a range of assumed S/C environmental temperatures, and temperature time gradients.

5.5.2 Assumptions

The assumed S/C environmental temperature and time gradient ranges for operation of the RGG within specification were 0 to 55 C and 3 C/hr to 20 C/hr, respectively. In addition to the above assumptions, the orbit time was assumed to be 105 minutes and the worst case of 12 W internal RGG power dissipation was used.

5.5.3 Preliminary Analysis

A first look at the RGG temperature-control heater-power requirements indicated that the worst case boundary conditions are: (a) maximum ambient temperature range, (b) maximum environmental temperature rate of change, and (c) an orbit with a S/C sunlit-to-shadow ratio of one.

The RGG nominal operating (case) temperature can be shifted periodically to maintain it at or slightly above the peak S/C ambient temperature. It is feasible to do this by program or command control. Thus, long term shifts in S/C ambient temperature as might be caused by shifts in the sun/shadow ratio or failure in S/C thermal control systems would not significantly increase RGG heater power requirements.

5.5.4 Thermal Design Approach

The required thermal control of the RGG can be achieved by utilizing conventional thermal control techniques. Conduction isolation (conductivity less than 0.5) will be employed to minimize conduction effects of the S/C environment. High emittance thermal finish (emissivity greater than 0.85) is required to reject the 12 W internal dissipation of the unit while maintaining case temperatures below 61 C. These passive techniques will be utilized in conjunction with proportionally controlled heaters to null out case transient temperature variations.

The combination of 12 watts internal dissipation and +.06 C/hour temperature stability requirement greatly influenced the thermal design of the unit. The present 0.18 square meter radiative surface area has to be approximately doubled to prevent the RGG bulk temperature from exceeding 61 C when exposed to the S/C maximum environmental temperature of 55 C. The required increase in radiative surface area may be accomplished by addition of fins to the ends of the RGG unit.

For the final analysis, four maximum S/C environmental temperatures were selected: 55, 45, 30 and 15 C. The first represents the worst case maximum temperature at which the RGG must operate within specification. This is also the upper limit for the RGG, because of the temperature rise within the unit and the temperature limits of the Mil-Spec electronic components. The last is the lowest anticipated orbit-maximum S/C environmental operating temperature. The others are convenient intermediate values. Three values of temperature time gradient were used in the analysis: 3, 11, and 20 C/hour. Other factors used have been stated above. It should be emphasized that these include the worst case values for RGG internal power dissipation and sunlit-to-shadow ratio.

5.5.5 Results

The results of the thermal analysis are listed in Table 1. The first two columns are the selected parametric values for temperature rate of change and maximum environmental temperature. The third column contains the calculated values of minimum environmental temperature. The fourth column in Table 1 shows the calculated values of RGG bulk temperature, and the last two columns list the maximum and average heater power required for each combination of parametric conditions.

The results are plotted in Figures 26 and 27. Figure 26 shows the variation in S/C internal environmental temperature over the orbit period for each combination of parametric values. Figure 27 shows the variations in required average and peak

Table 1. RGG Thermal Analysis Results

5278 9

$ \Delta T/\Delta \theta _E$ (°C/hr)	ENVIRONMENTAL TEMP, °C		RGG BULK TEMP, °C	HEATER POWER, W	
	MAX	MIN		MAX	AVG
3	15	12.4	22.3	4.0	2.0
	30	27.4	37.8	5.0	2.5
	45	42.4	51.0	5.3	2.7
	55	52.4	60.2	5.6	2.8
11	15	5.4	22.3	13.8	6.9
	30	20.4	37.8	17.5	8.8
	45	35.4	51.0	18.8	9.4
	55	45.4	60.2	20.3	10.2
20	15	-2.5	22.3	23.9	12.0
	30	12.5	37.8	30.2	15.1
	45	27.5	51.0	32.5	16.3
	55	37.5	60.2	35.2	17.6

NOTES:

1. $|\Delta T/\Delta \theta|_E$ = RATE OF CHANGE OF ENVIRONMENTAL TEMPERATURE
2. ORBITAL PERIOD = 105 min
3. RGG RADIATIVE SURFACE AREA = 0.36 m²
4. RGG INTERNAL POWER DISSIPATION = 12.0 W
5. CONDUCTANCE FROM RGG TO S/C = 0.5 W/°C

heater power over the range of maximum S/C internal environmental temperatures selected and for each selected value of temperature rate of change. Corresponding RGG bulk temperatures can also be read from the same curves using the upper abscissa scale. The peak power requirement occurs at the minimum S/C temperature and heater power decreases to zero at the maximum S/C temperature. The average power required is one half of the peak power.

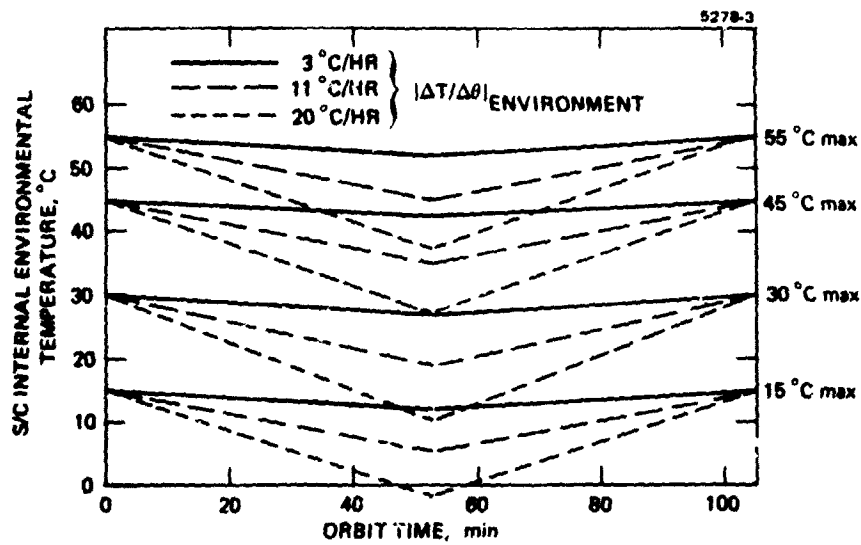


Figure 26. Spacecraft Internal Environmental Temperature vs Orbit Time

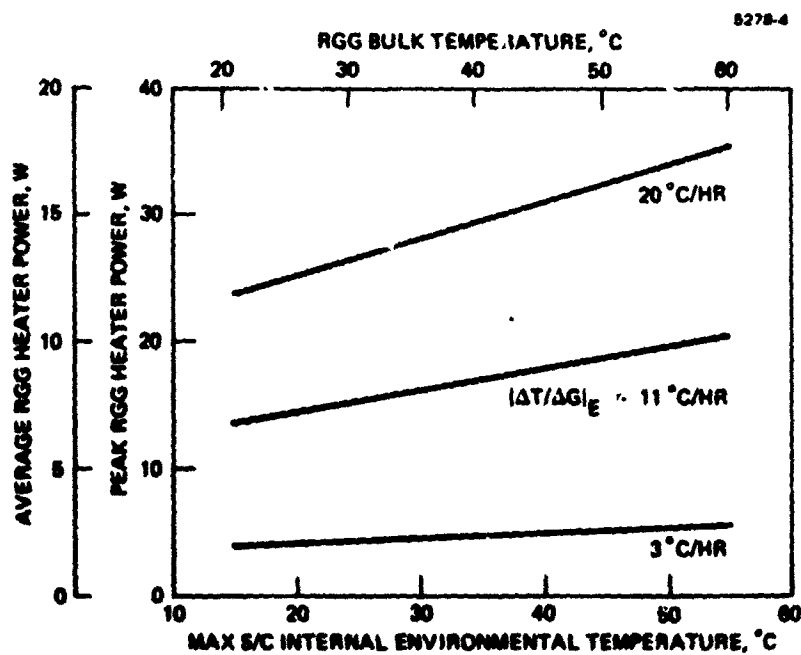


Figure 27. RGG Bulk Temperature and Heater Power vs Maximum S/C Internal Environmental Temp and Temperature Change Rate

From the table and the curves it is seen that most significant factor dictating the heater power required to null out bulk case temperature variations is the S/C environment temperature change rate. Average (over one orbit) heater power consumption ranges from 2 to 2.8 W for a 3 C/hr change rate, 6.9 to 10.2 W for an 11 C/hr rate and 12.0 to 17.6 W for a 20 C/hour rate.

5.5.6 Conclusions

Thermal control of the RGG to maintain case temperature within ± 0.06 C is feasible with a radiation dominated design, utilizing proportional controlled heaters to null out S/C internal environmental temperature changes. Location of the RGG in a region not likely to have high environmental temperature change rates is recommended to minimize heater power consumption.

5.6 Sensor Dynamic Characteristics

The RGG instrument has a significant amount of angular momentum (30 million gm-cm squared/second), but due to the speed control of one part in 10 million, this should not disturb the S/C attitude. A brief consideration of the momentum effect on attitude change control indicates that there will be no increase in thrust requirement, if the RGG momentum is taken into account in the attitude control equations and mechanization. Further study is required to fully evaluate momentum effects.

6.0 INTERFACE DEFINITIONS

6.1 Mechanical/Weight/Volume

(a) Sensor Mechanical: The mechanical configuration of the RGG sensor is shown in Figure 2. While the exact interface will be a function of the S/C, the unit can be mounted using the existing center flange. The addition of radiation fins as discussed in Section 5.5 will increase the length slightly. Nominal S/C alignment accuracy is adequate (see Section 5.2).

(b) Electronics Mechanical: The configuration of the external electronics package for one RGG sensor is shown in the layout and mounting drawing of Figure 25. The case, except for the cover, and the structure for supporting the electronic subassemblies are machined from a single aluminum casting. This produces a very rugged unit and also serves as a good heat conductor between the electronics and the S/C structure.

(c) Sensor Weight: The RGG sensor including its internal electronics weighs approximately 16 Kg.

(d) Electronics Weight: The external electronics for one RGG sensor will weigh about 3 Kg.

(e) Sensor Volume: The sensor is approximately 30 cm long by 23 cm in diameter.

(f) Electronics Volume: The electronics unit is 37x15x8 cm.

6.2 Thermal

(a) Sensor: The RGG will have its own thermal system to control temperature to within ± 0.06 C of the nominal operating temperature set by command signal. This control will be effective over a spacecraft environmental temperature range from below 0 C to 55 C, and for temperature rates of change up to 20 C/hr. The cost of wide and rapid temperature changes, however, is the requirement for increased heater power to maintain the RGG case temperature within the ± 0.06 C tolerance. This power requirement will be kept within bounds by occasionally changing the nominal RGG temperature operating point automatically or by command as the S/C interior environmental temperature changes due to changes in the sun/shade ratio or other factors. Spin speed must be changed when the nominal temperature operating point is changed. The heater power requirement can be reduced to a very nominal value of 2 to 3 watts average by locating the RGG in an area of the S/C which has a low temperature rate of change. The sensor-to-spacecraft

thermal conductivity will be approximately 0.5 W/C. The thermal study results are discussed in more detail in Section 5.5.

(b) Electronics: The Hughes standard space-qualified electronics design and fabrication techniques allow operation within specification over a range of -7 C to 55 C and survival without damage over a range of -40 C to 71 C. Thermal conductivity between the external electronics unit and the S/C is made as low as practicable.

(c) Thermal Power:

RGG: 6 to 12 W (Probably near 6 W)

External Electronics: 6 W

Heater: 2 to 18 W avg (See (a) above and Section 5.5)

6.3 Power

The GEMS for space applications operates from raw 28vdc power with power switching provided by the S/C. Total consumption is between 14 and 36 W average over one orbit, or between 16 and 54 W peak at the coldest period in the orbit. Both ranges are calculated using worst case conditions. The actual power in each case will depend on changes expected to be made in the spin motors (-6 W) and primarily on location of the RGG in the S/C, effecting temperature rate of change and thus heater power (See Section 6.2 (a) above and Section 5.5). No pulsed power modes are used.

6.4 Command

Command Requirements for GEMS are listed in Table 2.

6.5 Data

Following are data register and data rate requirements for GEMS.

(a) Science Data: Table 3. The output science data should be identified with the lunar surface position over which it was gathered to an accuracy equal to 0.1 to 0.3 times the S/C nominal altitude above the lunar surface.

(b) RGG Engineering Data: Table 4.

(c) External Electronics Engineering Data: Table 5.

Table 2. Command Words

5278-14

ITEM NO.	COMMAND DATA ITEM	WORDS	BITS
1	MOTOR SPEED (PRESET OCTANT COUNT)	1	17
2	MOTOR SPEED VARIATION LIMIT	1	8
3	MOTOR STOP	1	1
4	MOTOR DRIVE SERVO VELOCITY GAIN	1	10
5	MOTOR DRIVE SERVO PHASE GAIN	1	10
6	NOMINAL RGG OPERATING TEMPERATURE	1	7
7	RGG TEMPERATURE TOLERANCE LIMIT	1	4
8	RGG DATA READ	1	2
9	CAPACITOR DRIVER	1	1
10	RGG MODE CONTROL	1	4
11	ENGINEERING DATA RATE	1	1
	TOTAL	11	65

Table 3. Science Data

5278-15

ITEM NO.	SCIENCE DATA ITEM	WORDS	BITS PER WORD	DATA RATE	
				WORDS/MIN	BITS/MIN
1	GRAVITY GRADIENT MEASUREMENTS: EIGHT "OCTANT COUNTS" OF 10 MHz REFERENCE CLOCK (MAY INCLUDE TEST REFERENCE TORQUE)	8	$8 \times 20^{[1]}$	8×16	160×16
	TOTAL	8	152 (bits)	128	2560

[1] TWENTY BITS INCLUDES 19 BITS FOR GRAVITY GRADIENT DATA AND 1 BIT FOR WIDE SLOT MARKER (PHASE REFERENCE).

Table 4. RGG Engineering Data

5278-16

ITEM NO.	RGG ENGINEERING DATA ITEM	WORDS	BITS PER WORD	DATA RATE	
				WORDS/MIN	BITS/MIN
1	UNREGULATED VOLTAGE	1	8	1/12 ^[2]	8/96
2	REGULATED VOLTAGE	1	8	1/12	8/96
3	RF VOLTAGE	1	8	1/12	8/96
4	TEMPERATURE SENSOR NO. 1	1	10	1/12	10/120
5	TEMPERATURE SENSOR NO.2	1	10	1/12	10/120
6	REFERENCE TWO-OMEGA SQUARE WAVE VOLTAGE	1	8	1/12	8/96
	TOTAL	6	52 (bits)	6/72	52/624

[2] THE NORMAL RATE OF 1 WORD PER MIN IS MORE THAN ADEQUATE, EXCEPT WHEN MONITORING CHANGES IN OPERATING PARAMETERS DURING AND IMMEDIATELY AFTER OPERATIONAL COMMAND INPUTS. THEN A RATE OF AT LEAST 12 WORDS PER MIN IS DESIRABLE.

Table 5. External Electronics Engineering Data

5278 17

ITEM NO.	EXTERNAL ELECTRONICS ENGINEERING DATA ITEM	WORDS	BITS PER WORD	DATA RATE	
				WORDS/MIN	BITS/MIN
1	REFERENCE 2 ω SQUARE WAVE VOLTAGE	1	8	1/12 ^[3]	8/96
2	FOUR POWER SUPPLY VOLTAGES	4	8	4 x (1/12)	4 x (8/96)
3	MOTOR CONTROL FIELD	1	8	1/12	8/96
4	MOTOR REFERENCE FIELD	1	8	1/12	8/96
5	MOTOR SPEED ERROR	1	1	1/12	1/12
6	MOTOR STOP	1	1	1/12	1/12
7	WIDE SLOT MARKER FAIL	1	1	1/12	1/12
8	VELOCITY ERROR (8 QUADRANTS)	8	5	8 x (1/12)	8 x (5/60)
9	FM SIGNAL LEVEL	1	8	1/12	8/96
10	Ki DATA	8	12	8 x (1/12)	8 x (12/144)
11	STATOR TEMPERATURE	1	10	1/12	10/120
12	AMBIENT TEMPERATURE	1	10	1/12	10/120
13	STATOR TEMPERATURE ERROR	1	1	1/12	1/12
14	HEATER CURRENT	1	8	1/12	8/96
15	RGG LOGIC CODE	1	4	1/12	4/48
16	PHOTO PICKOFF SIGNAL	1	8	1/12	8/96
	TOTAL	33	244 (bits)	33/396	244/2928

[3] (SEE FOOTNOTE OF TABLE 3)

7.0 PERFORMANCE PARAMETERS

7.1 Sensitivity

The GEMS has a design sensitivity of 1 Eotvos for a 10 second integration period.

7.2 Dynamic Range

The GEMS is capable of operating over a gravity gradient range of +50,000 Eotvos to -50,000 Eotvos.

7.3 Quantization

By using the highly accurate digital speed control servo in each RGG to demodulate and digitize the analog sensor output, the GEMS converts the gravity gradient signal to a digital word with a precision of 0.2 Eotvos (19 bits).

7.4 Alignment

The RGG does not need to be accurately aligned, because ground data processing of GEMS data results in a knowledge of alignment with respect to local vertical of ± 0.001 radian.

7.5 Spin Speed

The nominal spin speed of the RGG is 1050 rpm (17.5 rps) with the capability to control the speed at a commanded value from 500 rpm (0 rpm with design modification) to 1500 rpm.

7.6 Spin Speed Accuracy

The RGG spin speed is controlled to an accuracy of one part in 10 million. The short term noise is less than 20 microradians and the long term phase stability is better than one part in 1 billion. See Section 3.3.2 for details on the RGG spin speed control.

7.7 Temperature

RGG bulk (case) temperature is maintained within ± 0.06 C about a commanded case operating temperature which is set at or slightly above the sensed S/C maximum internal environmental temperature at the location of the RGG. See Section 5.5 for details on the RGG thermal control.

7.8 Sensitivity to Spurious External Fields

The RGG is fabricated from non-magnetic materials to avoid magnetic field error sensitivity. In the original design, an inadvertent closed loop conductive path through each set of arm plates and end masses has resulted in a higher magnetic field error sensitivity than was expected. RGG prototype No. 1 has a magnetic field error sensitivity of approximately 20,000 Eotvos per Gauss squared. A design modification has already been incorporated in RGG No. 2 to break the closed conductive path. It is anticipated that this will reduce the magnetic field error sensitivity by the required amount. There will still remain an eddy current effect which is difficult to calculate. If the sensitivity is still above the level of 1000 Eotvos per Gauss squared, and if the sensor could be subject to magnetic field variations greater than 0.01 Gauss from other equipment in the spacecraft, magnetic shielding will be used. This has been proven in the laboratory to be completely successful in reducing the error to acceptable limits, even with RGG No. 1's high magnetic field error sensitivity and operating in the earth's magnetic field. Thus, magnetic field error sensitivity will not be a problem in the LPO application.

The RGG is not sensitive to electrostatic fields nor to nuclear radiation. Sensitivity to mass shifts in the S/C can be minimized by locating the RGG away from large moving masses such as platforms, neglecting the gravity gradient data during periods of large mass shifts, if infrequent or short in duration, or by compensating for the shifts in the data if needed.

The external electronics has the same degree of sensitivity to nuclear radiation as conventional space-qualified analog and digital circuitry. Hardened devices and design techniques can be used if required.

7.9 Generation of Interference Fields

The RGG does not utilize nor produce nuclear radiation. It produces only the normal electromagnetic fields produced by current flow in cables external to the RGG housing and electronics unit enclosure. These can be minimized by proper design and cable shielding.

The radio frequency (RF) link is between the RGG rotor and stator and thus is totally inclosed within the RGG metal housing (stator) which does not leak RF. Therefore, the RF link does not produce radio frequency interference (RFI) external to the RGG. Even within the RGG the RF link produces no significant effect on the internal electronics circuitry including the low level preamplifier for the sensor signal from the piezoelectric transducer.

8.0 SAFETY

There are no high voltages, radioactive materials or other hazardous items in GEMS.

The RGG is designed to withstand up to 50 g shock loads in the radial direction (perpendicular to the spin axis) and up to 100 g in the longitudinal direction (parallel with the spin axis) under non-operating conditions (for ground handling and launch). These factors can be increased, if necessary, by making a minor design change.

No problems are anticipated in operating the GEMS in the very benign space environment as it was designed for operation in aircraft and other vehicles with more severe environments.

9.0 MISSION

(TBC)

APPENDIX C

LPOSIM FORTRAN PROGRAM

SIMULATES A LUNAR POLAR ORBITER GRAVITY GRADIENT EXPERIMENT

```

C
C LPOSIM.FOR
C
C SIMULATES LUNAR POLAR ORBITER GRAVITY GRADIENT EXPERIMENT
C
C 30 JUNE 1976 VERSION
C
C DR. ROBERT L. FORWARD, SENIOR SCIENTIST
C HUGHES RESEARCH LABS, 3011 MALIBU CANYON RD., MALIBU, CA 90265
C (213)456-6411
C
C CALCULATES THE VARIOUS GRAVITY GRADIENTS AND COMBINATIONS OF
C GRAVITY GRADIENTS TO BE EXPECTED ON THE LPO. THE LPO IS IN A
C SIMPLE ELLIPTICAL ORBIT ABOUT A SPHERICAL, INERTIALLY ROTATING,
C BUT NON-TRANSLATING MOON.
C THE MOON HAS VARIOUS MASCONS ON IT THAT ARE MOVED UNDER THE LPO
C ORBIT AS THE MOON ROTATES.
C
C DIMENSION THE MASS POINT SET AND OPEN DATA STORAGE FILES.
C
C     IMPLICIT DOUBLE PRECISION (A-H,O-Z)
C     DIMENSION AM(20),XM(20),YM(20),ZM(20)
C
C     OPEN(UNIT=20,FILE='GVV.DAT')
C     OPEN(UNIT=21,FILE='GAA.DAT')
C     OPEN(UNIT=22,FILE='GCC.DAT')
C     OPEN(UNIT=23,FILE='GVA.DAT')
C     OPEN(UNIT=24,FILE='GAC.DAT')
C     OPEN(UNIT=25,DEVICE='DSK',FILE='GCV.DAT')
C     OPEN(UNIT=26,DEVICE='DSK',FILE='GVMA.DAT')
C     OPEN(UNIT=27,DEVICE='DSK',FILE='GAMC.DAT')
C     OPEN(UNIT=28,DEVICE='DSK',FILE='GCMV.DAT')
C     OPEN(UNIT=29,DEVICE='DSK',FILE='GTRA.DAT')
C     OPEN(UNIT=30,DEVICE='DSK',FILE='ALT.DAT')
C     OPEN(UNIT=31,DEVICE='DSK',FILE='TIME.DAT')
C
C SET UP CONSTANTS.
C     G = GRAVITATIONAL CONSTANT IN KM^3/KG*SEC^2
C     A = LUNAR RADIUS IN KM
C     AM,X,Y,Z = MASS AND POSITION OF MOON
C     WL= LUNAR SIDEREAL ROTATION IN RAD/SEC
C
C     PI=3.1415926
C     G=6.67E-20
C     A=1737.9
C     AM(1)=7.349E+22
C     XM(1)=0
C     YM(1)=0
C     ZM(1)=0
C     WL=2.6618E-6

```

```

C
C SET UP ORBITAL PARAMETERS FOR SPACECRAFT
C   E = ORBITAL ECCENTRICITY
C   H = MINIMUM ORBITAL ALTITUDE IN KM (PERILUNE)
C   P = SPACECRAFT ANGULAR MOMENTUM IN KG*KM^2/SEC
C   RP = RADIUS CONSTANT IN ORBITAL EQUATION IN KM
C   TH0= INITIAL ANGLE FOR ORBIT IN RAD
C
C   E=0.0000
C   TH0=-0.25*PI
C   H=60.
C   RP=(A+H)*(1+E)
C   P=SQRT(G*AM(1)*RP)
C
C START SPACECRAFT ORBITING MOON
C   TH = SPACECRAFT ANGLE ALONG ORBIT IN RAD
C   DT = TIME INCREMENT IN SEC
C   RS = SPACECRAFT RADIUS FROM LUNAR CENTER IN KM
C   ALT= SPACECRAFT ALTITUDE IN KM
C   WS = SPACECRAFT INERTIAL ANGULAR RATE IN RAD/SEC
C   XS,YS,ZS = SPACECRAFT POSITION IN KM
C
C   TH=TH0
C   DT=10
C   DO 10 T=-24000,24000,DT
C   RS=RP/(1+E*COS(TH))
C   ALT=RS-A
C   WS=P/(RS*RS)
C   XS=RS*COS(TH)
C   YS=0
C   ZS=RS*SIN(TH)
C
C GENERATE MASS POINT SET
C   AM(I) = MASS OF Ith MASS POINT
C   XM(I),YM(I),ZM(I) = POSITION OF MASS POINT IN INERTIAL FRAME
C
C SPACE THEM 2 DEG = 0.035 RAD APART
C   CD=COS(0.035)
C   SD=SIN(0.035)
C
C AND MOVE THEM AROUND WITH THE LUNAR ROTATION.
C   CWLT=COS(WL*T)
C   SWLT=SIN(WL*T)

```

C
 C MASCON DIRECTLY ALONG X AXIS
 AM(2)=5.0E+16
 XM(2)=A*CWLT
 YM(2)=A*SWLT
 ZM(2)=0
 C MASCON ON EQUATOR-WEST OF #2
 AM(3)=0
 XM(3)=A*CD*CWLT+A*SD*SWLT
 YM(3)=-A*SD*CWLT+A*CD*SWLT
 ZM(3)=0
 C MASCON BELOW #2
 AM(4)=5.0E+16
 XM(4)=A*CD*CWLT
 YM(4)=A*CD*SWLT
 ZM(4)=-A*SD
 C MASCON ALONG -X AXIS (FARSIDE)
 AM(5)=5.0E+16
 XM(5)=-A*CWLT
 YM(5)=-A*SWLT
 ZM(5)=0
 C MASCON ON EQUATOR-WEST OF #4
 AM(6)=5.0E+16
 XM(6)=-A*CD*CWLT-A*SD*SWLT
 YM(6)=-A*CD*SWLT+A*SD*CWLT
 ZM(6)=0
 C MASCON BELOW #4
 AM(7)=0
 XM(7)=-A*CD*CWLT
 YM(7)=-A*CD*SWLT
 ZM(7)=A*SD
 C MASCON LUNAR NORTH POLE
 AM(8)=5.0E+16
 XM(8)=0
 YM(8)=0
 ZM(8)=A
 C MASCON SOUTH OF #8 TOWARD #2
 AM(9)=0
 XM(9)=A*SD*CWLT
 YM(9)=A*SD*SWLT
 ZM(9)=A*CD

C
C CALCULATE TOTAL GRAVITY GRADIENT OF ENTIRE MASS POINT SET
C IN INERTIAL REFERENCE FRAME.
C

```
GXX=0
GYY=0
GZZ=0
GXY=0
GYZ=0
GZX=0
DO 20 I=1,9
GM=G*AM(I)
X=XM(I)-XS
Y=YM(I)-YS
Z=ZM(I)-ZS
R=SQRT(X*X+Y*Y+Z*Z)
GRR=GM/(R*R*R)
GXX=GXX+GRR*(-1+3*X*X/(R*R))
GYY=GYY+GRR*(-1+3*Y*Y/(R*R))
GZZ=GZZ+GRR*(2-3*(X*X+Y*Y)/(R*R))
GXY=GXY+GRR*3*X*Y/(R*R)
GYZ=GYZ-GRR*3*Y*Z/(R*R)
GZX=GZX-GRR*3*Z*X/(R*R)
```

20 CONTINUE

C
C ROTATE TOTAL GRADIENT CALCULATED IN INERTIAL REFERENCE FRAME TO
C A LUNAR VERTICAL REFERENCE FRAME, V = VERTICAL, A = ALONG TRACK
C AND C = CROSS TRACK.
C

```
CWCT=COS(TH)
SWCT=SIN(TH)
GVV=GXX*CWCT*CWCT-2*GZX*SWCT*CWCT+GZZ*SWCT*SWCT
GAA=GXX*SWCT*SWCT+2*GZX*SWCT*CWCT+GZZ*CWCT*CWCT
GCC=GYG
GVA=(GXX-GZZ)*SWCT*CWCT+GZX*(CWCT*CWCT-SWCT*SWCT)
GAC=-GXY*SWCT-GYZ*CWCT
GCV=-GXY*CWCT+GYZ*SWCT
```

C
C NOW PUT IN EFFECTIVE GRADIENTS OF THE SPACECRAFT ANGULAR RATES
C

```
WV=0
WA=0
WC=WS
GVV=GVV+WA*WA+WC*WC
GAA=GAA+WV*WV+WC*WC
GCC=GCC+WV*WV+WA*WA
GVA=GVA+WV*WA
GAC=GAC+WA*WC
GCV=GCV+WC*WV
```

C
C PUT IN ANGULAR PERTURBATIONS ABOUT THE LUNAR VERTICAL
C COORDINATES (USE SMALL ANGLES ONLY SINCE THE ROTATION
C MATRICES USED ARE NOT INDEPENDENT)

C
C PUT IN SMALL PERTURBATION ABOUT VERTICAL AXIS
C VP = PERTURBATION ANGLE IN RADIANS (SMALL)

C
C
C VP=0
C CV=COS(VP)
C SV=SIN(VP)
C PVV=GVV
C PAA=GAA*CV*CV+2*GAC*SV*CV+GCC*SV*SV
C PCC=GCC*CV*CV-2*GAC*SV*CV+GAA*SV*SV
C PVA=GVA*CV+GCV*SV
C PAC=GAC*(CV*CV-SV*SV)+(GCC-GAA)*SV*SV
C PCV=GCV*CV-GVA*SV

C
C PUT IN SMALL PERTURBATION ABOUT ALONG TRACK AXIS
C AP=PERTURBATION ANGLE IN RADIANS (SMALL)

C
C
C AP=0
C CA=COS(AP)
C SA=SIN(AP)
C GVV=PVV*CA*CA+2*PCV*SA*CA+PCC*SA*SA
C GAA=PAA
C GCC=PCC*CA*CA-2*PCV*SA*CA+PVV*SA*SA
C GVA=PVA*CA+PAC*SA
C GAC=PAC*CA-PVA*SA
C GCV=PCV*(CA*CA-SA*SA)+(PCC-PVV)*SA*CA

C
C PUT IN SMALL PERTURBATION ABOUT CROSS TRACK AXIS
C CP=PERTURBATION ANGLE IN RADIANS (SMALL)

C
C
C CP=0
C CC=COS(CP)
C SC=SIN(CP)
C PVV=GVV*CC*CC+2*GVA*SC*CC+GAA*SC*SC
C PAA=GAA*CC*CC-2*GVA*SC*CC+GVV*SC*SC
C PCC=GCC
C PVA=GVA*(CC*CC-SC*SC)+(GAA-GVV)*SC*CC
C PAC=GAC*CC-GCV*SC
C PCV=GCV*CC+GAC*SC

```

C
C CONVERT GRADIENTS TO EOTVOS UNITS.
C
    GVV=PVV*1.0E+9
    GAA=PAA*1.0E+9
    GCC=PCC*1.0E+9
    GVA=PVA*1.0E+9
    GAC=PAC*1.0E+9
    GCV=PCV*1.0E+9
C
C CALCULATE IN-PHASE OUTPUTS OF ROTATING GRAVITY GRADIOMETERS
C AND TRACE OF GRADIENT TENSOR.
C (TRACE SHOULD EQUAL TWICE THE SQUARE OF THE ANGULAR RATES.)
C
    GVMA=(GVV-GAA)/2.0
    GAMC=(GAA-GCC)/2.0
    GCMV=(GCC-GVV)/2.0
    GTRA=GVV+GAA+GCC
C
C WRITE RESULTS IN FILES
C
    WRITE(20,1)GVV
    WRITE(21,1)GAA
    WRITE(22,1)GCC
    WRITE(23,1)GVA
    WRITE(24,1)GAC
    WRITE(25,1)GCV
    WRITE(26,1)GVMA
    WRITE(27,1)GAMC
    WRITE(28,1)GCMV
    WRITE(29,1)GTRA
    WRITE(30,1)ALT
    WRITE(31,1)T
1  FORMAT(F10.2)
C
C CONTINUE MOTION ALONG ORBIT
C
    TH=TH+WS*DT
10  CONTINUE
C
C STOP WHEN FINISHED
C
    STOP
    END

```

APPENDIX D

LUNAR POLAR ORBITER GRAVITY GRADIENT EXPERIMENT
SIMULATION PLOTS

LUNAR POLAR ORBITER GRAVITY GRADIENT EXPERIMENT SIMULATION PLOTS

To examine the behavior of a gravity gradient measurement system on board an LPO spacecraft, we used the simulation program in Appendix C.

In our first run with the program, we assumed a circular 60 Km orbit for the spacecraft, and did not introduce any perturbations in the spacecraft attitude. We inserted three mascons. One mascon was on the near side, one at the north pole, and one on the far side. The plots from this simulation are shown in the first two figures. The six outputs of the sensors (see Figure {1} and {2}) were flat, except where they went across the mascons. In Figure {1} we see that all the "principal gradient difference" outputs of the RGG sensor, have significant biases. The bias level on G_{vm} or $(G_{vv}-G_{aa})/2$ is 1266 Eotvos, on G_{mc} or $(G_{aa}-G_{cc})/2$ is 422 Eotvos, and on G_{mv} or $(G_{cc}-G_{vv})/2$ is -1688 Eotvos. The three cross gradient outputs (See Figure {2}) were zero except when they crossed a mascon.

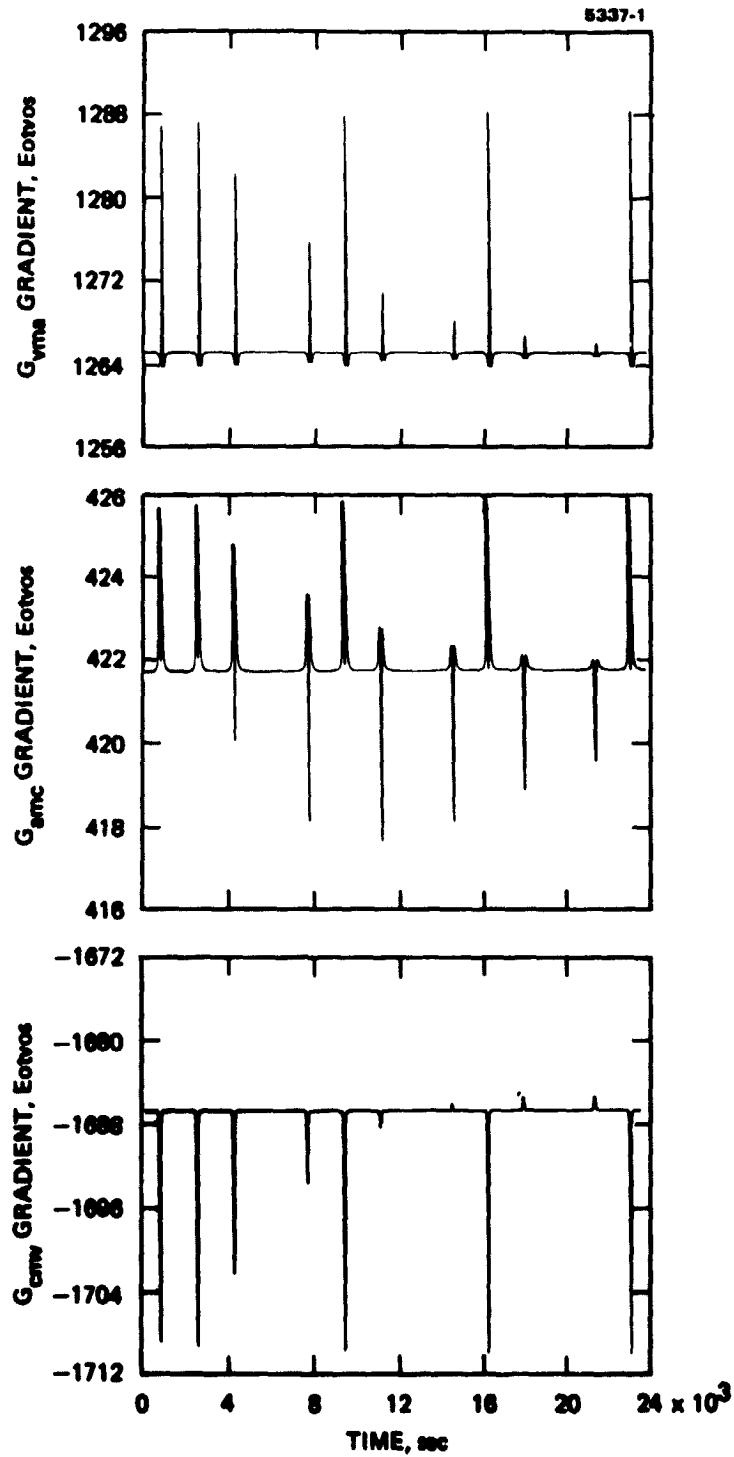


Figure (1) - RGG Principal Gradient Difference Outputs
60 Km Circular Orbit

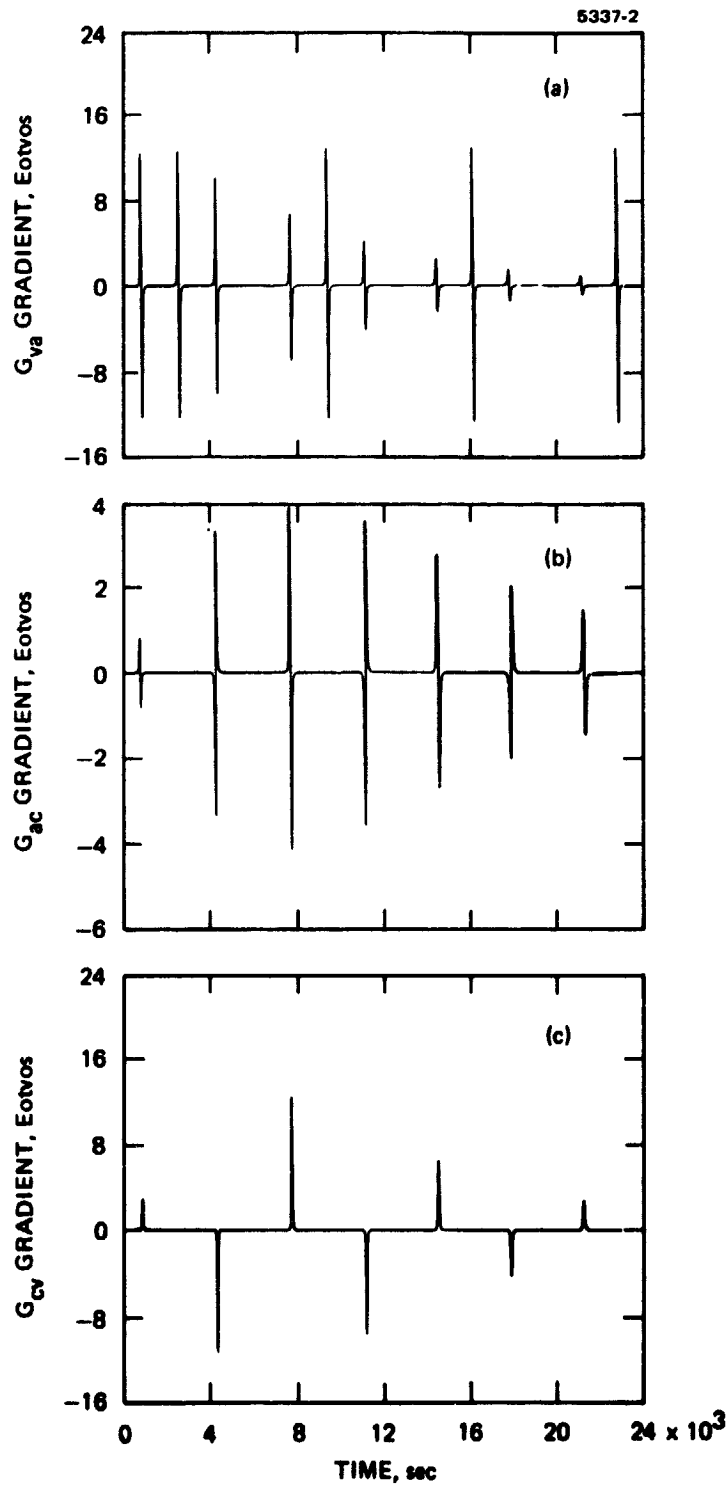


Figure {2} - RGG Cross Gradient Outputs
60 Km Circular Orbit

From these sensor outputs we can calculate the three principal gradient tensor components (See Figure {3}) and the trace of the gradient tensor.

For the zero eccentricity, zero attitude error case, the principal vertical gradient G_{vv} bias is 2532 Eotvos, the principal cross track gradient G_{cc} bias is -844 Eotvos and the principal along track gradient G_{aa} bias is zero. This last occurs because the along track gravity gradient is exactly canceled by the rotational rate gradient of the spacecraft rotating once per orbit to maintain a local vertical orientation.

Because the spacecraft is vertically stabilized, it is rotating with respect to inertial space. Since the trace of the gradient tensor G_{tra} is independent of the lunar or mascon gravity fields and is only equal to the square of the angular rate of the spacecraft, it was constant at 1688 Eotvos.

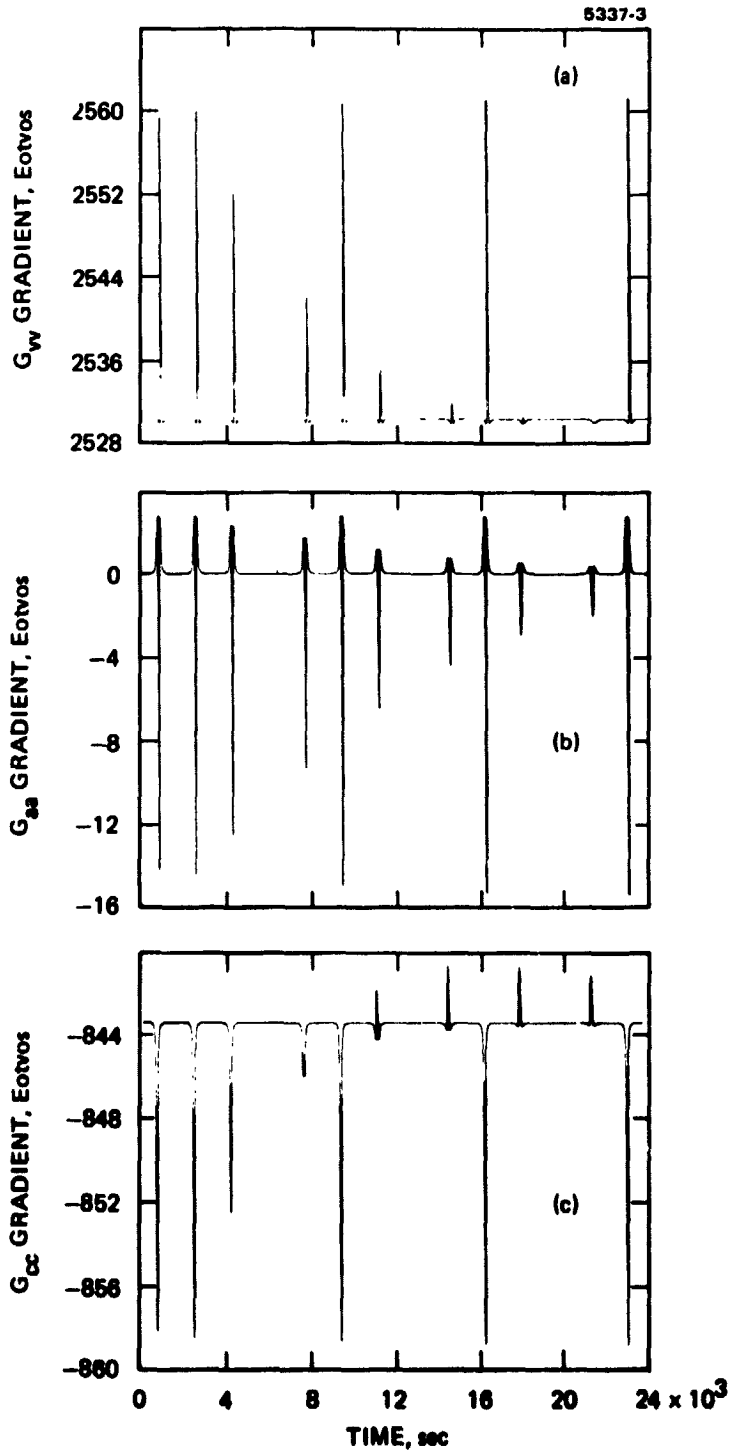


Figure {3} - Derived Principal Gradients
60 Km Circular Orbit

We then introduced an eccentricity of $e=0.005$ into the orbit. This caused the spacecraft altitude to vary from 60 Km on the near side to 78 Km on the far side. With this altitude variation we get variations in the measured gradient of tens of Eotvos because of the background gravity gradient of the moon. But as can be seen in Figure {4} through Figure {6}, these variations occur very slowly compared to the more rapid changes in the gradient as we cross over a mascon and their strict once per orbit periodicity should allow us to remove them from the sensor data.

Note, however, that not all the gradiometer outputs are affected. As we can see in Figure {5}, the sensor outputs that give a measure of the cross gradients do not have any shift in their bias level due to the eccentricity of the orbit since their initial bias was zero. Thus, even for an elliptical orbit, we can use this data just as it comes from the sensor without any preprocessing and integrate it to get the gravity.

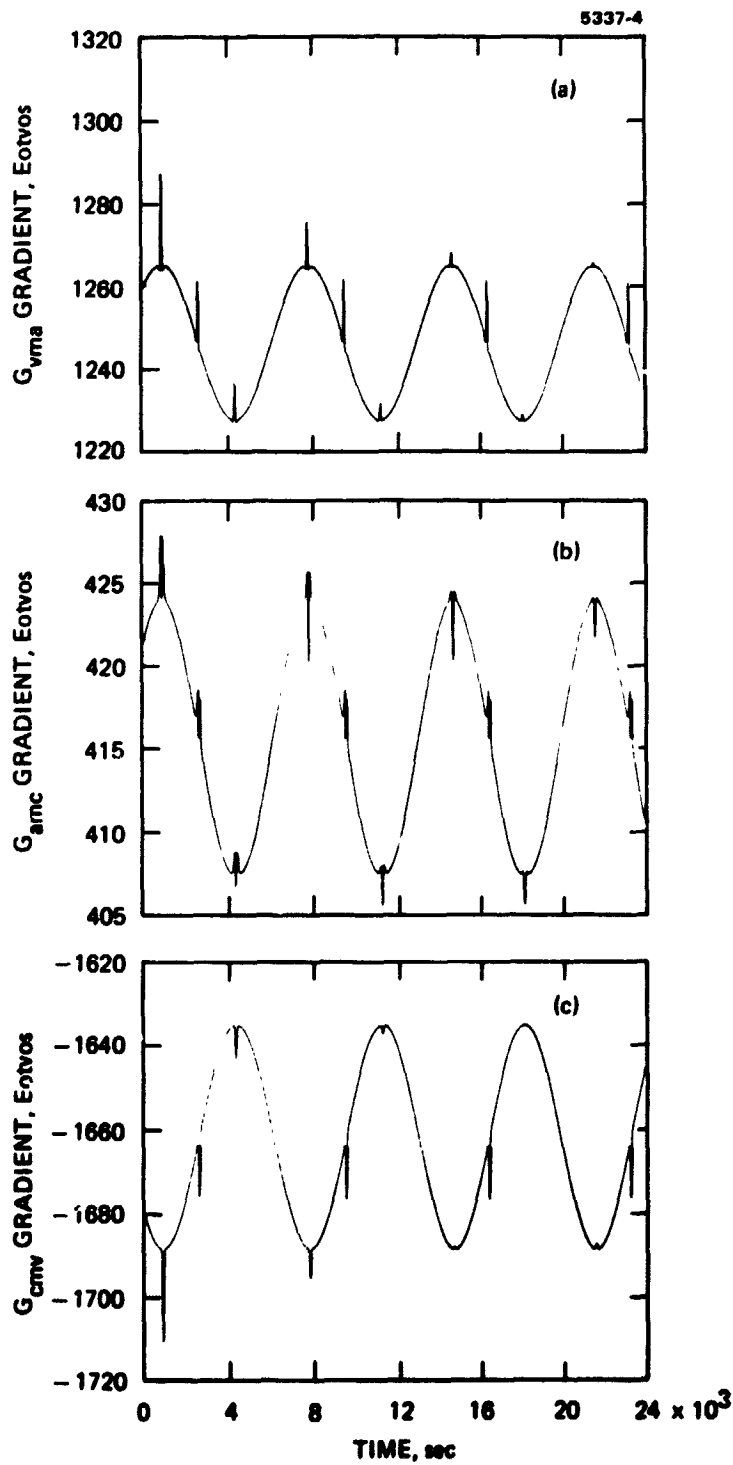


Figure {4} - RGG Principal Gradient Difference Outputs
60 Km Perilune ($e = 0.005$)

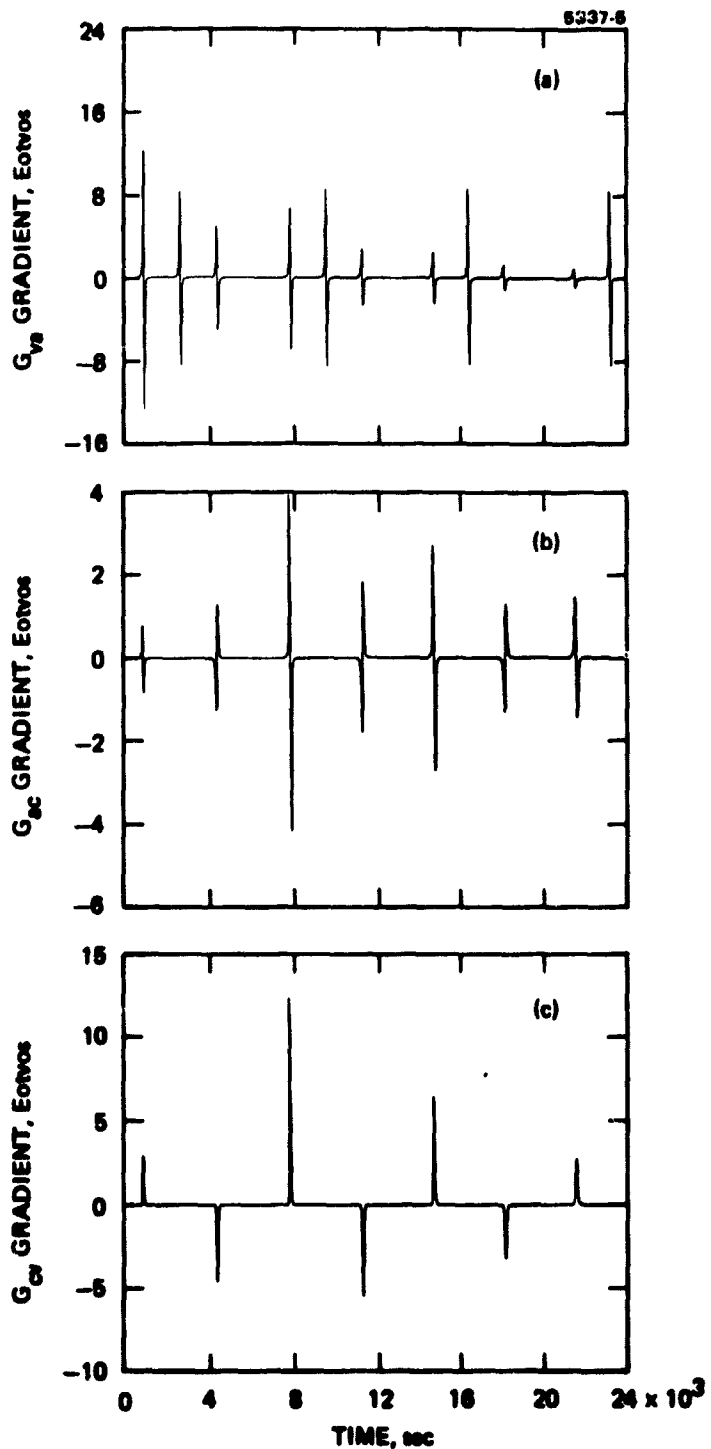


Figure {5} - RGG Cross Gradient Outputs
60 Km Perilune ($e = 0.005$)

5337-6

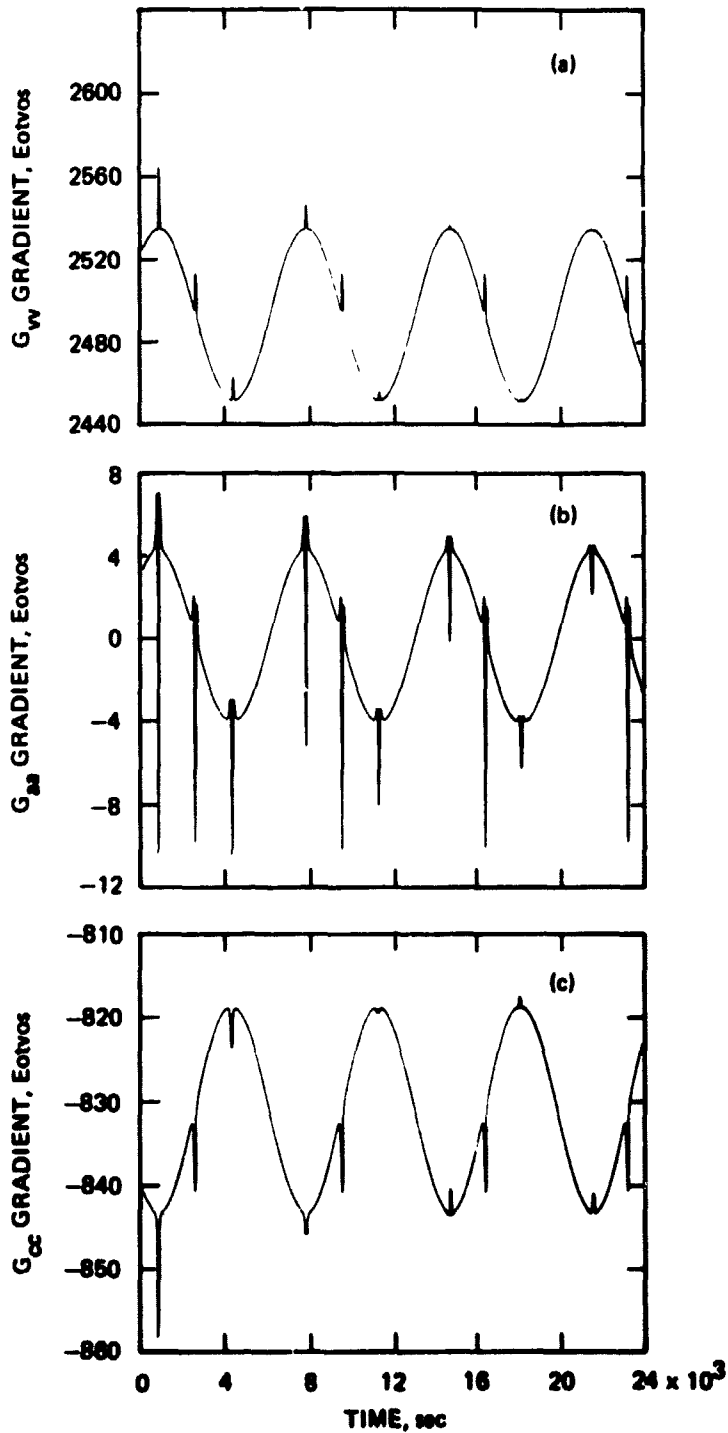


Figure {6} - Derived Principal Gradients
60 Km Perilune (e = 0.005)

If we have three sensors and can obtain the trace of the gradient tensor, we find that the trace has the same variation as the altitude (See Figure {7}), but it has no gravity information in it since the trace of the gravity part of the gradient tensor is zero. The variation seen in the trace of the gradient tensor is just the angular rate variation due to the ellipticity of the orbit and is a direct measure of the ellipticity and altitude. The amplitude of the variations in the trace are about 4 Eotvos for a 1 Km change in altitude. Since we can curve fit over many minutes (say 1000 sec), then the accuracy of the curve fit would be 0.1 Eotvos and we see that we can use the output of the trace of the gravity gradient measurement system to estimate the spacecraft altitude variations to better than 25 m.

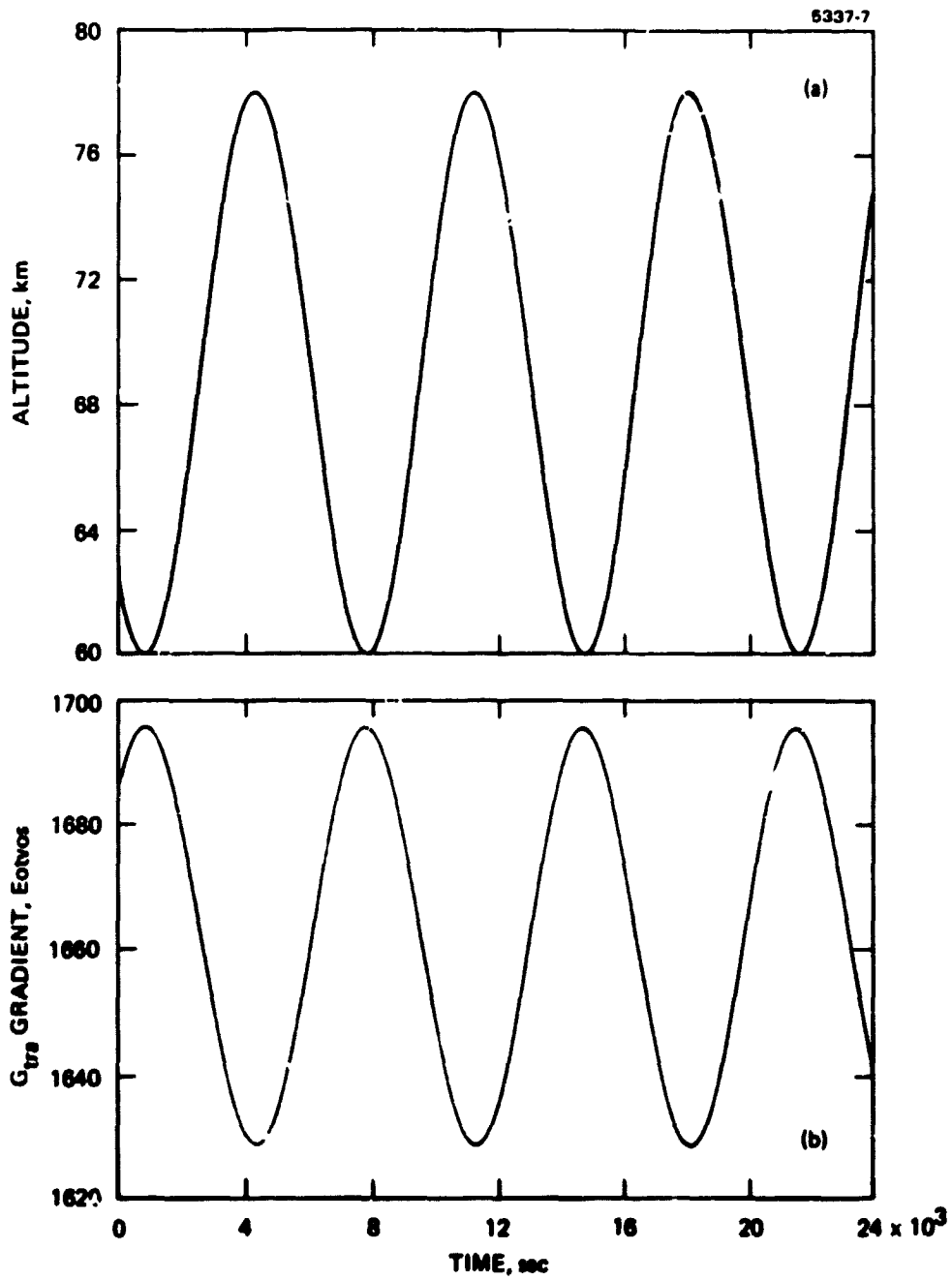


Figure {7} - Spacecraft Altitude and Gradient Tensor Trace
60 Km Perilune ($e = 0.005$)

It is instructive to examine the very low frequency harmonic portions of the many gradiometer outputs, since they have significantly different responses to the altitude variation and angular rate variations that are caused by the ellipticity of the orbit.

In a simple elliptical two body orbit, the radius R of the orbit varies as

$$1/R = (1 + e \cos(a))/A$$

where A is the average orbital radius
 e is the eccentricity of the orbit
 a is the angle along the orbit

The square of the orbital angular rate W_{cc} of the spacecraft for this simple orbit varies as:

$$W_{cc} = W_c \times W_c = G_{rr} (1 + e \cos(a))$$

where $G_{rr} = GM/R^3$ is the gravity gradient amplitude.
 W_c = orbital angular rate

Since the gravity gradient amplitude G_{rr} varies as the inverse cube of R , if the eccentricity of the orbit is small, this can be approximated by:

$$G_{rr} = G_{gg} (1 + 3e \cos(a))$$

where $G_{gg} = GM/A^3$ is the average gravity gradient amplitude

In the same manner, the square of the orbital angular rate has the variation:

$$W_{cc} = G_{gg} (1 + 4e \cos(a))$$

Because the LPO spacecraft is stabilized to the Lunar vertical by a control system sensing the Lunar horizon, the spacecraft is rotating with respect to the inertial space at an instantaneous rate that is identical to the instantaneous orbital angular rate. The gradiometer instruments will measure the gradients of both the Lunar gravity field (which will vary with the change in orbital radius), and the gradient of the angular rate (which varies in a different manner with the motion along the orbit).

After a bit of calculation it can be shown that the low frequency components of the six gradiometer outputs have the variation:

$$Gvma = 1.5 \quad Grr = Ggg (1.5 + 4.5e \cos(a))$$

$$Gamc = 0.5 \quad Wcc = Ggg (0.5 + 2.0e \cos(a))$$

$$Gcmv = -1.5 \quad Grr - 0.5 \quad Wcc = Ggg (-2 - 6.5e \cos(a))$$

$$Gva = Gac = Gcv = 0$$

Notice that the $Gvma$ gradiometer output does not contain any of the spacecraft angular rate in the cross track direction (the orbital axis direction), thus its output is pure gravitational data. The low frequency variations seen in this output are then directly related to the orbital radius variation through the inverse cube law of the gravity gradient.

From the gradiometer outputs we can derive other outputs such as the principal components of the gradient tensor:

$$Gvv = 2Grr + Wcc = Ggg (3 + 10e \cos(a))$$

$$Gaa = -Grr + Wcc = Ggg (0 + e \cos(a))$$

$$Gcc = -Grr = Ggg (1 + 3e \cos(a))$$

and the trace of the gradient tensor

$$Gtra = 2 \quad Wcc = Ggg (2 + 8e \cos(a))$$

If we have a three axis gradiometer system, then the gradient trace will be a very important output, for it will contain no gravity gradient signals at any harmonic order, so any variations seen in the trace - fast or slow - are due to angular rate variations. Their presence in the trace will mean that similar variations will be found in the other outputs of the system and that these output variations are due to angular rate variations and are not due to gravity anomalies.

We then repeated the simulation for a circular orbit at 60 Km with the spacecraft attitude off about the along track direction (roll) by 1 degree (17 milliradians). We now again get essentially flat traces except for the mascons (See Figures {8} through {10}). The RGG principal gradient difference outputs (See Figure {8}) are almost the same as they were for perfect attitude (the cosine of one degree is very close to one) and the cross gradient outputs (See Figure {9}) have zero bias except for G_{cv} , which now has a constant bias of -58 Eotvos due to the roll of one degree. Thus, by attributing this bias to a spacecraft attitude error, we could use the cross gradient component bias to estimate the spacecraft attitude error to much better than a milliradian.

Notice that in the plots of the cross gradient terms G_{ac} and G_{cv} , the north pole mascon shows up as a slight signal whereas for perfect roll orientation (See G_{ac} and G_{cv} in Figure {2}), those cross gradient components remain zero during the polar mascon crossing. These errors could be eliminated in post data processing using the G_{cv} bias knowledge, but even if they are not, the effect is only to misplace the mascon by 600 meters for 60 Km altitude - a shift that is far less than the data resolution.

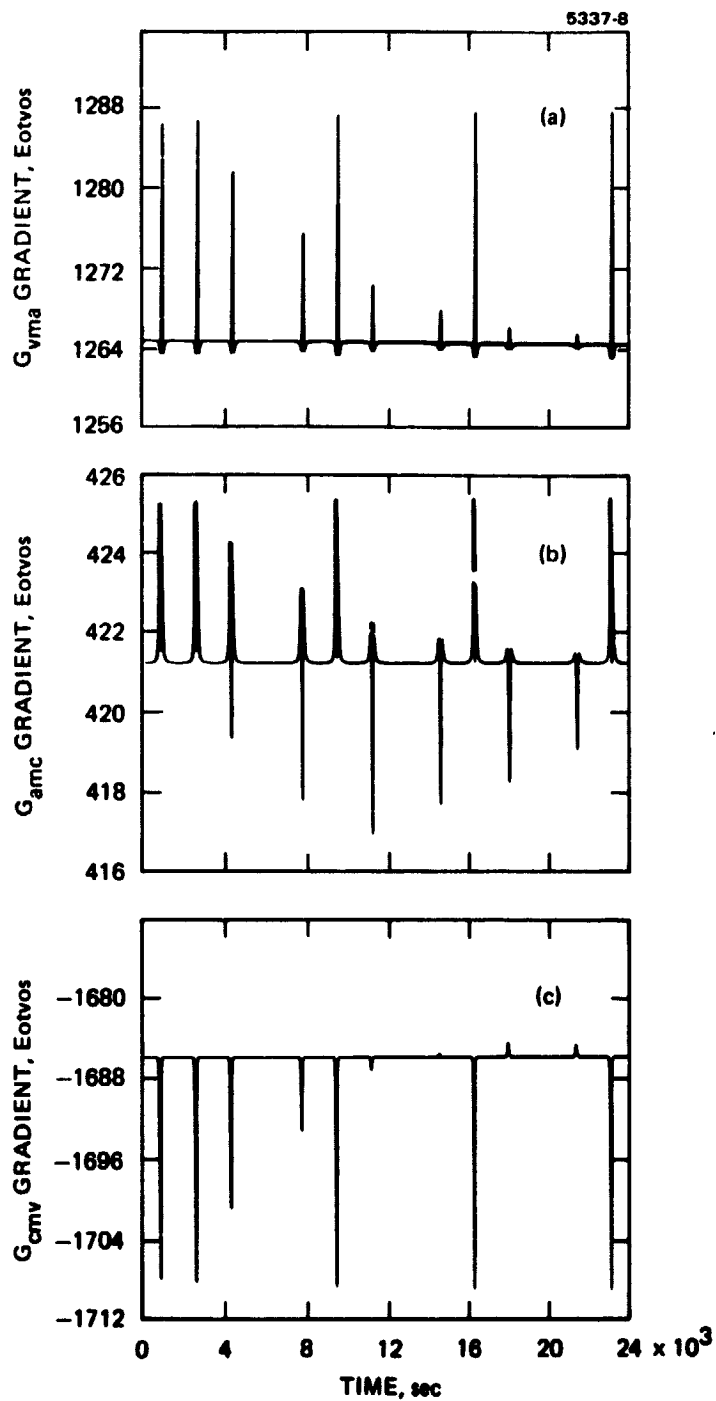


Figure {8} - RGG Principal Gradient Difference Outputs
 60 Km Circular Orbit
 1 Degree Roll Bias

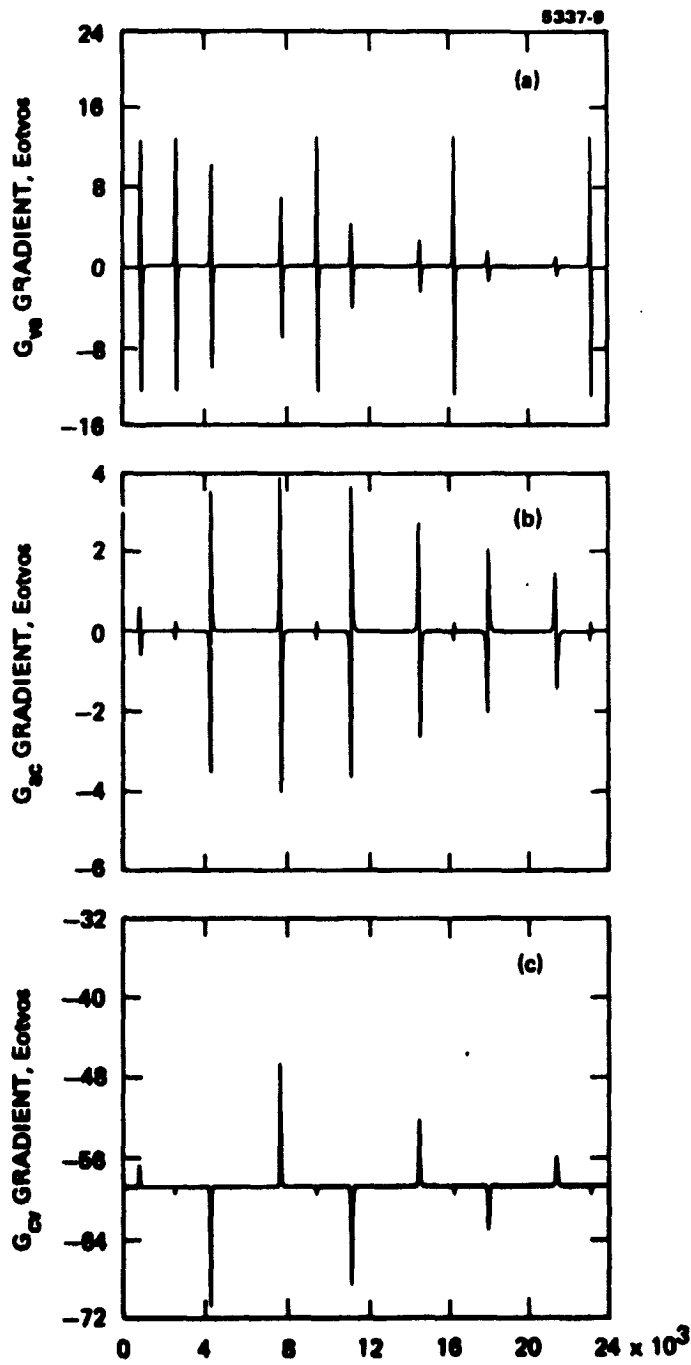


Figure (9) - RGG Cross Gradient Outputs
 60 Km Circular Orbit
 1 Degree Roll Bias

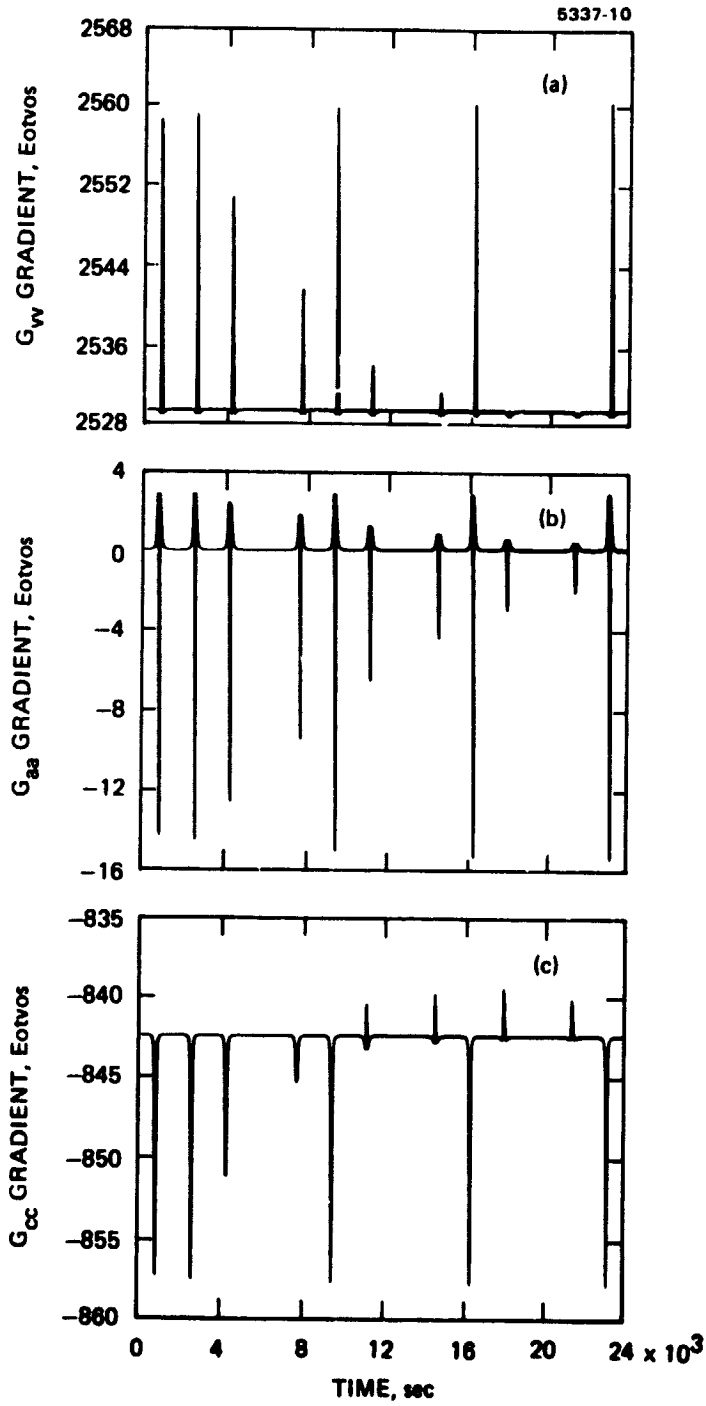


Figure {10} - Derived Principal Gradients
 60 Km Circular Orbit
 1 Degree Roll Bias

Since it seemed from the plots and our previous experience that a great deal of information could be obtained from a single RGG sensor oriented along the orbit axis so that it measured the gradients in the orbital plane, we decided to generate some simulations using only the output of one RGG sensor. One of the questions was whether a single sensor oriented to sense the gradients along the orbital track would provide adequate resolution for mascons separated in the cross track direction.

To look at this question we rearranged the orbital equations to give us traces of the gravity gradient output as the orbit passed over the front side of the moon in 20 successive orbits. On the front side we placed three mascons. One directly at the nearside point, one north of it (along the orbital track) and one to the west (in the cross track direction). We first spaced the mascons at 60 Km separation, the same distance as the altitude. The plots were then presented in a perspective view.

We first needed something to compare the single sensor output with. In Figure {11} is plotted the vertical gradient of the vertical gravity G_{vv} . Our previous simulations had shown that this gradient component was of high resolution and gave a good representation of the mass distribution. Examination of the plot shows that this component of the gravity gradient tensor can separate the three mascons, both along track and cross track even when the spacecraft altitude is equal to the mascon spacing.

5337-11

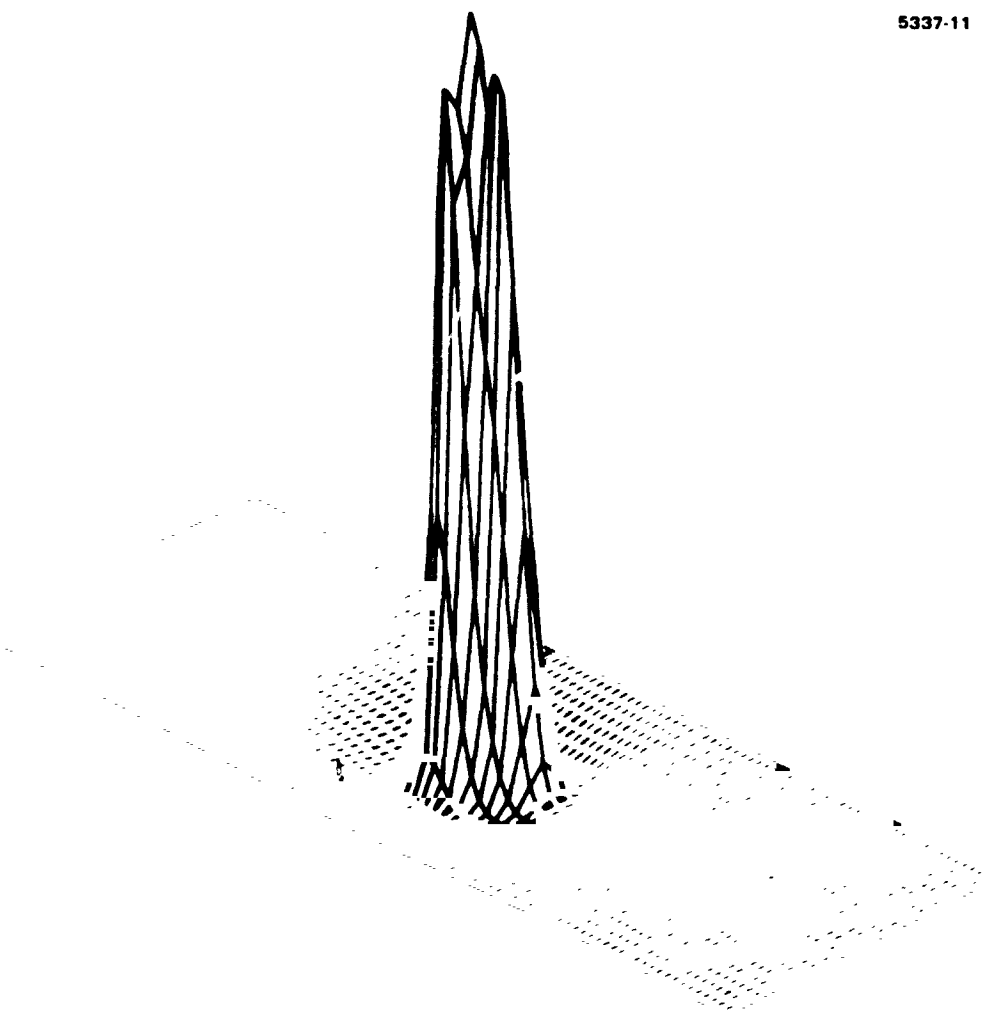


Figure {11} - Vertical Gradient of Vertical Gravity
Three Mascon with 60 Km Spacing
60 Km Circular Orbit

Now the vertical gradient of the vertical gravity G_{vv} is not one of the normal outputs of a single RGG system, but has to be derived from the outputs of three gravity gradiometers. The nearest equivalent sensor output of a single RGG system is the sine output of the RGG which is the difference of the vertical gradient and the along track gradient $(G_{vv}-G_{aa})/2$. This sensor output is plotted in Figure {12}. We see that it is a slightly distorted version of G_{vv} . It has equivalent resolution in the cross track direction, and slightly better resolution in the along track direction.

5337-12

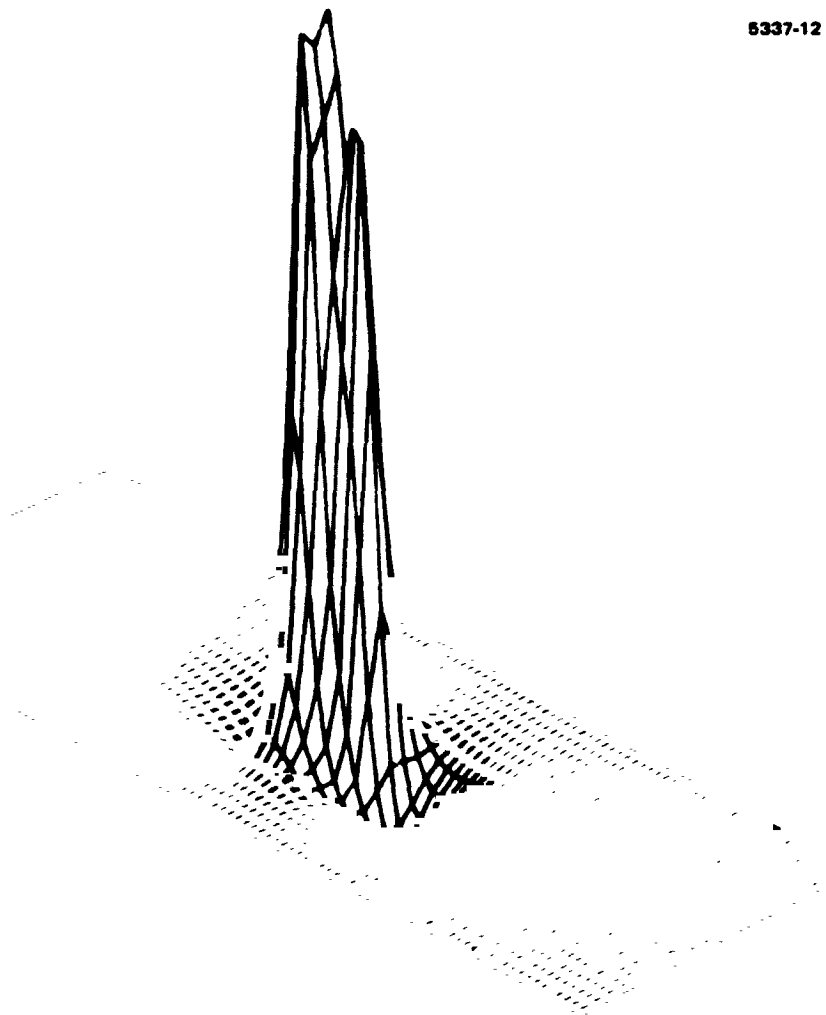


Figure {12} - RGG Principal Gradient Difference Output
Three Mascons at 60 Km Spacing
60 Km Circular Orbit

The other output of a single RGG sensor is the cross gradient, which is positive on one side of a mascon, drops through zero over the mascon and goes negative on the other side (See Figure {13}). If this cross gradient output is multiplied by the spacecraft velocity and integrated with time, the result is the vertical gravity.

5337-13

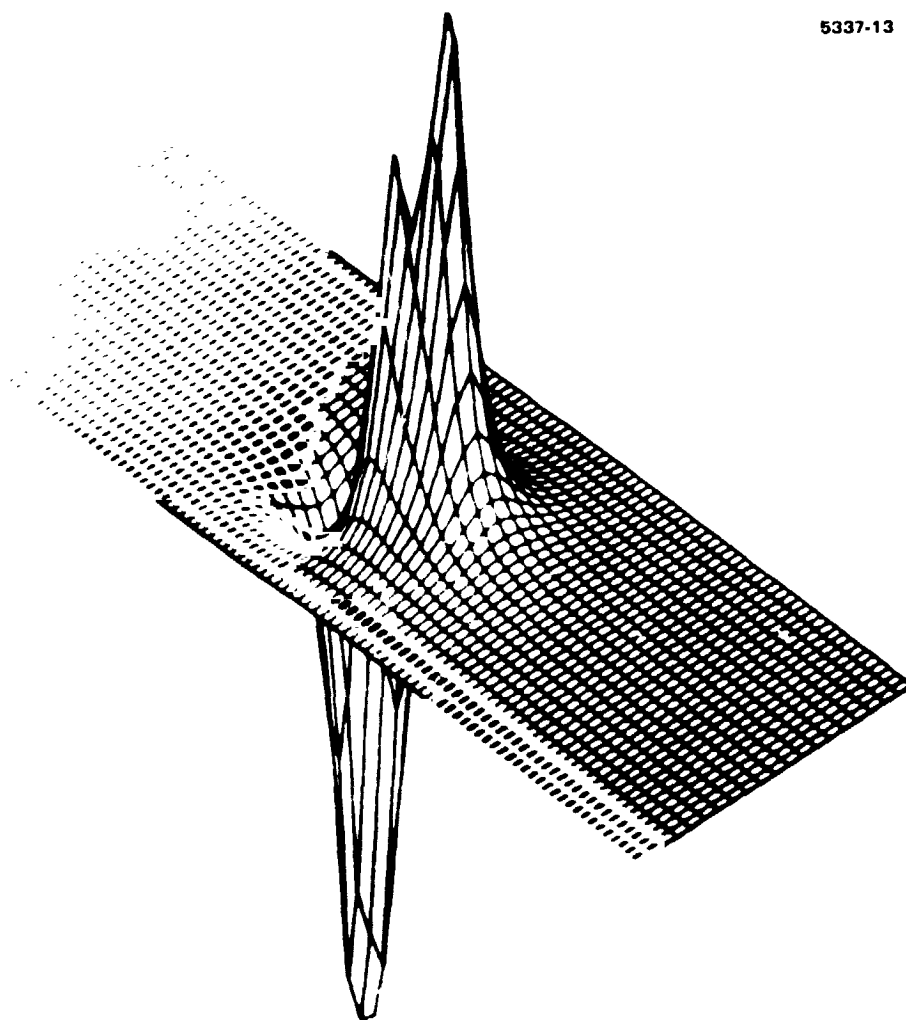


Figure {13} - RGG Cross Gradient Output
Three Mascons at 60 Km Spacing
60 Km Circular Orbit

Figure {14} is the integrated cross gradient output of a single RGG sensor. There is a nice rounded peak, but it is obvious that the integrated cross gradient does not have the resolution to see the three mascons when they are separated by a distance equal to the spacecraft altitude. However, this integrated output gives an undistorted gravity contour map. Thus for optimum data processing, this undistorted but lower resolution integrated output should be used in conjunction with the higher resolution (but slightly distorted) principal gradient difference output to provide a high resolution, low distortion data set for determining underground mass distributions.

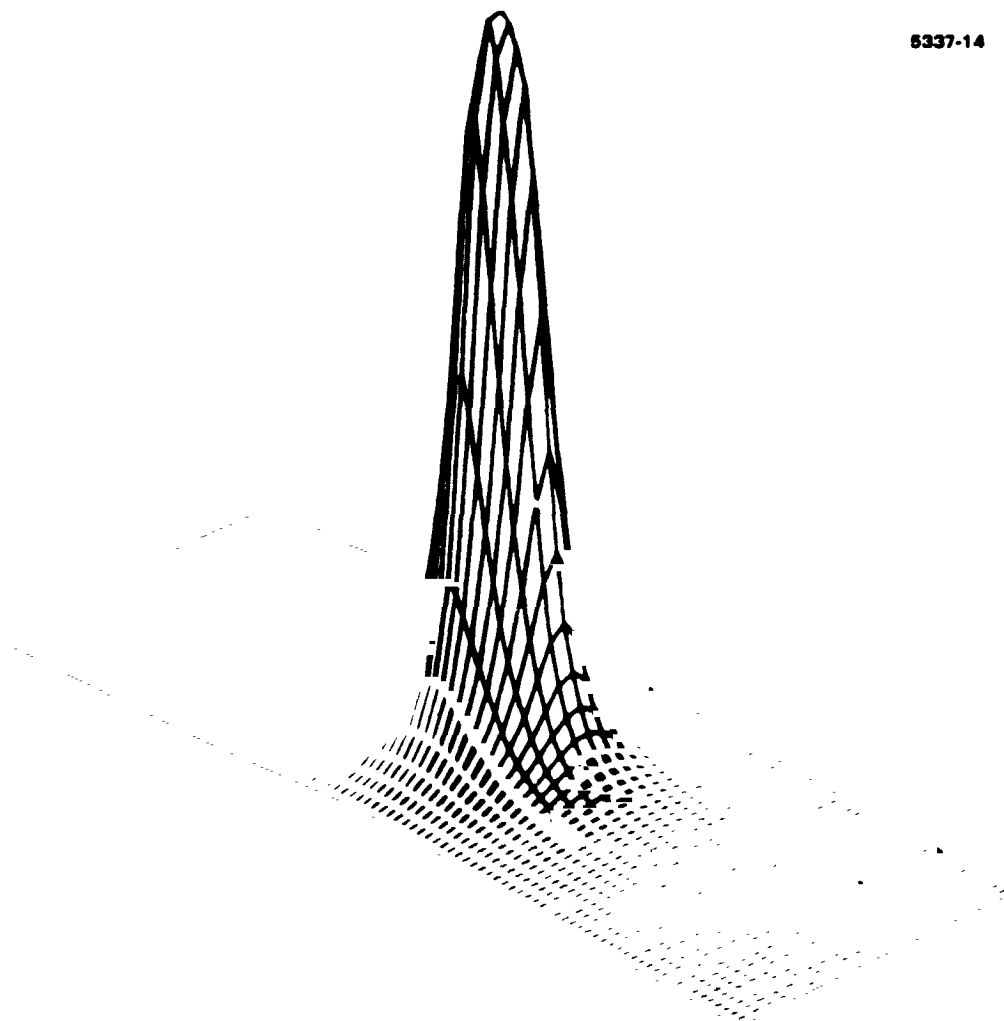


Figure {14} - Integrated RGG Cross Gradient Output
Three Mascons at 60 Km Spacing
60 Km Circular Orbit

We next wanted to study the effects of an elliptical orbit on the data resolution. We used the same three mascon set as in the previous plots, but now we spaced them 120 Km (4 degrees) apart. We chose an orbital eccentricity of $e=0.005$ (which gives an orbital altitude variation from 60 to 78 Km) and we placed the perilune of the ellipse right over the three mascon set. In Figure {15} is shown the best that could be obtained from a three sensor system, the vertical gradient of the vertical gravity. Notice, that although there is a significant curvature to the data, the mascon peaks are still resolved.

5337-15

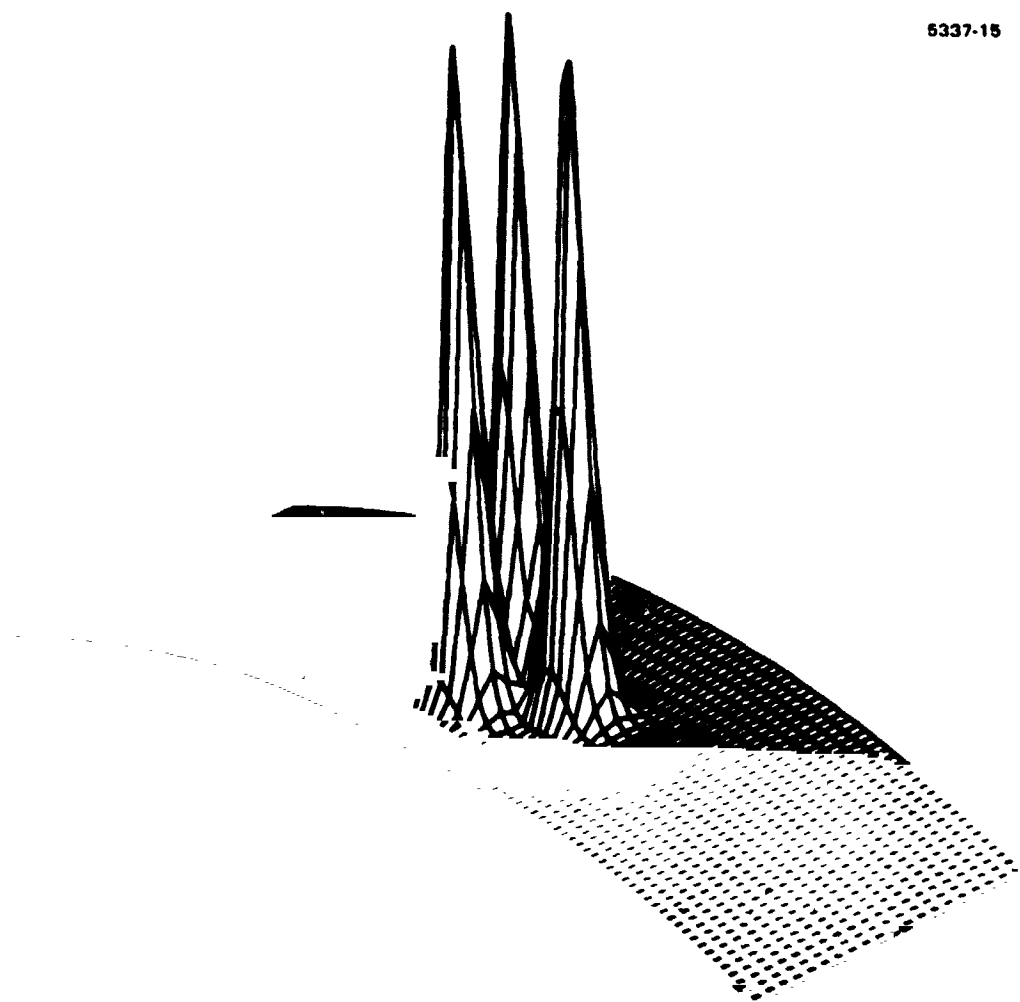


Figure {15} - Vertical Gradient of Vertical Gravity
Three Mascons at 120 Km Spacing
60 Km Perilune of $e=0.005$ Elliptical Orbit

A plot of the principal gradient difference output G_{vma} of a single RGG for the same orbital conditions is shown in Figure {16}. It too has good sensitivity and resolution for the elliptical orbit case.

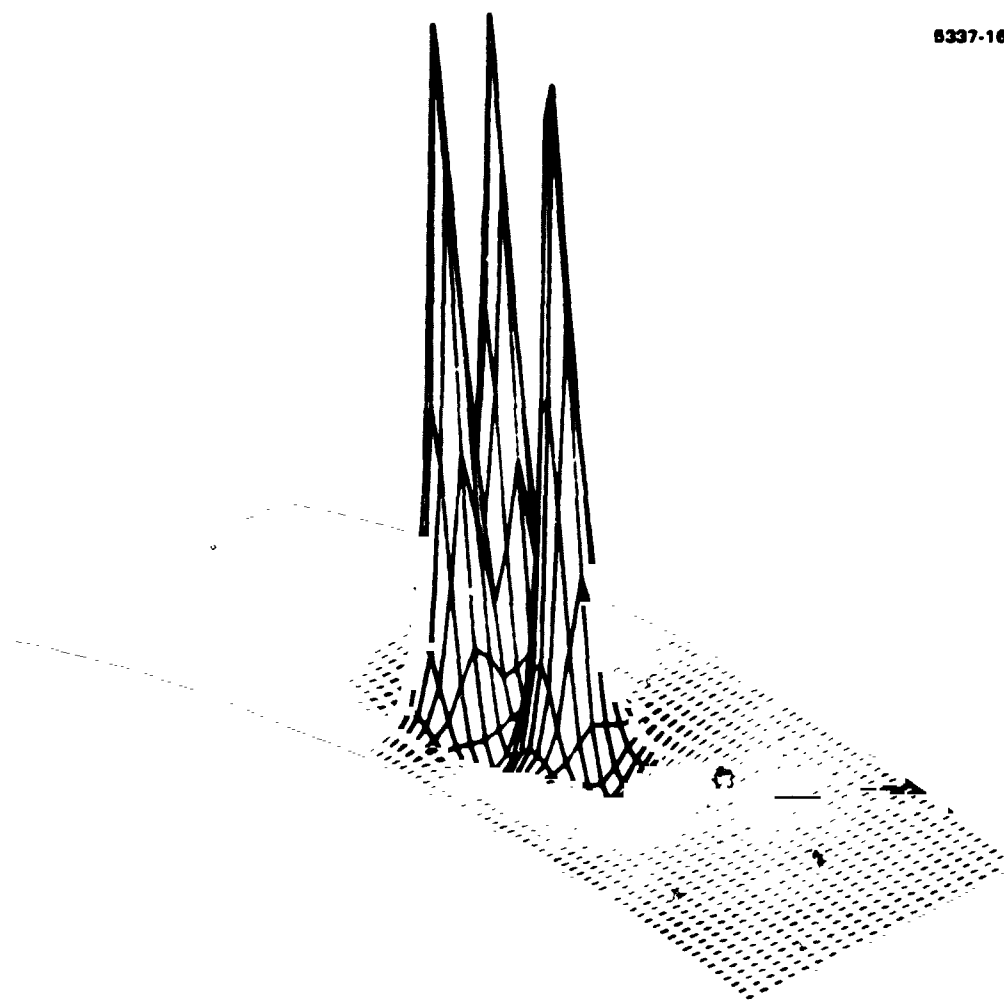


Figure {16} - RGG Principal Gradient Difference Output
Three Mascons at 120 Km Spacing
60 Km Perilune of $e=0.005$ Elliptical Orbit

The other output of a single RGG system is the cross gradient output, and as before, we can integrate it to obtain the vertical gravity. Although there might be some concern about the integration because of the elliptical orbit, the average bias of the signal in the cross gradient term is zero (see previous discussion about Figure {5}) and the integration proceeds well. (The slight ridge in the back portion of the plot in Figure {17} is due to computer roundoff error.)

5337-17

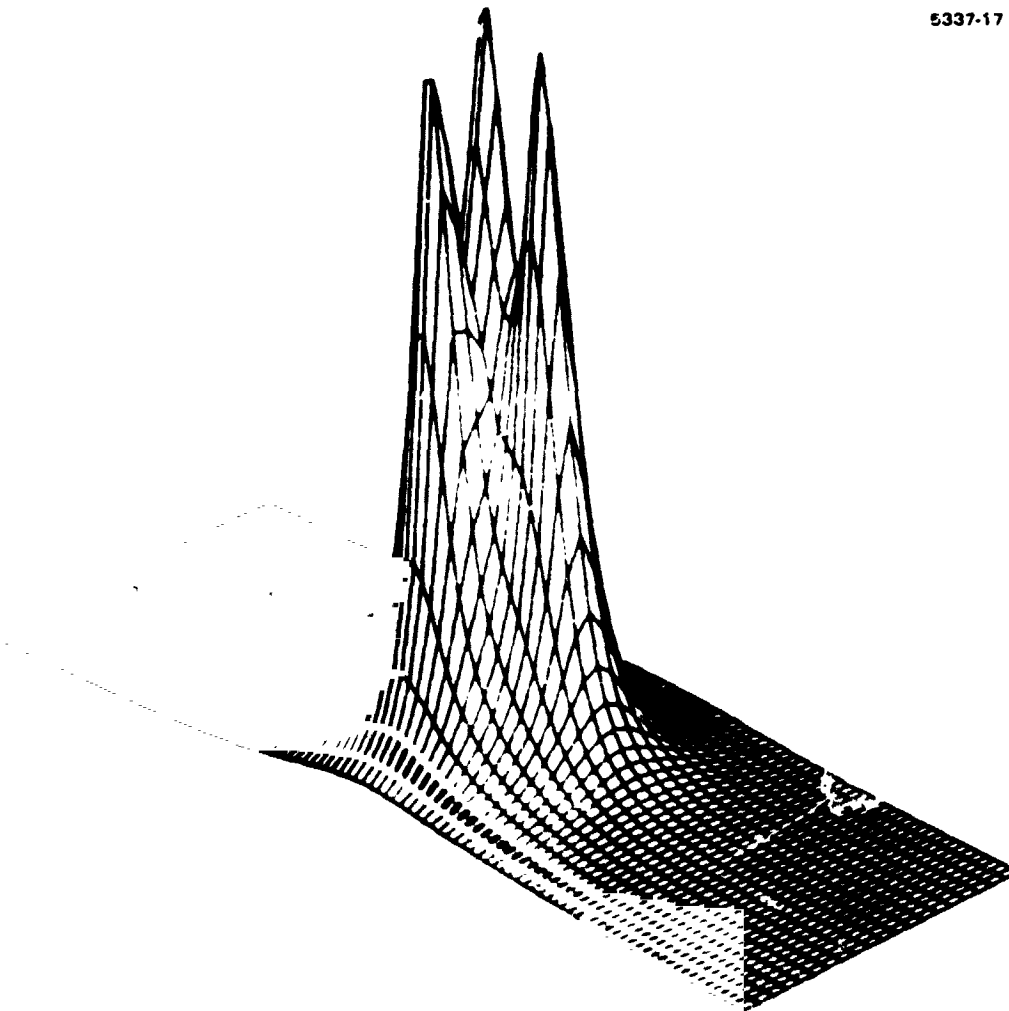
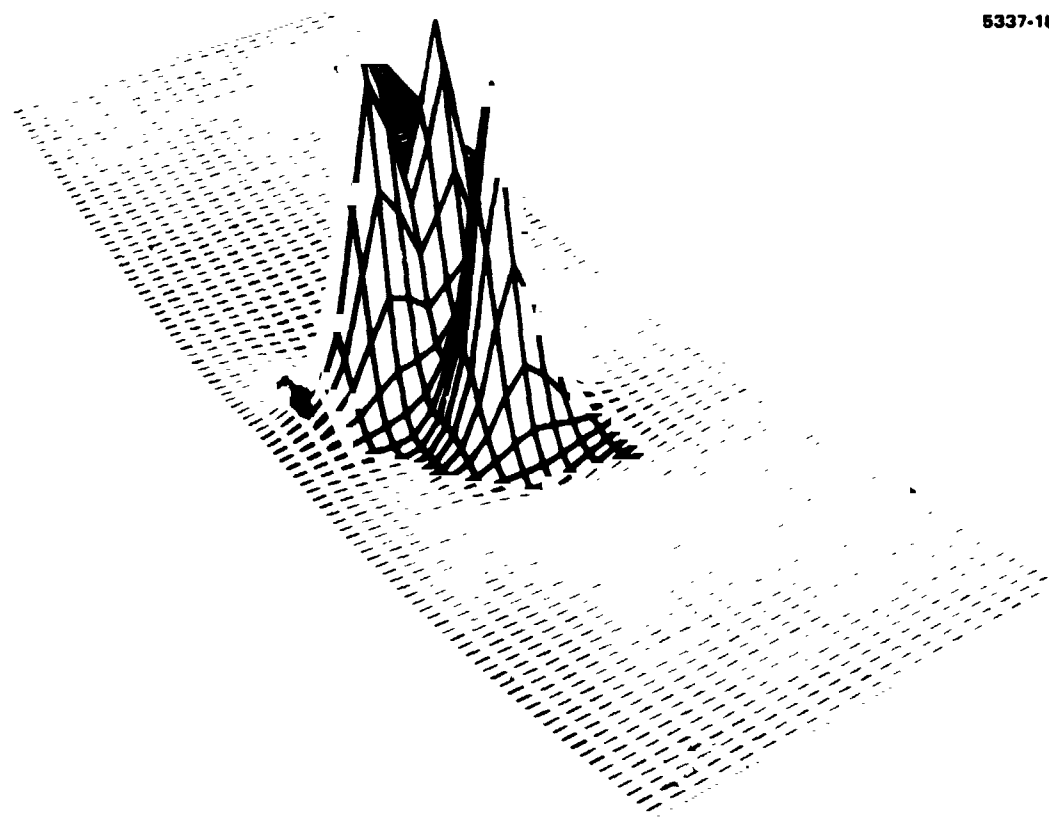


Figure {17} - Integrated RGG Cross Gradient Output
Three Mascons at 120 Km Spacing
60 Km Perilune of $e=0.005$ Elliptical Orbit

The simulation was then changed so that the apolune of the elliptical orbit was over the three mascon set. The principal gradient difference output of a single RGG is plotted in Figure {18}. Notice that the curvature of the data is in the opposite direction, and that the sensitivity and resolution of the data is less. This is to be expected from the increase in spacecraft altitude over the three mascon set from 60 Km to 78 Km.



5337-18

Figure {18} - RGG Principal Gradient Difference Output
Three Mascons at 120 Km Spacing
78 Km Apolune of $e=0.005$ Elliptical Orbit

Figure {19} gives the integrated cross gradient output of a single RGG system. Again, this plot has less resolution because of the data integration and the higher spacecraft altitude.

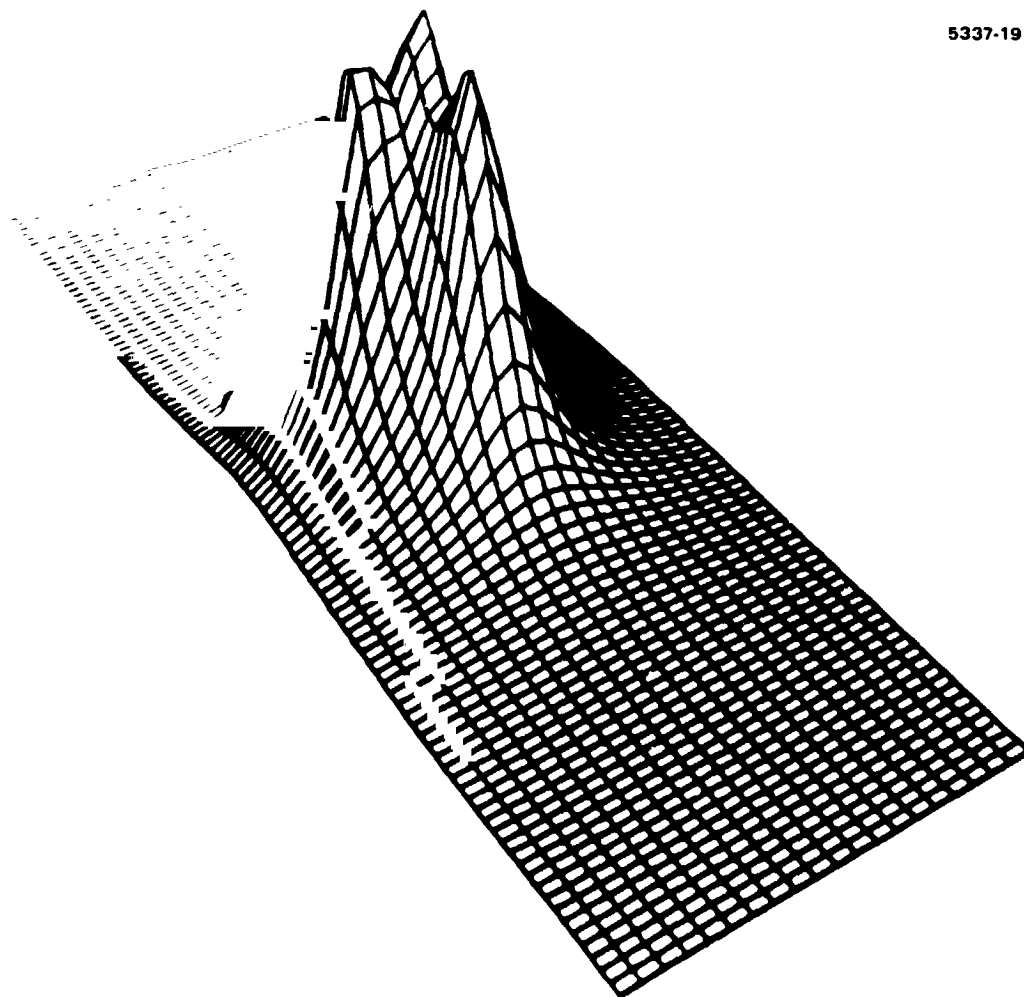


Figure {19} - Integrated RGG Cross Gradient Output
Three Mascons at 120 Km Spacing
78 Km Apolune of $e=0.005$ Elliptical Orbit

We next tried to get a feeling for the combined effects of a number of error sources on the performance of a single RGG system. We simulated an elliptical orbit with an eccentricity of 0.005 and with the three mascon set halfway between perilune and apolune so that there would be a large background bias shift. We then introduced a periodic attitude control error perturbation with an amplitude of 0.1 degree and a five minute period. This introduced bias shift errors due to the attitude change, and angular rate errors due to the gradient of the rate of the error. Figure {20} shows that the effects of the errors are significant, but the mascons are still resolvable.

5337-20

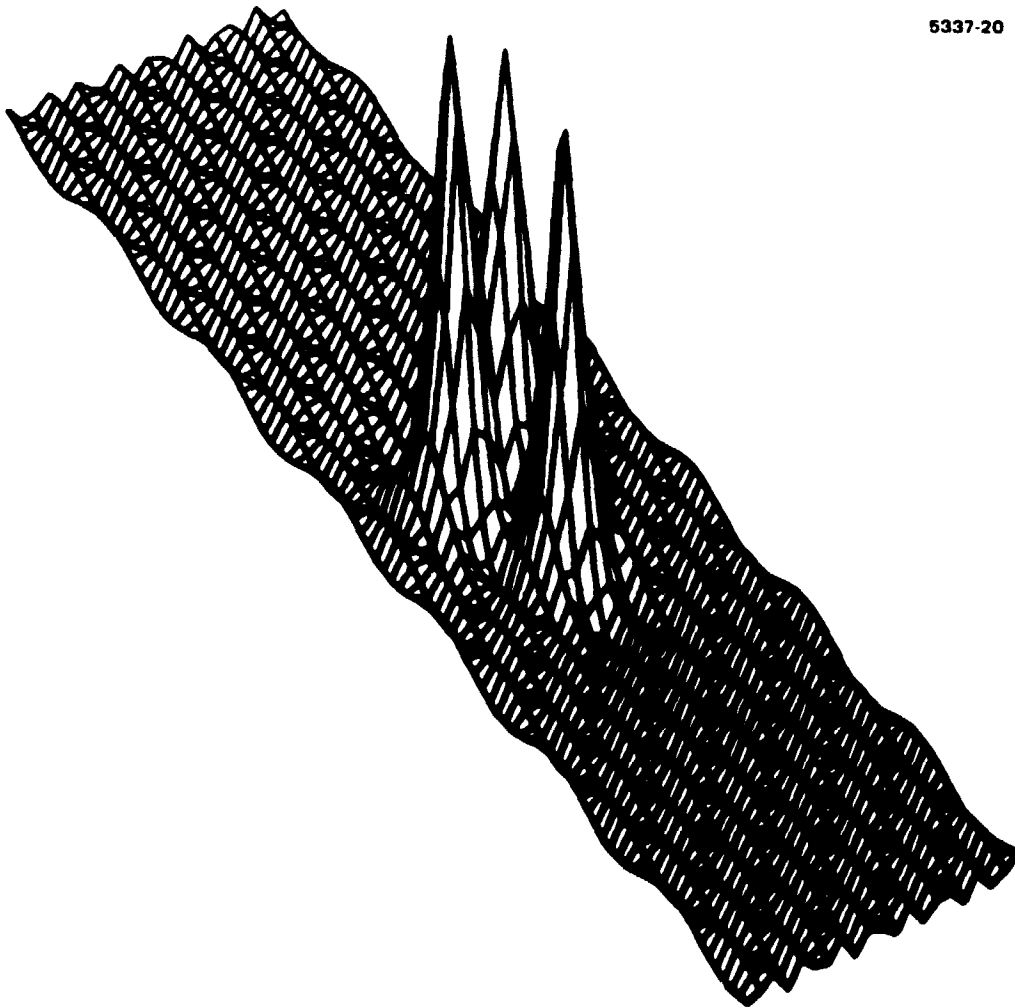


Figure {20} - RGG Principal Gradient Difference Output
Three Mascons at 120 Km Spacing
0.1 Degree Periodic Attitude Error
 $e=0.005$ Elliptical Orbit

The plot of the vertical gravity obtained from the integrated cross gradient output of the single RGG system (See Figure {21}) shows a considerably better picture. Although the resolution is still not as good because of the inherent resolution advantage of the gradient over the gravity, there is still adequate resolution, and of equal importance, better signal-to-noise. This is partially due to the integration process which tends to smooth out the higher frequency components of the data and noise.

5337-21

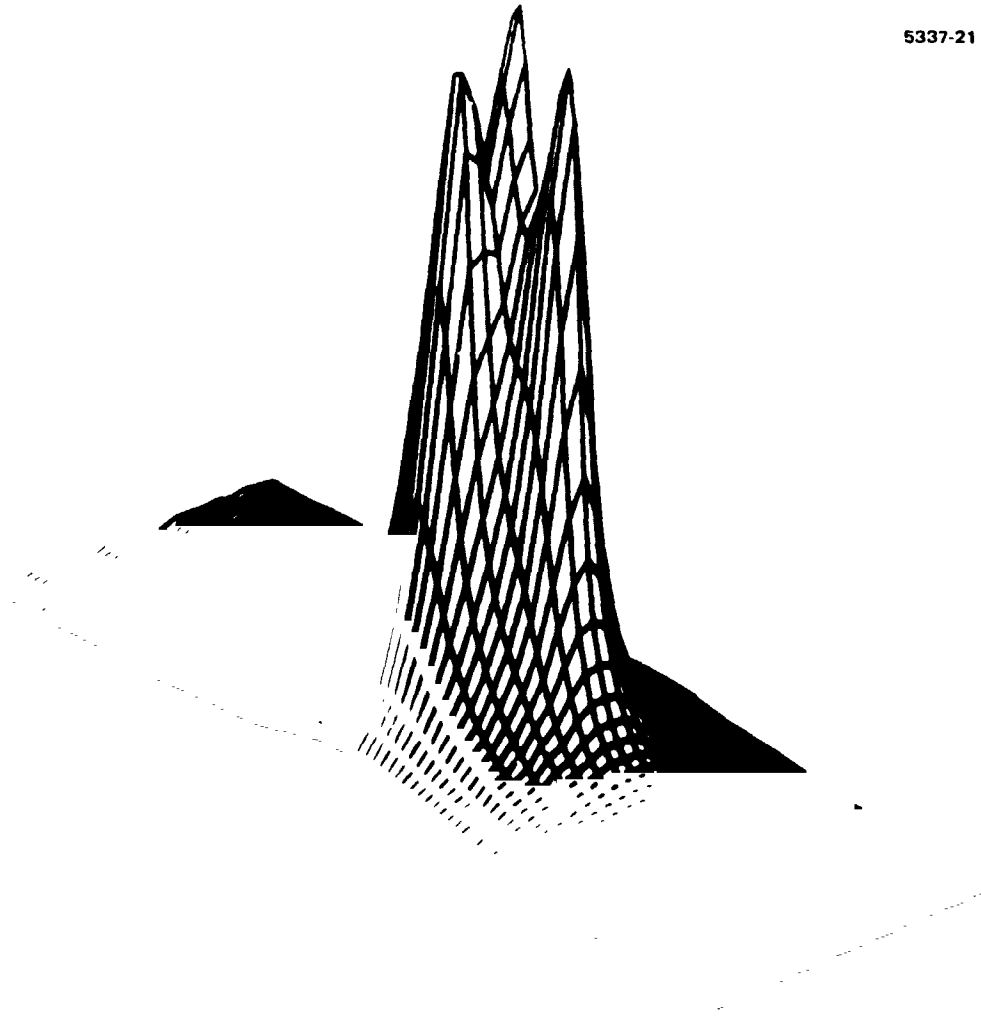


Figure {21} - Integrated RGG Cross Gradient Output
Three Mascons at 120 Km Spacing
0.1 Degree Periodic Attitude Error
 $e=0.005$ Elliptical Orbit

However, the better signal to-noise of the integrated cross gradient output of the single RGG system is not just due solely to the integration of the data, but is due partially because the cross gradient output has smaller variations caused by the attitude control errors. As we can see in comparing Figure {22} with Figure {20}, the attitude error variations are less for the cross gradient output. Thus this shows that the two outputs are complementary and both should be used for best results.

5337-22

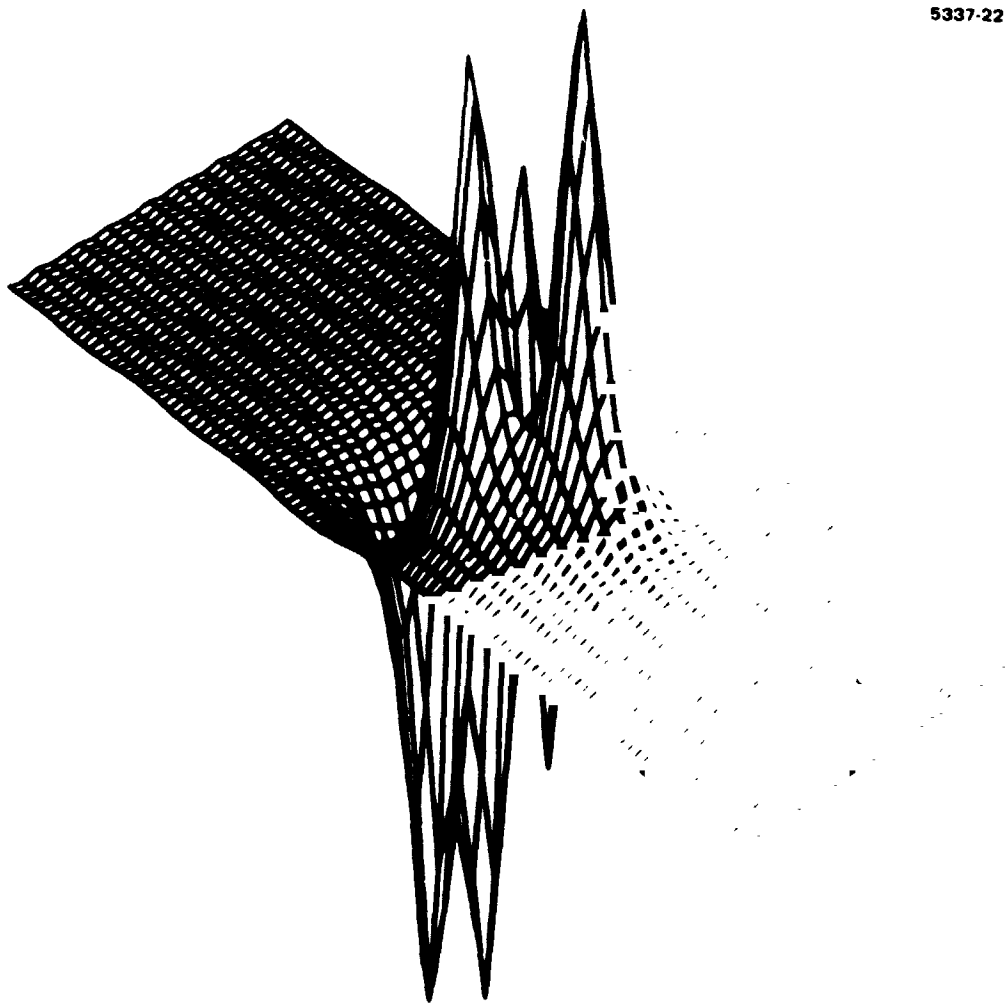


Figure {22} - RGG Cross Gradient Output
Three Mascons at 120 Km Spacing
0.1 Degree Periodic Attitude Error
 $e=0.005$ Elliptical Orbit

To give a dramatic presentation of the effects of very bad attitude control problems on the two outputs of a single RGG system, we increased the amplitude of the previous attitude control error to 1 degree. We kept the period at 5 minutes and kept the eccentricity of the orbit the same. Figure {23} is a plot of the principal gradient difference output of the single RGG system. One can see the mascon peaks in there, and can certainly tell there are three distinct peaks, but an estimate of their magnitude would be of poor accuracy.

5337-23

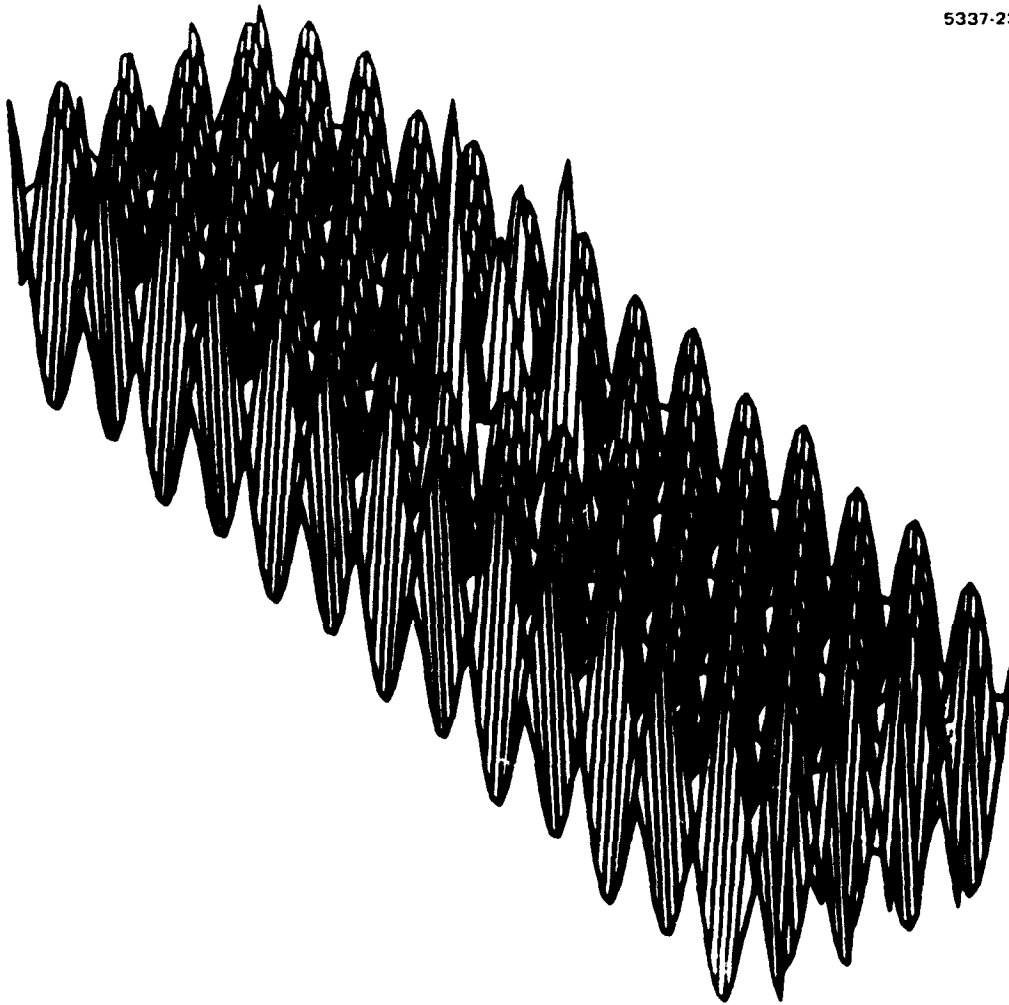


Figure {23} - RGG Principal Gradient Difference Output
Three Mascons at 120 Km Spacing
1 Degree Periodic Attitude Error
 $e=0.005$ Elliptical Orbit

However, a plot of the integrated cross gradient output of the single RGG system (see Figure {24}), shows that this output is nowhere near as drastically affected, even by these very large error rates.

5337-24

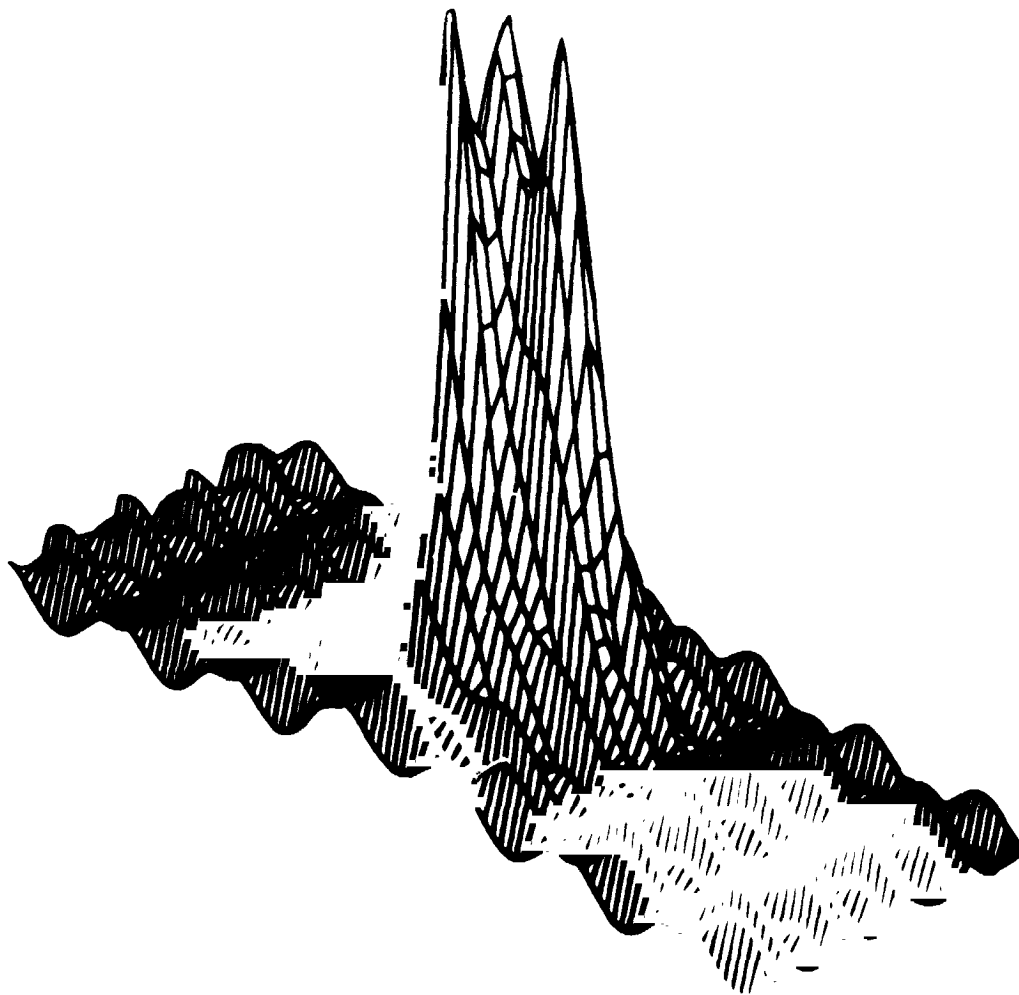


Figure {24} - Integrated RGG Cross Gradient Output
Three Mascons at 120 Km Spacing
1 Degree Periodic Attitude Error
 $e=0.005$ Elliptical Orbit

The conclusions that can be drawn from this simulation are:

Spacecraft altitude variations due to an elliptical orbit may cause some loss of sensitivity and resolution, but the bias shifts introduced should not prevent the extraction of the higher frequency gravity data.

Spacecraft attitude tilts cause a bias shift, and should be rapidly recognizable and removable from the data by their appearance in the cross gradient terms.

Periodic attitude errors caused by malfunction of the attitude control system will cause significant data reduction errors if the attitude error amplitudes are large (greater than 1 degree) and of rapid period (less than 5 minutes). (Since they are time varying, they will show up as angular tilts in the cross gradient outputs and as angular rate gradients of the same periodicity but quadrature phase in the trace.)

A single RGG sensor oriented along the orbital axis to measure the gravity gradients in the plane of the orbit can use the lunar orbit track to track spacing of about 30 Km to obtain good resolution of mascons in both the along track and cross track directions. The cross gradient output of the RGG should be integrated with the spacecraft velocity to obtain a contour map of the vertical gravity field, and then the higher resolution (but slightly distorted) principal gradient difference output of the RGG should be used to enhance the resolution of the data set for geophysical interpretation purposes.